Title
Defect Characterization of Metals in Radiation and Oxidizing Environments using Positron Annihilation Spectroscopy

Author
Auguste, Rasheed

Publication Date
2022

Peer reviewed|Thesis/dissertation

Defect Characterization of Metals in Radiation and Oxidizing Environments using Positron Annihilation Spectroscopy

By

Rasheed K. Auguste

A dissertation submitted in partial satisfaction of the

requirements for the degree of

Doctor of Philosophy

In

Nuclear Engineering

in the

Graduate Division

of the

University of California, Berkeley

Committee in charge:

Professor Peter Hosemann, Chair
Professor Farida Selim
Professor Eric Norman
Professor Mark Asta

Fall 2022

Defect Characterization of Metals in Radiation and Oxidizing Environments using Positron Annihilation Spectroscopy

Abstract

Defect Characterization of Metals in Radiation and Oxidizing Environments using Positron Annihilation Spectroscopy

by

Rasheed K. Auguste

Doctor of Philosophy in Nuclear Engineering

University of California, Berkeley

Professor Peter Hosemann, Chair

Coupled extremes such as radiation and corrosion in nuclear environments induce a state in matter that is far from equilibrium. The addition of corrosion increases the complexity of the nonequilibrium problem. Thus, there is a continual need to advance understanding of these coupled effects to ultimately predict material response and enable the design of new materials that can better withstand these combined extreme conditions. The work in this dissertation advances toward a predictive understanding for how point defect transport can drive radiation damage and corrosion.

This dissertation seeks to advance fundamental understanding of defects from radiation damage and oxidation phenomena in structural materials for nuclear reactor applications. The first objective of this research is to validate rate theory predications of radiation damage defect populations in-situ using positron annihilation spectroscopy. This hypothesis is explored using simulation, execution, and discussion of novel positron annihilation spectroscopy experiments. Ultimately, radiation-induced nonequilibrium monovacancy defects were simulated and experimentally observable with positron spectroscopy, and in-situ vacancy concentration showed an increase with increasing dpa (displacements per atom). The second objective of this research is to validate theoretical predictions of predominant defect identities within passivating systems. Positron spectroscopy was again used to experimentally connect to previous results from simulations of oxide layer defect behavior, electrochemical studies on oxides, and post-mortem irradiation microscopy studies. Oxidation defect behavior in iron and chromium was quantified as a function of oxidation time, temperature, and irradiation.

Positron annihilation spectroscopy is a monovacancy-sensitive, depth-dependent, nondestructive technique to understand defect behavior, which ultimately governs materials' radiation and corrosion performance for safety and corrosion protection of new and existing nuclear structural materials. It is hoped that this research will open new doors to advanced characterization and modelling opportunities in the study of nonequilibrium radiation and oxidation defects.

To my brother Jahmal,

I love and appreciate you, your loud advice, and your unwavering encouragement.

Contents

Acknowledgements

Acknowledgements

First and foremost, I must thank my family as my stabilizing support system during this graduate degree program. The fact that I stayed sane throughout the various trials of this program is a direct reflection of the support I received. Thank you to Ma, Dad, and Jahmal for always being one FaceTime button away. You are my inspirations for success, enthusiasm, and hard work. Every single prayer and kind word of encouragement from my grandparents, aunts, uncles, and cousins was necessary and pivotal to this achievement.

I was able to find supportive community on this coast away from my family. To Rebekka Dagher, Buquis, my love, I am honored to celebrate this latest milestone with you. I am so grateful for your check-ins and your patient understanding. To my community, I appreciate your willingness to hear my complaints and my triumphs with equal measure. To Phillip Aubrey and Veronica Cummings, thank you both for your constant support, active listening, and compassionate wisdom. To my Goldman School people, especially Elizabeth Annis, Daniel Lao-Talens, Ramsey AlQaisi, Sergio Dueñas, Adha Mengis, Rhina Torres, Caroline Palmer, Emory Wolf, Todd Faulkenberry, Mehak Khan, and Saqib Mumtaz, thank you for giving me a sense of belonging and for all the fun outside of work. To the Santa Cruz Crew: Sam Finn, Chelsea Muir, Laura Chen (and Jeff Kwarsick), your lightness, rituals, and reflection prompts helped me make peace with the passage of time. Thank you to the 7 Billou family for all the conversation, food, and laughter. Finally, a big thank you to all the people that have stuck with me since undergrad, high school, and earlier. You have always kept me grounded. To Chocolate City ’17, my Rho Nu brothers, the LBR group chat, and my DnD Discord, thank you because this effort takes a village.

There is no achievement without support or without precedent. I not only built my graduate degree path from the previous examples of nuclear engineering Black graduates, but I also specifically relied on their academic prowess, professional excellence, and lived experiences during my academic journey. This was especially true during difficult career decisions, screening exams, and my oral qualifying exam. I need to also single out Dr. Grey Batie for their incomparable commitment to seeing me and students like me succeed in the academy. Thank you for your hard work, G, but mostly, thank you for being yourself and being my friend.

I would like to thank my thesis committee; Professor Peter Hosemann, Professor Farida Selim, Professor Mark Asta, for their guidance through my experimental process, comments on my dissertation methodology, and overall feedback on this thesis. To my advisor, Professor Peter Hosemann, thank you for your advice, our candid conversations, and your willingness to share knowledge with me on countless occasions. I respect your commitment to experimental materials science and dedication to pushing the boundaries of scientific knowledge.

I am also grateful for the mentors and work relationships gained through Professor Peter Hosemann’s Nuclear Materials group. Every group researcher was willing to take time to train me or to thoughtfully critique my work, no matter how late or how busy they were. Thank you, Jeff Bickel, for your ready helping hand and acerbic wit around the laboratory. Thank you, Dr.

Alan Bolind for your needed safety expertise and caring attitude. Thank you, Dr. Ryan Weed for sharing your positron system expertise. Thank you to the Physics and Mechanical Engineering Department Machine Shops for your design and manufacturing assistance. Thank you to the graduate students in the office who helped me along the way, including Joey Kabel, Hi Tin Vo, Jeff Graham, Franziska Schmidt, Evan Still, Sarah Stevenson and several others.

I would also like to thank the institutions which were instrumental in my scientific development: The University of California at Berkeley and Los Alamos National Laboratory. Sample preparation and data analysis were both made possible because of the efforts of the Ion Beam Materials Laboratory in Los Alamos. Furthermore, a significant portion of this research was also carried out at the Institute of Radiation Physics at Helmholtz-Zentrum Dresden – Rossendorf in Dresden, Germany. Thank you to Dr. Oskar Liedke, Dr. Maik Butterling, and their team for their willingness to lend their positron spectroscopy expertise and equipment for this research.

This work was supported as part of FUTURE (Fundamental Understanding of Transport Under Reactor Extremes), an Energy Frontier Research Center funded by the U.S. Department of Energy, Office of Science, Basic Energy Sciences. Under Dr. Blas Uberuaga, the collaborative environment in FUTURE meetings was an unforgettable example of how science can be collectively advanced by bringing together different experts. This work was also partially supported by the Impulse-und Net-working fund of the Helmholtz Association (FKZ VH-VI-442 Memriox), and the Helmholtz Energy Materials Characterization Platform (03ET7015). This work was also supported by the Ron & Gail Gester Fellowship at the University of California, Berkeley.

1. Introduction

Nuclear power has been one of the predominant energy sources in the United States over the past 60 years. In 2021, nuclear energy accounted for approximately 20% of total electricity generation in the country. [1] As a low-carbon electricity source, nuclear power serves an increasingly important role amid climate change concerns. Along with renewable energy sources, nuclear power deployment has historically been associated with lower emissions per capita, which contributes directly to decarbonization and climate mitigation objectives. [2] In addition to emissions benefits, there is also growing expert consensus that scaling up nuclear energy is a promising path to creating a global energy system that supports high universal living standards. This is especially critical in emerging markets, where almost all (about 95 percent) of the increase in the world's energy demand through 2035 will originate. [3] Climate change affects all nations, so around the world, there is increasing global support for large-scale climate mitigation techniques. Climate change from greenhouse gases (GHG), specifically, has become one of the most important issues of this century. In 2015, more than 190 countries committed to limit global warming by reducing GHG emissions in the Paris Agreement signed at the United Nations Conference on Climate Change in 2015. [4] Given the climate crisis and urgent need to switch to sustainable, low-carbon sources of energy, nuclear power has emerged as an important alternative energy source for large-capacity, firm, baseload electricity.

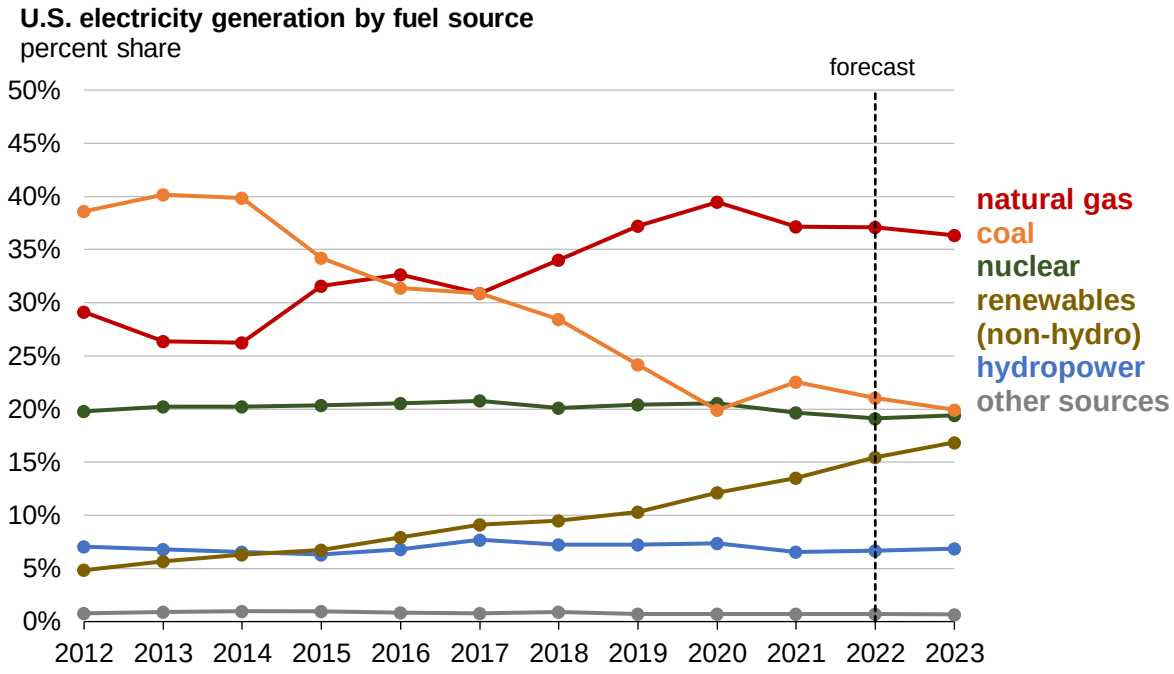

Figure 1.1: U.S. electricity generation by fuel source, all sectors. Nuclear energy has maintained its 20 percent share in electricity generation for the past 10 years. [1]

Figure 1.1 shows the current share of electricity generation from each energy source in the United States, [1] and that nuclear energy has maintained its 20% share in electricity generation for the past 10 years. In the United States, commercial power reactors are either pressurized water reactors (PWRs) or boiling water reactors (BWRs). BWRs and PWRs also account for most reactors in the world. [5] Other reactor types include heavy water reactors, gas-cooled reactors, graphite-moderated reactors, and liquid-metal-cooled reactors. Each reactor concept is promising in terms of producing highly sustainable and low-carbon energy. However, engineering design challenges exist for both safely maintaining currently deployed reactors and realizing other advanced reactor concepts. The internal core components of a nuclear reactor consist of many different structural materials subjected to various harsh environmental conditions including radiation flux, mechanical stress, high temperature, and corrosive media. Choosing appropriate structural materials dependent on degradation conditions expected during service is the key to safe, successful engineering design and risk management, especially in accident scenarios. For example, 304 SS, 304L SS, 316L SS, and 347 SS are common austenitic stainless steels for the core structural materials because they have excellent toughness for dealing with high pressure environment, excellent fatigue resistance for dealing with cyclic stress and excellent water corrosion resistance [6].

Radiation damage is a major materials design consideration for nuclear reactors, especially within the core where radiation fields are the highest. Radiation causes changes in material properties of structural components, like bolts, cladding, or even the overall pressure vessel. These material property changes often weaken structural components, causing them to fail early, limiting their lifetime, which presents a risk analysis and safety issue. [7, 8] Material property changes in a nuclear environment can be divided into three subcategories: mechanical property changes, dimensional changes, or elemental changes. Mechanical property changes refer to deformations from applied stress or changes in a materials' microstructure or phase [9, 10]. Dimensional property changes refer to changes in the size of the component, such as "swelling" due to voids forming in the crystal lattice from radiation damage. Figure 1.2 displays a classic example of voids from radiation damage in 316 SS [11] and Al [12]. Transmission electron microscopy (TEM) results show voids as atoms missing from the lattice. These voids can coalesce over time, growing cavities inside the lattice accompanied by significant decreases in material density and concurrent increases in volume. This process is usually referred to as void swelling, and it presents safety issues when designs must accommodate this dimensional change [13]. Lastly, elemental changes from alpha decay or neutron transmutation processes such as neutron capture or (n, α)-reactions may create He-bubbles or other transmutation products that start to affect the microstructure so that new phases begin to separate out. [14, 15, 16] All these issues work to collectively limit nuclear materials component lifetimes and change the overall performance properties, which ultimately presents reactor safety and risk issues.

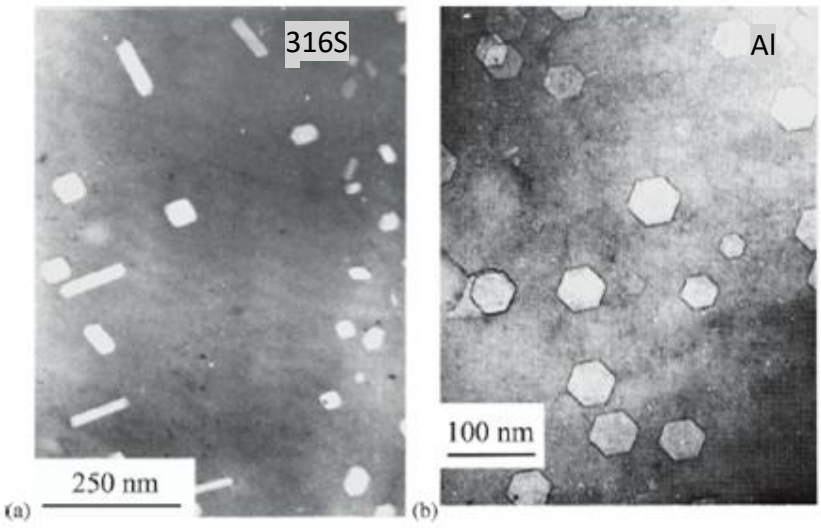

Figure 1.2: TEM micrographs of void formation in 316SS versus Al. Lighter contrast areas are regions of missing atoms called voids. [11, 12]

Radiation-induced effects in reactor components present significant design challenges alone, but these effects are also coupled with other harsh environmental conditions to further limit component lifetimes. Thermal stresses, mechanical forces, and even corrosive media work in concert to cause these material changes. Figure 1.3 [17] features an example of how coupled environments (temperature and radiation) can change a materials property. A notable study showed Ni irradiated by neutrons at different temperatures led to swelling at different rates. There is broad range of swelling responses across 300^{o}C to 700^{o}C with a noticeable peak swelling temperature around 500^{o}C. This is due to the fact that both void growth and void stability factors exhibit a temperature dependence. The swelling rate is dependent on the opposing effects of vacancy mobility increasing with temperature to grow voids versus large void stability decreasing with temperature. Thus, a maximum swelling rate in metals is expected at an intermediate temperature where net flow of vacancies to voids is maximized.

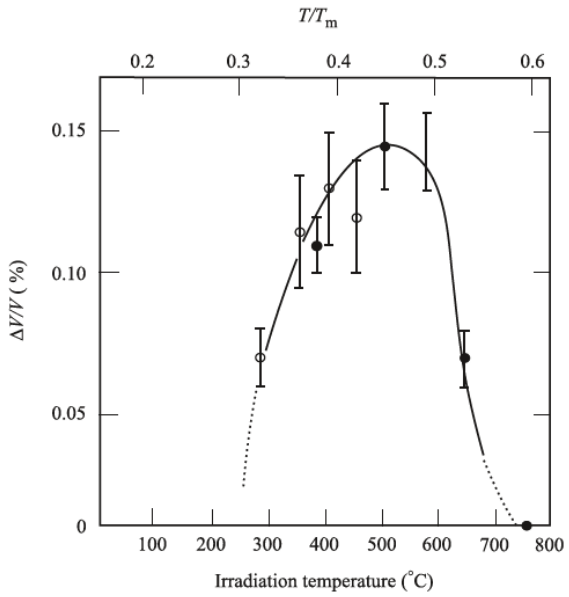

Figure 1.3: Nickel swelling response at different temperatures. There is broad range of swelling responses across 300°C to 700°C with a noticeable peak swelling temperature around 500°C. The swelling rate is dependent on the opposing effects of vacancy mobility increasing with temperature to grow voids versus large void stability decreasing with temperature. Originally Brimhall (1972) [17]

From an engineering point of view, the voids produced by high-temperature (> 400°C) irradiation of metals has substantial economic and safety implications. Void swelling can yield up to tens of percent increases in volume, which then requires a substantial reactor design modification for operating at high temperatures. In 1966, Cawthorne and Fulton first reported pronounced swelling including the formation of microscopic voids in stainless steel irradiated to high fluences at elevated temperature. [18] Shortly afterward in the 1970s, Huebotter and Bump discussed how swelling implies an additional cost of several billions of dollars over 50 years in the operating cost of a fast breeder reactor fleet (which operate at high temperatures). The cost of accommodating 5% versus 15% swelling in breeder reactor fleet over the period 1970 to 2020 increased from $860 Million USD to $5.6 Billion USD (in 1970 present worth) [19]. In pressurized water reactor environments where components face considerably lower temperatures (around 200°C to 350°C) than proposed advanced reactors, drastic swelling in core components can still be observed. A study by Edwards and Bruemmer [20] on a baffle bolt used to secure baffle plates in a pressurized water reactor core revealed stark differences in swelling along the bolt, despite its short length. The bolt head was closest to the core and received the highest dose (19.5 dpa), but no voids were present in TEM micrographs. The largest void size was observed at the top shank of the bolt, even though it saw lower dose (12.2 dpa) than the bolt head. However, the bolt head saw a lower temperature (320°C) than the bolt shank (340°C) and bolt threads (330°C). The temperature effect on swelling is evident again in this example. Furthermore, it is also evident how precise safety design tolerances must be considering the baffle bolts location inside the reactor core containment. Thus, there are substantial economic and safety motivations to study the mechanism for void formation from radiation damage in nuclear reactor alloys.

Corrosion is another major materials design constraint for nuclear reactors, especially for stainless steels in water-cooled reactors such as LWRs. Corrosion occurs when a metal comes into contact with an environment, either liquid or gas, which causes the metal to degrade. In an oxidizing environment, the corrosive medium attacks the metal chemically, causing it to transform into a more stable phase. This chemical reaction results in movement of positively or negatively charged atoms and vacancies in the oxide, which are analogous to the metallic point defects created during irradiation. The corrosion mechanisms are so important that for existing nuclear power plants, the safety cases for life extension are often predicated on demonstrating good corrosion performance of the service components, including the reactor pressure vessel [8]. For a new power plant, understanding the key corrosion mechanisms and how to limit corrosion damage is a key challenge to achieving 50 to 60-year reactor lifespans. A notable corrosion mechanism for water-cooled reactors is stress corrosion cracking (SCC), or the premature cracking of an alloy in the presence of a tensile stress and a corrosive environment. PWRs primarily experience stress corrosion cracking challenges, while BWRs experience neutron-activated irradiation-assisted stress corrosion cracking (IASCC) challenges [21]. In IASCC, the material becomes susceptible to SCC after neutron embrittlement. [22] While these specific SCC mechanisms have been studied extensively, the more fundamental way in which irradiation affects a material's defect evolution in a corrosive environment has not been the subject of extensive investigation.

To further characterize radiation induced changes, one aspect of research explored in this dissertation is to understand the interplay of the radiation damage and chemical changes in nuclear reactor structural materials. To reduce the risks of operating nuclear systems, degradation prediction methodologies are used to evaluate the integrity of components over time and assist with mitigation approaches. Both prediction and mitigation methodologies rely critically on the proper conceptual understanding and the modeling of the fundamental defects during irradiation and oxidation. How does radiation ultimately affect defects in different chemical extremes such as oxidizing environments? What is the mechanism for how radiation defects influence existing defects in the oxidation process? Ultimately, this understanding would enable an accelerated pathway to qualification and design optimization of existing structural reactor components and even future advanced reactor applications.

2. Background

Radiation damage in materials is a fundamental problem faced by most nuclear technologies, e.g., nuclear fission, nuclear fusion, and other accelerator-based techniques. Fundamentally, an incoming particle transfers a fraction of its energy to a host lattice atom—depending on interacting particles' masses and energies—or induces a nuclear interaction which can lead to more energetic particles. Subsequently, the struck atom carries a kinetic energy which may induce further displacement damage in the material even leading to large displacement cascades. The total amount of displacements caused by an energetic particle interacting with the material is what is usually characterized in the unit displacements per atom (dpa). While it is important to understand the number of initial displacements produced, it is the evolution of these displacements and resulting defects that cause the permanent materials property changes such as swelling, hardening, or embrittlement.

When considering the evolution of radiation damage, it is important to remember the time scale of the damage evolution after the initial displacements of the incoming particle. Numerous computer simulation and experimental studies have shown that the time scale for the ballistic atom collision processes is of the order of 100 femtoseconds, and the time scale for subsequent thermalization of the collisions is on the order of 1 to 10 picoseconds [1]. A notable model, the Kinchin and Pease model captures the fundamental physics of the atomic collisions. This model will be discussed in more detail in the subsequent section. After the thermalization stage, longer-time scale (nanoseconds to years) damage evolution caused by thermally activated processes then occur. Figure 2.1 [2] shows this process in detail. The first atom in the material that receives a recoil energy from the passing particle is called the primary knock-on atom (PKA). The collision cascade model starts with independent binary collisions (Figure 2.1a) [2].

After a few tens of picoseconds, if the initial PKA energy is high enough (greater than 1 keV) and the material is dense, a very dense region of multiple atomic collisions, sometimes called a heat spike, may form (Figure 2.1b) [1,2]. During the heat spike stage, the collision energy of the displaced atoms is shared among their neighboring atoms in a region of high deposited energy density. The development of the spike requires about 0.1 picoseconds, and the spike may occupy several zones in which the energy is high enough so that collectively the atoms resemble liquid material (i.e., losing lattice structure). As energy is transferred to the surrounding atoms, the molten zones return to the thermodynamic equilibrium at the end of the spike (after about 10 picoseconds). The quenching stage takes the most time during the thermal spike stage as the lattice structure is restored. During this time, stable lattice defects form either as point defects or as defect clusters. Point defects consist of interstitials and vacancies (Frenkel pairs) created in this process [2]. Interstitials are the atoms knocked from their lattice sites and vacancies are the resulting empty lattice positions. The total number of defects at this stage is much less than the number of atoms displaced in the collisional stage. The annealing stage involves further rearrangement and interaction of defects and proceeds via thermally activated diffusion of mobile lattice defects. This marks the end of the primary damage phase, and the material is left with the remaining stable lattice defects (Figure 2.1c). [2]

The next stage is the defect mobility stage (depicted in Figure 2.1d [2]), which lasts until all mobile defects anneal out of the lattice, escape the cascade region, or another cascade occurs within it. The timescale extends from nanoseconds to months, depending on the temperature and the irradiation conditions. The major determinant in this phase is the remaining defects' mobility. Most defects can be mobile, but the energy required to move a defect (mobility energy) may be so high that it becomes immobile and stops evolving for all practical purposes at a given temperature. Atoms in a lattice are in a constant state of motion due to thermal vibration, and this means that point defects in the lattice are also in motion. The random nature of thermal vibration causes random motion, or self-diffusion of the atoms and the defects to maintain thermal equilibrium with their surroundings. Note that vacancy mobility is governed by substitutional diffusion, defined as switching places with an adjacent lattice position. However, self-interstitials move within the lattice interstices (interstitial diffusion), and self-interstitials generate more strain on the surrounding lattice than vacancies. Interstitial mobility is generally greater than vacancy mobility because bonding of interstitials to the surrounding atoms is normally weaker and there are many more interstitial sites than vacancy sites to diffuse to.

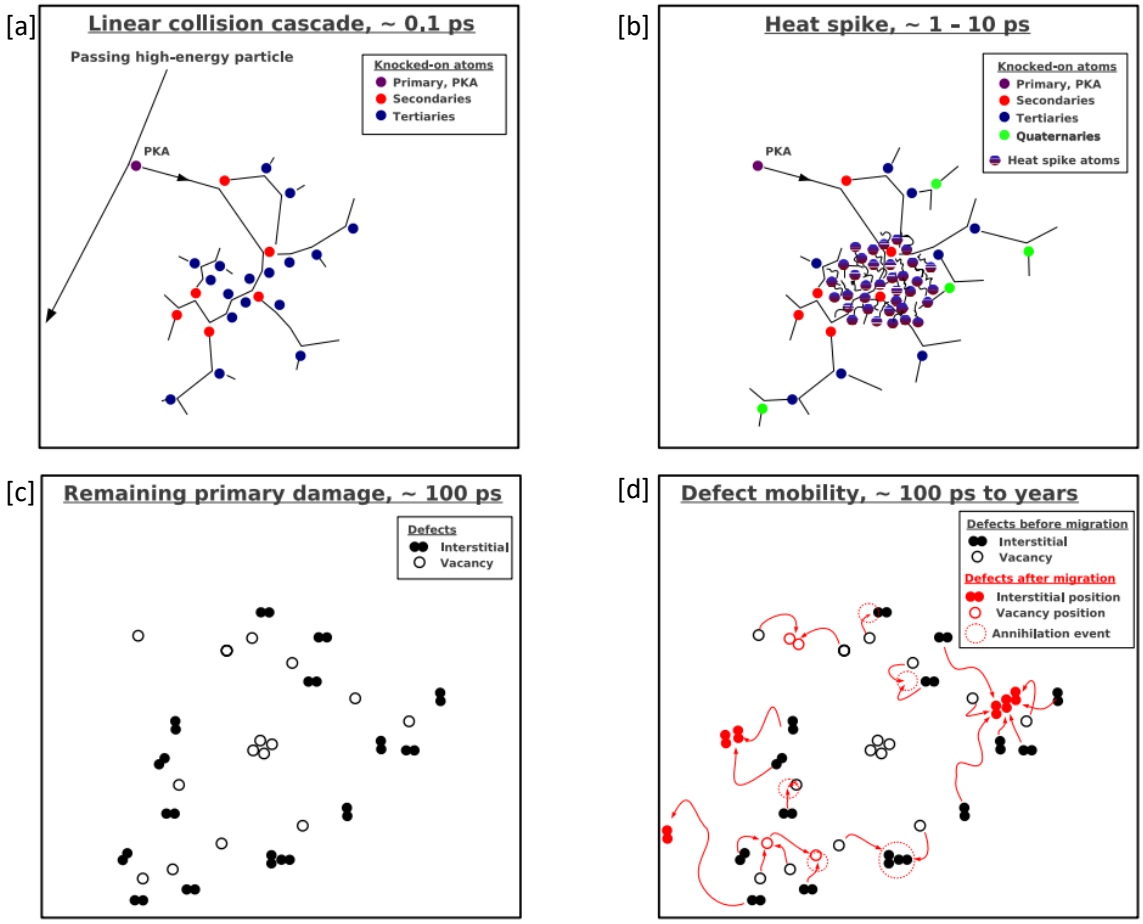

Figure 2.1: Schematic illustration of the stages of radiation damage development from an energetic particle. [a] The linear collision cascade stage in the first 0.1 ps contains collisions with nuclei (primary knock-on atoms (PKA) from incoming energetic particles) to produce

damage. [b] The PKA then induces a cascade of atomic collision processes which locally heats the material atoms. [c] After the heat spike, a fraction of the point defects remains in the lattice. [d] Finally, longer-time scale (nanoseconds to years) damage evolution occurs caused by diffusion of point defects. [2]

The outcomes of the diffusing point defects determine the permanent damage within the material. Mobile vacancies and interstitials may meet within the lattice (i.e., an empty lattice position meets a displaced lattice atom—restoring the lattice structure) in a process called defect recombination, the reducing the number of permanent defects. Point defects can also meet and annihilate with other types of existing material defects like grain boundaries or dislocations, again reducing the number of permanent defects. [3] Alternatively, point defects can instead meet more of the defects of the same type, growing into vacancy clusters or interstitial loops. The accumulation of radiation-induced defects such as interstitial loops or vacancy clusters can lead to significant swelling, hardening, and embrittlement of the structural materials.

For example, void swelling caused by vacancy cluster buildup has been observed to cause embrittlement at irradiation temperatures in fast reactor environments between 30 to 60% of materials' melting point (T_m) and damage levels more than 10 dpa. Void swelling of over 14% was observed in 12X18H9T steel fuel assembly wrappers irradiated in BOR-60 fast reactors (Figure 2.2a) [4, 5]. The wrappers could not plastically deform in response to stress as indicated by the severely brittle failure of the wrappers failing during the refueling operation. Bulk tensile tests revealed planar facets in the fracture surface (Figure 2.2b) [4, 5], and these brittle, planar fracture surfaces were confirmed with TEM to be the result of intense shear localizations from extensive voids in the microstructure (Figure 2.2c) [4, 5]. This example shows that radiation-induced changes in the microstructure from point defect accumulation can lead to embrittlement in materials observed at the macroscale. Therefore, to effectively mitigate the effects of radiation damage, it is crucial to understand the evolution of point defect populations as they influence the deformation and failure mechanisms within the materials.

Extensive experimental and computer simulation studies have been performed over the past several decades to investigate the nature of the radiation damage point defect evolution. The work in this dissertation is primarily concerned with one of the oldest radiation damage simulation methodologies, reaction rate theory, or rate equations, which will be reviewed in detail in a subsequent section.

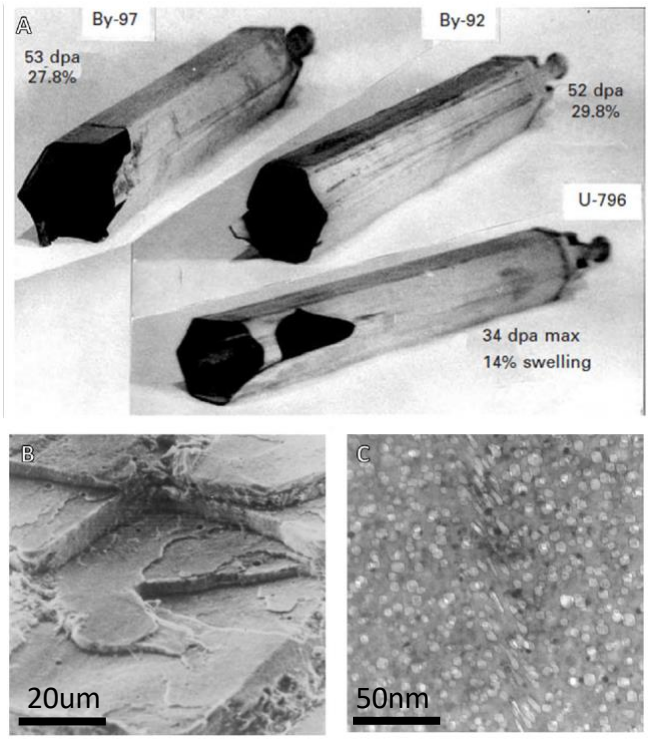

Figure 2.2: [a] Void swelling results of 12X18H9T steel fuel assembly wrappers in BOR-60 fast reactor revealing severe brittle failure during refueling [b] Micrograph of the brittle, planar facets of the fracture surface from a tensile test. [c] TEM micrograph showing voided microstructure responsible for intense shear localizations [4, 5]

2.1 Kinchin and Pease model

The Kinchin and Pease model [6] (Kinchin-Pease model, KP model) for atom displacements captures the fundamental behavior of the initial displacements produced in the lattice from an incoming particle (see Figure 2.1a [1]). It is a fundamental model for understanding primary radiation damage from an incident charged particle. First, define P_d as the probability that a struck lattice atom is displaced upon receipt of energy transferred to the struck atom, T. There is some minimum energy that must be transferred in order to produce a displacement, E_d. The magnitude of E_d is dependent on the crystallographic structure of the lattice, the direction of the incident primary knock-on atom (PKA), and the thermal energy of the lattice atoms. The model makes the following assumptions:

1. The radiation damage cascade results from two-body elastic collisions between atoms.
2. The displacement probability is 1 for $T > E_d$.
3. When an atom with initial energy T emerges from a collision with new energy T' and generates a new recoil with energy ε, no energy passes to the lattice and $T = T'+\varepsilon$.
4. Energy loss by electron stopping is given by a cut-off energy E_c. If the PKA energy is greater than E_c, PKA energy transferred to lattice atoms will be dispersed only via electron

ionization. Thus, no additional displacements occur until electron energy losses reduce the PKA energy to less than E_c. For all energies less than E_c, electronic stopping is ignored, and only atomic collisions occur.

5. The energy transfer cross section is given by the hard-sphere model.
6. The arrangement of the atoms in the solid is random such that crystal structure effects on atomic collisions are neglected.

Assumptions 1 and 3 assume conservation of energy and linear momentum. Solving a system of equations for the collision yields the maximum allowable energy transferred to the lattice atom, in Equation 2.1 and Equation 2.2.

$$\epsilon_{\max} = T - T' = \frac{4mM}{(m+M)^2} E \tag{2.1}$$

$$\mathrm{T} = \frac{2mM}{(m+M)^2} E\ (1 - \cos(\theta)) \tag{2.2}$$

Where m and M are the mass of the incident particle and the struck atom, E is the energy of the incident particle, and θ is the scattering angle between the two atoms. Integrating over all possible scattering angles to find the average energy to the struck atom yields the average energy transferred to the struck atom being $\epsilon_{max}/2$. Assumption 4 considers electronic energy loss to be the main stopping mechanism for high energy incident particles. However, in electronic energy loss models (e.g., Lindhard or Bethe-Bohr [7, 8]), the energy transferred to the lattice is lost to electron ionization, so there are no atomic displacements. This leads to the cutoff energy for atomic displacements from high energy particles, E_c. Assumption 6 ignores that metals have a crystal structure for the model because in reality, the potential barrier surrounding an equilibrium lattice site is not uniform in all directions. To illustrate, Figure 2.3 shows the displacement energy as a function of direction in FCC Copper [9]. However, since the direction of the recoil is determined from the collision event, which is itself a random process, the recoil direction is entirely random. The single value quoted for displacement energy in radiation damage calculations represents a spherical average of the potential barrier surrounding the equilibrium lattice site. In practice, there are ASTM standards for radiation damage simulations that set the displacement threshold energy, E_d at a constant 40 eV [10].

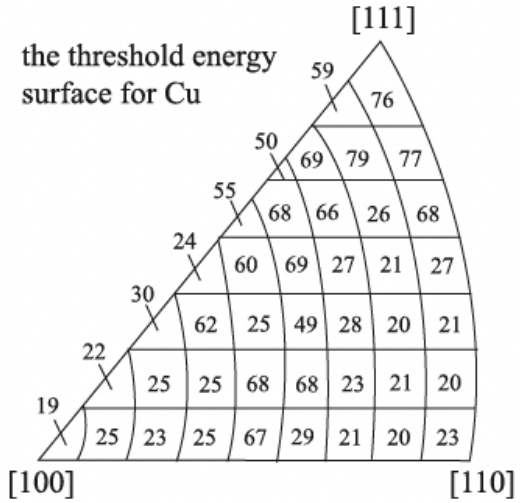

Figure 2.3: Displacement energy as a function of incident particle direction in copper. The single value usually quoted for displacement energy in radiation damage calculations represents a spherical average of the potential barrier surrounding the equilibrium lattice site. Values shown are in eV. [9]

In summary, the K-P model solves for the number of displaced atoms, ν, with a given initial particle energy, T. When $T < E_d$, there are no displacements. If T is greater than E_d but less than $2E_d$, two results are possible. First, the struck atom could be displaced from its lattice position and the PKA, now left with energy less than E_d, replaces the original atom. However, if the original PKA does not transfer at least $2E_d$, the struck atom remains in place and no displacement occurs. In either case, one displacement is the only result possible from a PKA with energy between E_d and $2E_d$. Lastly, when $T > E_c$ after the cutoff energy E_c, energy lost by the particle will be dispersed through ionization by lattice atoms, so there are no additional displacements. Thus, the full K-P model for $\nu(T)$, is given in Equation 2.3 and a schematic of number of displaced atoms as a function of energy, $\nu(T)$, is given in Figure 2.4.

$$\nu(T) = \begin{cases} 0 & for\ T < E_d \\ 1 & for\ E_d < T < 2E_d \\ \frac{T}{2E_d} & for\ 2E_d < T < E_c \\ \frac{E_c}{2E_d} & for\ T \geq E_c \end{cases} \tag{2.3}$$

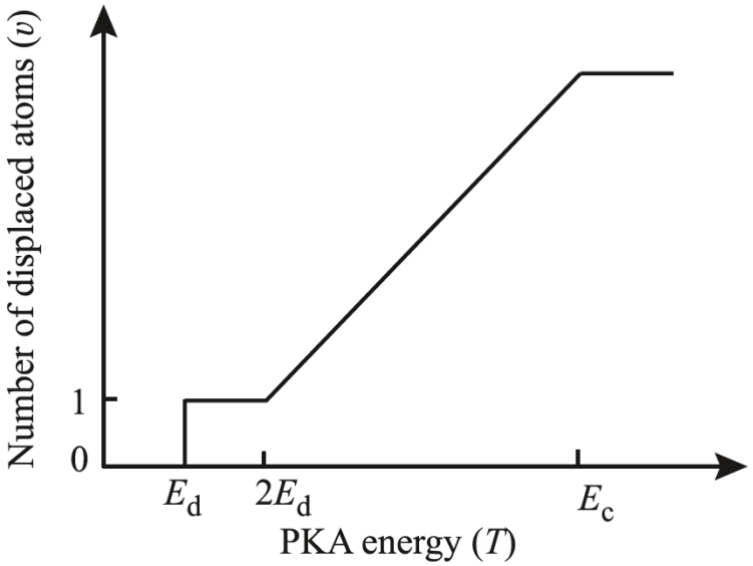

Figure 2.4: Schematic plot of the number of displaced atoms, ν(T), as a function of the PKA energy, T, according to the Kinchin-Pease model in the radiation damage cascade. [6]

2.1 Rate theory for radiation damage

Standard rate theory, rate theory, or rate equations refer to the methodology of using partial differential equations of defect densities to simulate their creation, diffusion, and survival from the damage cascade. The advantage of using rate theory is that it can span very large time, spatial, and energy ranges, from defect production in cascades to changes in macroscopic properties. The disadvantage is that it only gives average defect concentration information.

The Wiedersich rate theory approach uses four sets of variables for the two partial differential equations: one for vacancies and one for interstitials formed [3]. The first term to consider is the dpa rate, $\dot{n}$, which captures how many atomic displacements per second are expected based on the incoming radiation. Then, the sink annihilation probability, p, for the point defects – that is- if the point defect reaches a sink such as a dislocation, how likely the defect is to annihilate there. A key consideration in rate theory is which annihilating features (called traps or sinks) to include and what the trap (sink) strengths are. The results are naturally sensitive to which defects are included, what the associated sink strengths are, and how they are treated.

Third, the frequency factor, ν, is based on the migration probability of the point defects, or how likely are they to move. Fourth, the recombination factor, a, for point defects models the fact that in the crystal system of measurement, there is a fixed number of specific lattice sites available for point defect recombination, whether it be an interstitial finding a vacancy or vice versa. Writing a partial differential equation for those terms allows observation of the change in population of vacancies over time and a theoretical solution for the defect concentration at steady state. Note well that defect clustering is ignored in Wiedersich's original theory, which would yield phenomena such as void swelling. One can solve this system of coupled equations

for a steady state population of point defects with just one more consideration for the thermal equilibrium defects. The full set of differential equations is written in Equations 2.1 (vacancies) and 2.2 (interstitials):

$$\frac{dC_{1v}}{dt} = \dot{n}_{pv} - (v_v a_v + v_i)c_v c_i - v_v p_v c_v \tag{2.1}$$

$$\frac{dC_i}{dt} = \dot{n}_{pv} - (v_i a_i + v_v)c_v c_i - v_i p_i c_i \tag{2.2}$$

where $\dot{n}$ = displacements per atom per second (dpa/s – dpa rate), p_i = sink annihilation probability for interstitials, p_v = sink annihilation probability for vacancies, v_i = frequency factor for interstitials, v_v = frequency factor for vacancies, a_i = recombination factor for interstitials, and a_v = recombination factor for vacancies.

Thermal equilibrium defects must be considered in this model because of the fact that the material is not at 0 K. Thermodynamically, there is already a steady-state population of vacancies and interstitials from just thermal motion, so the total vacancy concentration must include both the thermal vacancies and the radiation damage induced point defects. Equation 2.3 shows this consideration for thermal defects:

$$C_{1v}^{th} = \mathrm{e}^{\left(\frac{S_{1v}}{k}\right)} * e^{-\frac{H_{1v}}{k_b * T}} \tag{2.3}$$

$$C_i^{th} = \mathrm{e}^{\left(\frac{S_i}{k}\right)} * e^{-\frac{H_i}{k_b * T}} \tag{2.4}$$

with S_x and H_x being the entropy and enthalpy of formation of the associated point, k_b is Boltzmann's constant, and T is temperature.

Finally, solving this slightly modified system of equations for vacancies and interstitials gives an expression for the steady state population of vacancies during irradiation according to Wiedersich. This solution mathematically estimates the point defect population during irradiation. The full rate equation for monovacancy concentration, C_{1v}, and interstitial concentration, C_i, is given below in Equations 5 and 6 [3].

$$C_{1v} = C_{1v}^{th} + C_{1v}^{ne} = C_{1v} = C_{1v}^{th} + \frac{1}{2}C\left\{\left(1 + 4 * \frac{\dot{n}\, v_i p_i}{A v_v p_v}\frac{1}{C^2}\right)^{\frac{1}{2}} - 1\right\} \tag{2.5}$$

$$C_i = C_i^{th} + \frac{C_{1v}^{ne} v_v p_v}{v_i p_i} \tag{2.6}$$

$$with: C = \frac{v_i p_i}{A} + C_{1v}^{th} + \frac{C_{1v}^{th} v_i p_i}{v_v p_v}\, and\ A = v_i a_i + v_v a_v$$

where C_{1v}^{th} is the contribution of thermal monovacancies and C_{1v}^{ne} is the contribution of nonequilibrium monovacancies from radiation damage. The point defects are assumed to be produced randomly throughout the solid. They move by random walk through the lattice until they cease to exist either by recombination with the opposite type of defect or by incorporation into the lattice at fixed, unsaturable sinks such as dislocations, grain boundaries and voids. Because defect clustering is ignored, so no attempt is made to treat the nucleation of vacancy clusters, voids, and interstitial loops quantitatively, but the basic theory can be extended to derive void growth rates or swelling rates from the total sink annihilation rates and the relative concentrations of sinks with preferential interstitial or vacancy absorption [3]. Figure 2.5 below shows an example of the steady-state populations calculated from Ni irradiation from the original Wiedersich manuscript. In addition, recalculated values for the steady-state population of point defects were modelled in MATLAB [11] to reproduce the results. Values for the provided for calculation in Table 2.1. There is overall agreement between the original and recalculated results.

Parameter	**Value**
H_{1v}	1.39 eV
$H_{1v,m}$	1.38 eV
H_i	4.08 eV
$H_{i,m}$	0.09 eV
$\exp(S_{1v}/k)$	4.48
$\exp(S_i/k)$	5
v_{v0}	5×10^{13} sec^{-1} [12]
v_{i0}	1.0×10^{14} sec^{-1} [12]
a_i	12
a_v	12
Correlation factor$_{1v}$	0.7437
Correlation factor$_i$	0.7437

Table 2.1: Constants for Nickel used in Wiedersich Equation 2.5 and Equation 2.6 for MATLAB calculations [3, 12]

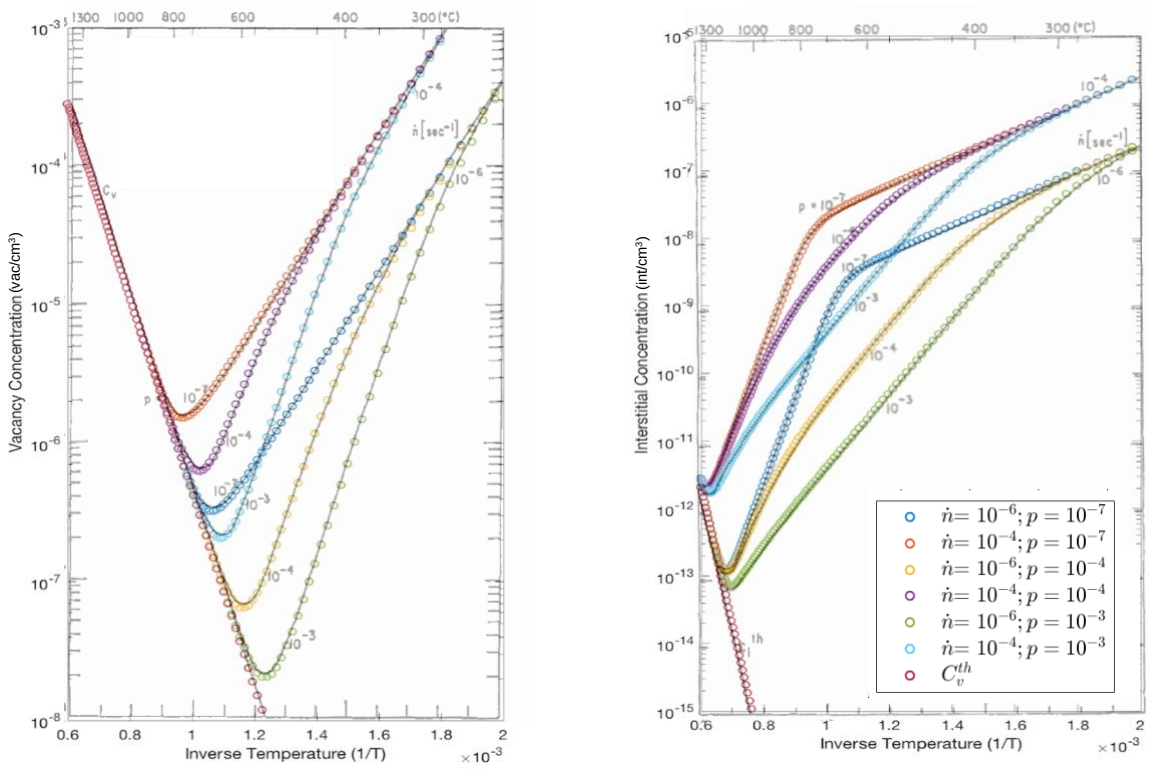

Figure 2.5: Expected concentration of vacancies in Ni plotted as a function of inverse temperature, dpa rate ($\dot{n}$) and annihilation probability (p) according to Equations and 6 and Ni parameters from Wiedersich et al. (1972) [3]. The open circles were calculated values plotted in MATLAB [BG4] to reproduce the plot from the original Wiedersich et al. paper [3]. The low temperature region limits thermal monovacancy formation while at high temperature the vacancy concentration is dominated by the equilibrium vacancy concentration.

At low temperatures, where C_{1v}^{th} is negligible, C_{1v} is dependent on the level of defect production (dpa rate), $\dot{n}$, from irradiation and the vacancy annihilation probability from the presence of sinks (p_v). As illustrated in Figure 2.5, with increasing temperature, C_{1v} initially decreases, goes through a minimum and then becomes indistinguishable from the thermally produced vacancy concentration without defect production from radiation. In the low temperature region, there is a small contribution from thermally produced vacancies, C_{1v}^{th}, while vacancies produced via radiation become more mobile with increasing temperature, increasing the likelihood of annihilation, and decreasing C_{1v}. Ideally, non-equilibrium experiments should be done in this low temperature region to measure the dominant effect of C_{1v}^{ne}. According to theory, increasing the dpa rate at low temperatures yields increasing concentration of vacancies, which can lead to larger extended defects such as large voids or vacancy clusters.

One can extend the rate theory model for different elements in order to observe interesting trends related to crystal structure and melting points. For this analysis, other common nuclear materials of interest such as Cu, Fe, W, Cr, and Al are presented. The curves for FCC materials, Cu, Ni, and Al, are shown first in Figure 2.6. The dpa rate and annihilation probabilities are held

constant at 10^{-6} dpa/s and 10^{-7}, respectively. Rate theory does not explicitly account for crystal structure, but interesting trends for FCC metals become apparent once plotted together. At low temperatures, the lowest equilibrium vacancy concentrations are from lower melting point metals (e.g., Al). This is due to the high mobility of nonequilibrium radiation vacancies from low melting point materials. However, at high temperatures, the formation of thermal vacancies dominates in all cases, so low melting point metals which also more readily form vacancies have a higher equilibrium vacancy concentration. Thus, the "inflection" temperature, or the temperature in which the thermal vacancy concentration begins to dominate the radiation produced vacancies, also seems to increase with increasing melting point.

Element	**Ni**	**Cu**	**Al**
Crystal Structure	FCC	FCC	FCC
Melting Point	1718 K	1357 K	933 K
H_{1v}	1.29 (0.02) eV [13]	1.28 eV [16]	0.65 eV [17]
$H_{1v,m}$	1.06 eV [12]	1.0 eV [15]	0.66 eV [18]
H_i	3.439 eV [14]	3.0 eV [15]	1.79 eV [19]
$H_{i,m}$	0.11 eV [14]	1.0 eV [15]	0.084 eV [19]

Table 2.2: Constants for FCC materials (Cu, Ni, and Al) used in Equation 2.5 for MATLAB calculations. See reference section for enthalpy and entropy formation and migration energies.

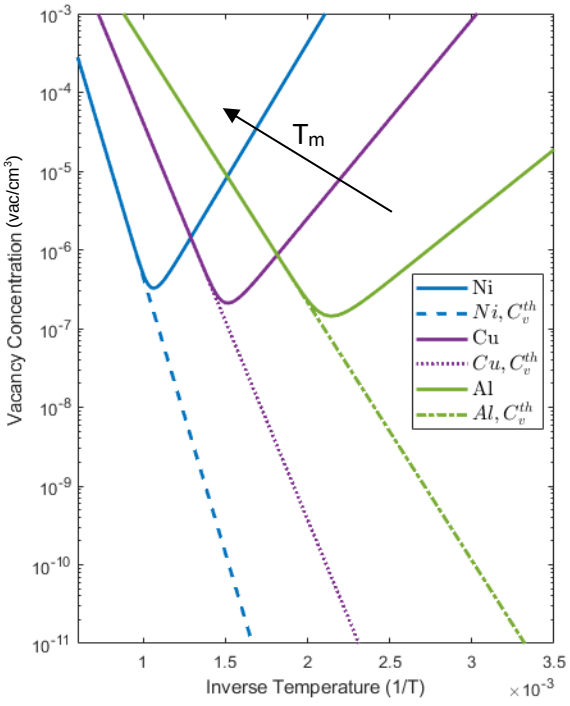

Figure 2.6: Expected concentration of vacancies in Ni, Cu, and Al plotted as a function of inverse temperature according to Equation 2.5 from Wiedersich et al. (1972). [3] The increase in melting temperature corresponds to a decrease the population of thermal vacancies.

Solving the rate theory equations for BCC materials yields a similar trend to FCC materials in terms of defect concentration behavior as a function of melting point. The Wiedersich curves for BCC materials, Fe, Cr, and W, are shown first in Figure 2.7. The dpa rate and annihilation probabilities are held constant at 10^{-6} dpa/s and 10^{-7}, respectively. Again, at low temperatures, the lowest equilibrium vacancy concentrations are from lower melting point metals (e.g., Fe compared to Cr). The "inflection" temperature, or the temperature in which the thermal vacancy concentration begins to dominate the radiation produced vacancies, also increases with increasing melting point.

	Cr	**Fe**	**W**
Crystal Structure	BCC	BCC	BCC
Melting Point	2180 K	1811 K	3695 K
H_{1v_f}	2.0 eV [20]	1.9 eV [22]	3.6 eV [24]
H_{1v_m}	0.95 eV [20]	0.735 eV [22]	1.78 eV [24]
H_{i_f}	6.074 eV [21]	4.0 eV [23]	9.06 eV [25]
H_{i_m}	0.052 eV [21]	0.3 eV [23]	0.38 eV [26]

Table 2.3: Constants for BCC materials (Fe, Cr, and W) used in Equation 2.5 for MATLAB calculations. See reference section for enthalpy and entropy formation and migration energies.

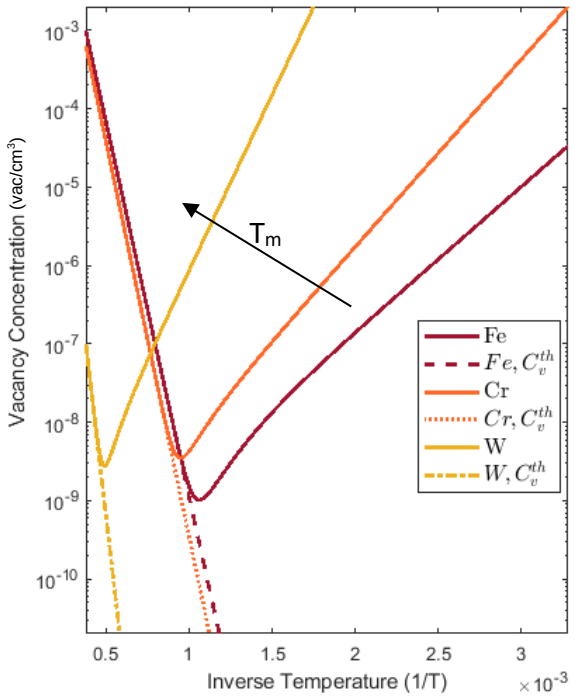

Figure 2.7: Expected concentration of vacancies in Fe, Cr, and W plotted as a function of inverse temperature according to Equation 2.5 from Wiedersich et al. (1972). The increase in melting temperature corresponds to a decrease the population of thermal vacancies.

Plotting the BCC and FCC materials together also yields an interesting comparison. The BCC materials have a consistently lower thermal vacancy concentration than FCC materials. This is due to the larger defect formation energies in BCC materials. The vacancy concentrations at the inflection points of these materials also shows an interesting trend. It seems that FCC materials show higher vacancy concentrations at the inflection points (10^{-6} – 10^{-7}) versus BCC materials (10^{-8} – 10^{-9}). This could indicate more defects in FCC materials from thermal and radiation induced vacancies. But it is more likely that the annihilation probability for this comparison is held constant, whereas changes in the microstructure during irradiation can also have a large impact on defect concentrations. FCC materials are known to form stacking faults and dislocations under irradiation, which can act as considerable sinks for vacancies compared to BCC materials.

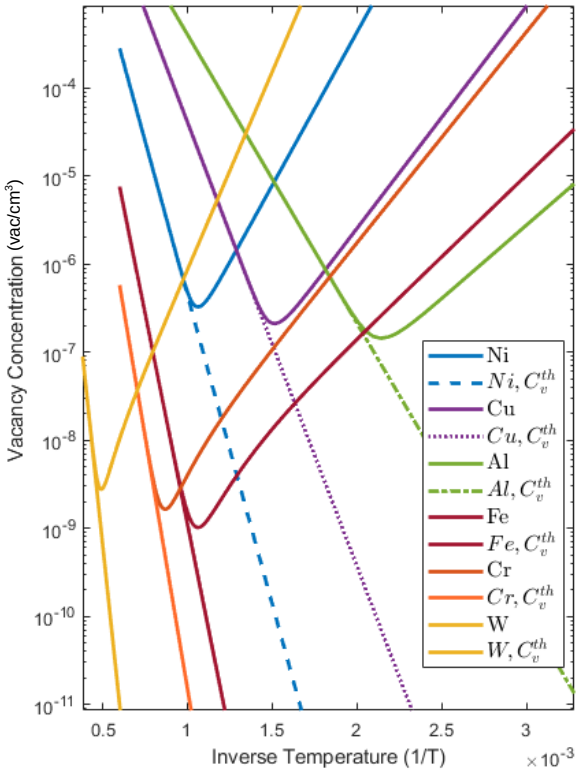

Figure 2.8: Expected concentration of vacancies in Ni, Cu, Al, Fe, Cr, and W plotted as a function of inverse temperature according to Equation 2.5 from Wiedersich et al. (1972). The BCC metals have higher melting points and show less contribution of thermal vacancies. The radiation induced vacancies have higher mobility in BCC materials though, so for the same annihilation probability, BCC vacancies are more likely to annihilate, leading to less overall BCC vacancies than FCC.

Larger extended defects in materials created by ion irradiation present a multi-scale problem with defect lifetimes ranging from picoseconds to years [27, 28]. Rate theory has even been extended to look at these larger defects before, particularly in modelling sink strength effects on steady-state defect populations. Wiedersich even hypothesized that if defect clusters are formed in a cascade, they can become the dominant sinks for mobile defects. [3] Additionally, including defect cluster formation allows rate theory to account for microstructural evolution during the damage cascade. [28-34]

As stated before, there are a large number of transient displacements in the radiation cascade, but most self-anneal with a time scale on the order of picoseconds, leaving just a relatively small number of defects. These remaining defects are still nonequilibrium [35], so capturing small point defects with short time scales must be done in-situ, before further self-annealing and relaxation to larger, extended, more stable defects. Again, direct quantification and verification of Equation 2.5 has not been conducted experimentally since quantifying monovacancies during irradiation

is not trivial. However, since this is a dynamic problem experimental verification of either the displacement damage or its evolution has proven to be difficult.

2.2 Point defects from oxidation

Corrosion is another major materials design constraint for nuclear reactors, especially for stainless steels in water-cooled reactors such as LWRs. Along with radiation, corrosive chemical environments cause material property changes that often weaken structural components, causing them to fail early, limiting their lifetime, which presents a risk analysis and safety issue. For instance, irradiation-assisted stress-corrosion cracking (IASCC) is the radiation-induced acceleration of progressive fracturing in a material as a result of the combined influence of tensile stress and corrosive chemical reactions on susceptible materials. IASCC is particularly an issue in boiling water reactors (BWRs), which prompted a long series of single-factor mitigation actions since the 1950s, some of which cost hundreds of millions of dollars per plant [36].

In IASCC, the influence of point defects is particularly highlighted, as it is the diffusion of radiation-induced point defects that contributes to the acceleration of the corrosion process. Thus, the relationship between radiation non-equilibrium defects and corrosion or oxidation defects merits investigation. [36] The mechanism for IASCC in BWRs starts with the neutron irradiation producing point defects, which subsequently diffuse. These point defects can diffuse along with existing solute atoms in steels during vacancy diffusion, forcing the migration of important alloying elements including Ni and Cr in stainless steels. Cr preferentially transports by vacancy exchange over Fe and Ni, and vacancies are absorbed by sinks at the grain boundaries. This leads to a depletion of Cr at the grain boundaries, making the overall material more susceptible to cracking at grain boundaries [37]. Interestingly, just as radiation produces point defects, oxidation and corrosion environments also produce defects that affect the overall behavior of the passivating layer.

Oxidation defects are of particular importance to the nuclear materials community because the behavior of the passive oxide layer often dictates the corrosion mechanism inside a nuclear environment. Oxidation occurs when a metal or alloy reacts with an oxidizing atmosphere under the driving force of the free energy of formation of the oxide. A continuous oxide scale can form on the surface of the metal. This has the potential to create a barrier to impede the reaction between the substrate and the environment, but protection depends on the rates of transport of reactants through the oxide layer, and on its mechanical integrity. If the passive scale breaks down, oxidation can occur at an excessive rate, severely degrading the component.

The diffusion of defects plays a centrally important role in regulating the effectiveness and establishing the limits of corrosion protection. Diffusing ionic defects can include Frenkel defects and Schottky defects. Frenkel defects occur as vacancy and interstitial pairs in the lattice, while Schottky defects occur where an equal number of negatively-charged cationic and positively-charged anionic vacancies are present. Once a barrier oxide scale has formed, its continued growth at elevated temperatures is dependent on defect diffusion through the oxide scale as long as the passive scale does not crack and allow molecules from the corrosive media to

penetrate directly to the underlying metal. For a continuous, adherent, compact oxide, the rate of oxide growth is governed by the rate of diffusion of the fastest-moving defect species, otherwise known as the predominant charge carrier. [38] Significant theoretical, experimental, and modelling efforts have been undertaken to understand the nature of ionic defects that control oxidation and to predict their diffusion mechanisms. The Point Defect Model (PDM) is one such model that captures the growth and breakdown rates of passive films that form on the surfaces of reactive metals in contact with corrosive environments. [39] Understanding dynamics of point defects during passive layer growth and within corrosive media is key to understanding corrosion protection. This dissertation will focus on corrosion and oxidation for nuclear structural materials (particularly chromium and iron), and how irradiation and oxidation work together in tandem to change defect properties of grown oxides.

Chromium has been widely studied and implemented because the passivating chromium oxide film formed during oxidation can be highly corrosion resistant [40-43]. For corrosion resistance, chromium is generally added to stainless steels to obtain a passive film rich in chromium oxide, Cr_2O_3. Point defects play an important role in regulating the effectiveness and establishing the limits of Cr_2O_3 corrosion protection, so significant theoretical, experimental, and modelling efforts have been undertaken to understand the nature of point defects that control oxidation and their diffusion mechanisms. [44-60] Several theoretical efforts have focused on growth kinetics of the oxide layer. [44-46] However, there is still a large spread in the reported self-diffusion coefficients and defect formation energies from various experimental studies. [46-56] In recent years, some modelling efforts have focused on self-diffusion coefficients in pure Cr, Cr_2O_3, and Cr-containing alloys using density functional theory. [57-60]. However, the nature of ionic transport and the predominant charge carrier in Cr_2O_3 are disputed due to the strong dependence on the experimental conditions such as temperatures, oxygen partial pressures, and impurity rates. Therefore, divergent conclusions have been drawn in different studies for the diffusion of elements and ionic species in Cr_2O_3. Experimentally identifying the predominant charge carrier and defect characteristics in Cr_2O_3 would improve the understanding of the corrosion protection mechanism for this important oxide.

Like chromium, iron-based alloys react with oxygen or water vapor at high temperature to form an oxide film covering the metal surface, and this oxide layer also functions as a barrier and separates the alloys from the corrosive medium to protect materials from corrosion [62, 63]. For example, when austenitic stainless steels are exposed to a primary nuclear water coolant environment, a passive film composed of an inner $FeCr_2O_4$ spinel and an outer Fe_3O_4 magnetite formed on the surface of steel protect it from further corrosion [63-67]. Figure 2.9 shows this duplex oxide layer and magnetite layer clearly in a TEM cross-section micrograph [67]. In reality, oxide scales are not uniform, featureless, parallel-sided films but possess microstructure (grain structure, pores, dislocations, cracks). Diffusion is faster along these microstructural features, often called “fast paths”, than through the lattice and fast path diffusion tends to dominate the oxidation process at low and intermediate temperatures (under 800^{o}C) [38]. For example, if grain boundaries are the dominant diffusion paths, then the grain structure of the oxide layer, its initial grain size, and subsequent grain growth are important as they effectively control the oxidation

rate. While the diffusion along fast paths such as grain boundaries is well understood, the defect concentrations across oxide interfaces remains to be investigated.

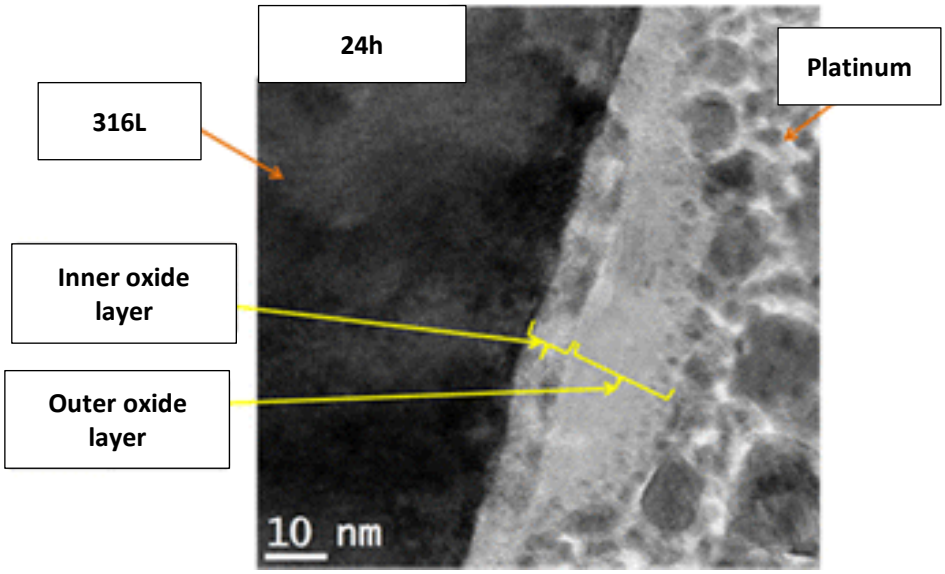

Figure 2.9: Bright field TEM micrograph of oxide layers formed on a 316 alloy in a simulated PWR environment (at 325 °C for 24h) showing a passive film composed of an inner $FeCr_2O_4$ spinel and an outer Fe_3O_4 magnetite. [67]

Moreover, the technological importance of these protective oxide films prompted widespread investigation of their microstructures and conductivity [62-69]. Increasing the oxidation time at a constant temperature can also improve the corrosion resistance of the oxide scale in corrosive media such as liquid lead-bismuth eutectic (LBE) [68]. It was found that not only the basic structure is important to passivity, the defects inside the oxide films also play a critical role for its protective properties [70,71]. It follows that defect behavior at different interfaces, including metal/oxide and mixed oxide interfaces could be critical to the oxide growth. However, discussions of oxide layers are limited to simulation and experimental charge transport studies across the entire oxide, even though the point defect behavior within different parts of the oxide may be different from behavior at the oxide interfaces. This unfortunately leads to limited understanding of all oxide interfaces, especially in mixed oxides with multiple different interfaces, phases, and/or stoichiometry. Depth-dependent experimental studies on oxide interfaces are necessary in order to understand defect behavior and ultimately the corrosion performance of different metals for safety and corrosion protection of new and existing nuclear structural materials. Experimentally verifying the defect behavior during in iron oxide growth and at oxide interfaces would improve the understanding of the corrosion protection mechanism.

As for combined investigations of irradiation and corrosion effects, there are a select few studies that investigate these coupled effects on nuclear materials. These experimental studies are designed to better replicate in-situ reactor conditions with both radiation and corrosion in mind.

It is only in coupled extreme studies that one can begin to isolate and verify the dominant effects of each extreme within the studied environment. Frazer et al. [72] studied the irradiation and corrosion coupling effects on the corrosion behavior of proton-irradiated HT-9 ferritic/martensitic (F/M) steel in static liquid LBE at 420-450^{o}C and found that irradiation enhanced the oxidation of these materials. Deng et al. [73] studied the effect of irradiation on corrosion of 304 SS in a primary nuclear water coolant environment and found similarly that irradiation enhanced the oxidation of materials. However, Jiao and Was [69] found that in 316 SS in a simulated boiling water reactor environment (which is compositionally similar to 304 SS but grows a different oxide, α-Fe_2O_3), proton irradiation did not greatly enhance oxidation. They did however, report a large oxidation dependence on grain orientation. Therefore, irradiation can induce microstructure and compositional modification and alters defect densities in materials, so it must also affect the passive behavior of oxides formed on the surface of alloys [74]. It is of particular concern to determine which of the charge carriers within the semiconductor oxide serves as the predominant charge carrier, driving oxidation growth.

A critical gap in knowledge of the interplay between irradiation and corrosion effects is highlighted by the fact that no models of corrosion explicitly account for radiation damage, particularly the effect of radiation dose or dose rate, or the resulting changes in defect content and microstructure. Radiation damage clearly changes corrosion rates, but studies that attempt to reveal the fundamental mechanisms of radiation-affected corrosion are few in number [75]. Oxidation can be modified significantly by preexisting radiation damage but predicting the extent to which such effects evolve and affect overall defect concentration is not currently well documented. Furthermore, the experimental literature interestingly points to threshold temperatures at which the effects of radiation on corrosion become minimal. [76, 77] Understanding exactly what dictates this critical temperature, as is done for critical pitting temperatures for conventional metal corrosion, would provide new insights for materials design. Thus, a fundamental understanding of the interactions between irradiation and corrosion is needed to better predict the performance of current materials and to develop new materials for future nuclear reactor application.

2.3 Positron spectroscopy of defects

Positrons are a well-known, nondestructive analytical probe for quantifying point defects and dislocations in materials. Positrons enter a solid and annihilate with electrons, and they are further sensitive to local electron density within individual defects. The annihilation process is nondestructive to the material, which is a major advantage as an investigative tool. The size of vacancy-type defects that can be sampled by positrons varies in size from voids down to monovacancies. This is because vacancy regions with reduced electron density will have fewer positron interactions. Positron annihilation spectroscopy (PAS) is the technique using positrons' interactions with local electron density to estimate vacancy concentration within materials.

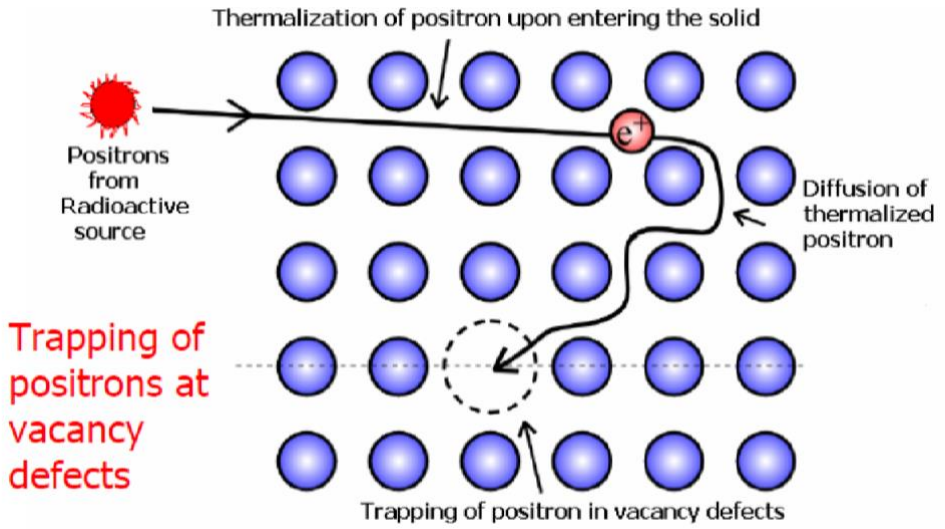

Figure 2.10: Schematic of positron entering and trapping inside a material. When a positron penetrates into a solid, it loses its kinetic energy (thermalizes) quickly, then diffuses through the interstices of the lattice. Diffusion occurs until positrons either become delocalized in Bloch states in the "bulk" material or become localized in an open volume defect site lacking positive charge (trapping). Positrons are finally annihilated by meeting one of the surrounding electrons in the lattice. [78]

The theory behind positron stopping is well-studied. When a positron penetrates into a solid, it loses its kinetic energy by ionization, excitation of electrons, and scattering at phonons until its energy is decreased down to the thermal energy, 3/2 k_bT, i.e.≈0.04 eV, at room temperature [BG15]. This process is called thermalization, and in metallic materials it takes only a few picoseconds [BG15], as shown in Figure 2.10 [78]. The positron implantation profile is described by the exponential probability density function, P(z), in Equation 2.7 [79]:

$$P(z) = \frac{mz^{m-1}}{z_0^m} e^{\left[-\left(\frac{z}{z_0}\right)^m\right]} \tag{2.7}$$

where z is the depth from the sample surface, $\bar{z}$ is the mean stopping depth, and m is a material dependent parameter with empirical value approximately equals to 2. The parameter z_0 is a function of incident positron energy in Equation 2.8.

$$z_0 = \frac{\bar{z}}{\Gamma\left(\frac{1}{m}+1\right)} \tag{2.8}$$

The mean penetration depth of positrons, $\bar{z}$, is given by the Makhov positron stopping expression as a function of positron implantation energy, E and using Equation 2.9 [79,80].

$$\bar{z} = \frac{A}{\rho} E^n \tag{2.9}$$

where A = 3.6 μg/cm^2 keV$^{-1.6}$ and n = 1.6 are independent empirical parameters [80], and ρ is the material density. Considering the density to be 7.874 g/cm^{-3} for pure iron, an example stopping profile at different positron implantation energies (5 keV, 10 keV, and 15 keV) is given in Figure 2.11. This stopping profile does not assume subsequent diffusion of positrons or formation of positronium.

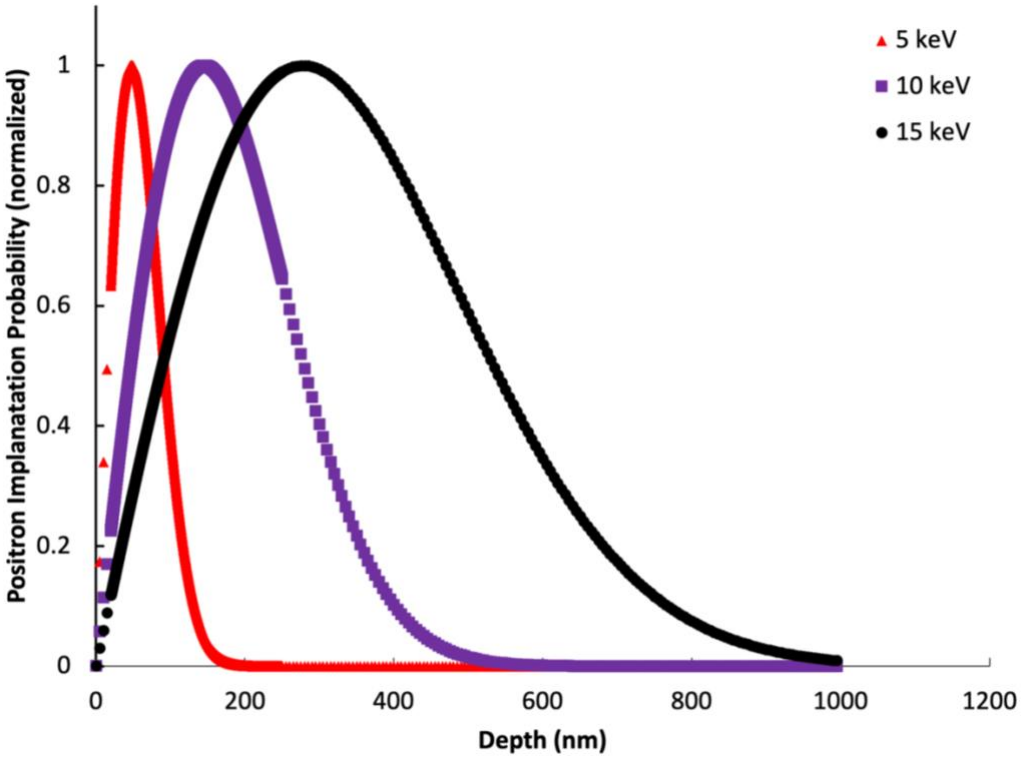

Figure 2.11: Mahkov positron implantation profiles for 5, 10, 15 keV implanted positrons in Fe (normalized). The peak of the implantation profiles increases with implantation energy. [79]

Implanted positrons will either backscatter off the surface of the material or implant into the material. Upon entering the sample, positrons again rapidly lose all their kinetic energy and thermalize (usually in the order of a few picoseconds) due to nonelastic interactions. After thermalization, positrons freely diffuse through the material density. Significant positron diffusion (more than 100 nm) occurs within the interstices of the material because of repulsive forces from the positive nuclei. Diffusion occurs until positrons either become delocalized in Bloch states in the "bulk" material or become localized in an open volume defect site lacking positive charge (see Figure 2.10). This localization of a positron within an open-volume defect in the lattice is called trapping. Positrons are finally annihilated by meeting one of the surrounding electrons in the lattice. The annihilating electron-positron pair is converted in the most cases into two annihilation γ-rays. Vacancy defects are the dominant trapping sites for localized positrons because the missing nucleus positive charge creates a deep negative potential well for positrons. The difference in annihilation characteristics for positron trapping at open-volume defects

compared to those annihilating from delocalized Bloch states is a central feature of PAS techniques, as is the annihilation parameters for trapped state positrons are characteristic of the defect type. It is the measurement of the annihilation γ-rays that allows for positron annihilation spectroscopy studies of defects. Moreover, it is the difference in the annihilation characteristics between a positron annihilating in the delocalized bulk versus a localized vacancy defect trap that allows for PAS measurement of different defect concentrations.

2.4 Positron annihilation spectroscopy

PAS is a technique that can identify vacancy-type defects and dislocations in materials, revealing their size, structure, and concentration with a remarkable sensitivity of 10^{-7} defects per cm^3 [81]. This remarkable sensitivity to defects is due to positrons' long diffusion length, more than 100 nm in most materials, which allows a positron to probe about 10^7 atoms before annihilation [82]. Another major advantage is that PAS is a nondestructive technique, and it is not sensitive to local variations of the lattice constant, as in the case of x-ray diffraction, which may interfere with the measurement of radiation-induced defects. It mainly probes defects without distracting from changes in the phase. Because positrons are sensitive to changes in local electron density, they can even be used to detect dislocation loops. Notably however, interstitials are not detected by positrons because interstitials do not provide a deep enough electronic trap. Positively charged vacancy type defects are also undetected either because they are repulsive electronic traps, or they can even repel incoming positrons.

For measurable vacancy type defects, PAS can reveal the early stage of defects' formation and follow their evolution because of its remarkable sensitivity and capability to distinguish between a defect's number of vacancies from one vacancy up to a cluster of 100 [83]. Furthermore, the ability of PAS to sample atomic electrons and measure their momenta makes it a unique technique for monitoring the chemical environment of defects and probing atomic-size precipitates [84]. Positron annihilation offers a number of spectroscopies that together provide invaluable information on defect density, structure, characteristics, and even chemical identity [85-88].

In practice, positron spectroscopy on materials uses two main techniques, Doppler Broadening spectroscopy (DBS) and positron annihilation lifetime spectroscopy (PALS). DBS is based on detection of the 511 keV characteristic annihilation γ-rays. The Doppler shift is measured by the broadening of the 511 keV peak in annihilation γ-rays resulting from the annihilation event with an electron. The broadening of this peak from electron annihilation represents the electron momentum distribution seen by positrons and is very sensitive to the presence of vacancies, as positrons trapped in vacancies mainly annihilate with the low-momentum valence electrons leading to less broadening.

For DBS, the S-parameter indicates the relative contribution in the 511 keV peak from valence and conduction electrons while the W-parameter represents the relative contribution from core electrons. The S and W parameters are calculated from the shape of the 511 keV peak as follows. S is calculated by dividing the counts in the central region of the peak to total counts in the peak,

and W from dividing the counts in the two wings of the peak to the total counts in the peak, as illustrated in Figure 2.12. For HPGe detectors with energy resolution around 1 keV at the annihilation line, 511 keV, the cutoff energies for the peak are 511 ± 0.70 keV and 508.56 ± 0.30 keV and 513.44 ± 0.30 keV for the wings, respectively. S is higher for positrons trapped at and annihilated in open-volume defects. [89] Doppler broadening mainly provides information on the overall defect concentration, and coincident Doppler broadening can provide information about the local chemical environment of defects.

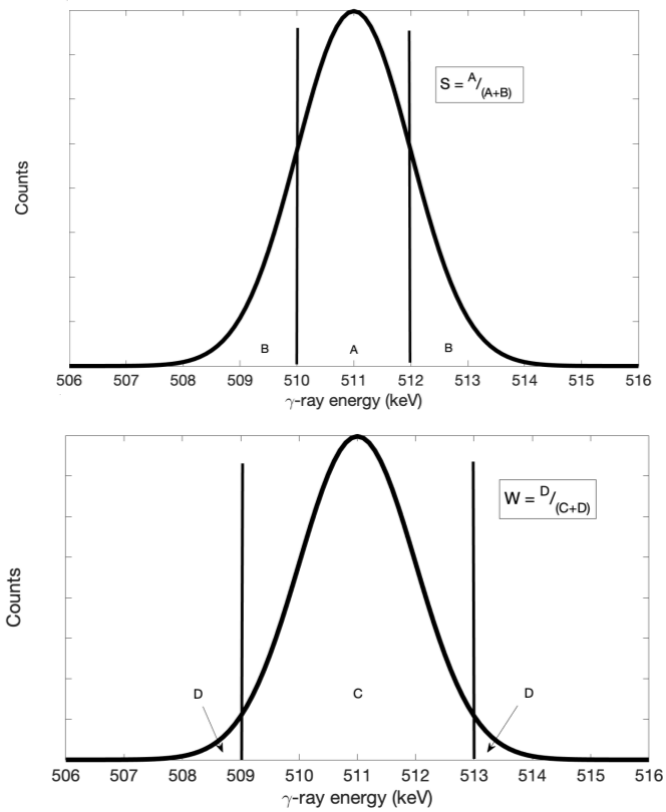

Figure 2.12: DBS calculation of the S and W parameters from the detection of the 511 keV characteristic annihilation γ-rays.

The second type of positron spectroscopy is called positron annihilation lifetime spectroscopy (PALS), which uses the time difference between a positron entering a material and the annihilation gamma to quantify the defect size and level. A schematic is also shown in Figure 2.13. These time differences correspond to the lifetimes of individual positrons. The lifetime of positrons trapped in defects will depend on the average electron density in the defects. The larger the defect size, the longer the lifetime because the longer it takes for a positron to annihilate and find an electron. The more defects there are, the more 511 keV signals will come at that defects annihilation rate. In principle, each type of defect gives rise to a characteristic positron lifetime, and by measuring these lifetimes, information is obtained about the size and concentration of the defects.

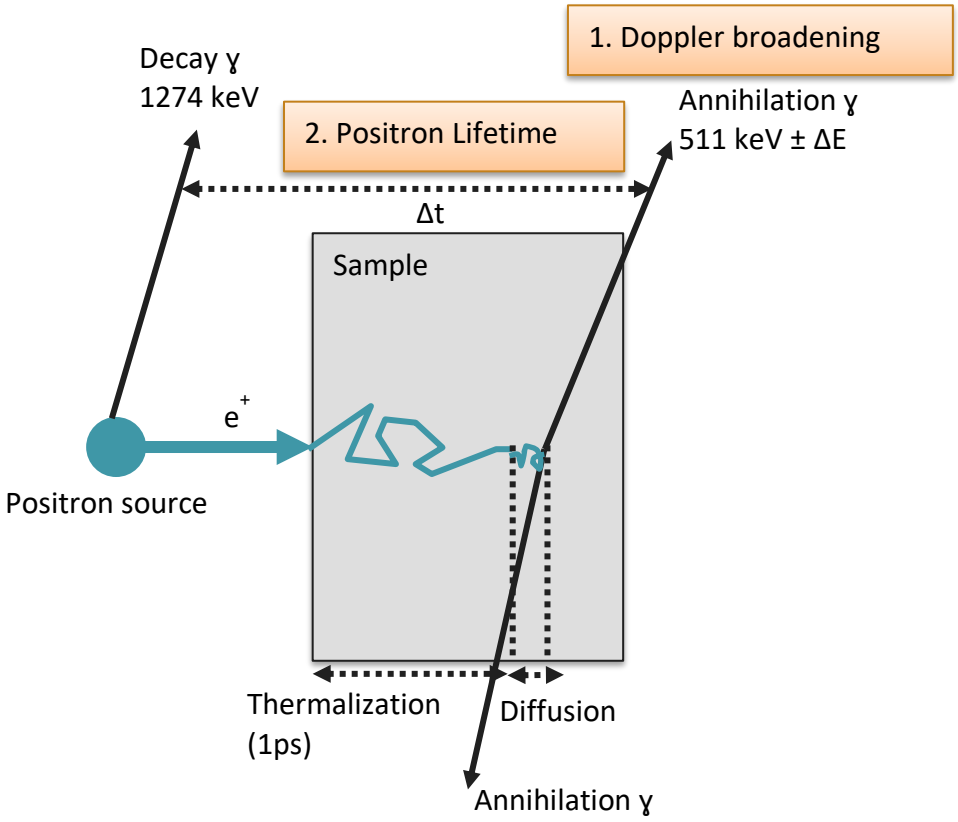

Figure 2.13: Schematic of positron spectroscopy techniques. 1) Doppler broadening spectroscopy (DBS) measures the Doppler shift of the 511 peak from electron annihilation and is very sensitive to the presence of vacancies, as positrons trapped in vacancies mainly annihilate with the low-momentum valence electrons leading to less broadening 2) Positron annihilation lifetime spectroscopy (PALS) uses the time difference between a positron entering a material and the annihilation gamma to quantify the defect size and level.

A positron trapping model was developed based on solving a coupled system of partial differential equations to facilitate defect density calculations from PALS measurements [83]. It assumes that a given number defect types are present and homogenously distributed in the material. It also assumes no saturation of positron trapping. Each defect type leads to a characteristic positron lifetime, τ_D, and a calculated positron trapping rate, K_D. In the two-state simple strapping model example, where there is only one type of defect, the positron trapping rate can be calculated according to Equation 2.9 [89]:

$$K_D = \frac{I_D}{IB}\left(\frac{1}{\tau_B} - \frac{1}{\tau_D}\right) \tag{2.9}$$

where τ_B and τ_D are the bulk and defect lifetimes, respectively, and I_B and I_D are their measured intensities. The trapping rate is proportional to the defect density, so defect concentration, C_D, for a given defect type can be calculated from Equation 2.10 [89].

$$C_D = \frac{K_D}{\nu_D} \tag{2.10}$$

where ν_D is the trapping coefficient (specific trapping rate for each defect type) which is determined computationally or experimentally from an independent reference method. The characteristic lifetimes for different metal defect can also be either calculated or found from previous positron experiments [90-93]. This enables the defect identification (e.g., the concentration and size of a vacancy cluster) from the measured lifetime value. From the PALS data, a typical PALS lifetime spectrum, N(t), is described by Equation 2.11 [89].

$$N(t) = \sum \left(\frac{1}{\tau_i}\right) \mathrm{I_i} \exp\left(-\frac{t}{\tau_i}\right) \tag{2.11}$$

where τ_i and I_i are the positron lifetime and intensity of the i-th component, respectively (ΣI_i=1). More details about the general standard trapping model for any number of defects are given in Čížek's 2018 review of PAS [89].

In practice, a lifetime spectrum is a histogram of positron annihilation events occurring in certain time intervals. An example positron lifetime spectrum measured on a plastically deformed steel is shown in Figure 2.14. The time measures the difference between the start and the annihilation γ rays (Δt in Figure 2.13). An overall spectrum fit is completed first, as in the red line in Figure 2.14. The overall lifetime spectrum fit can then be calculated as a sum of exponential components with relative intensities, I_i, and lifetimes, τ_i, according to Equation 2.11. This example spectrum consists of a free positron component with lifetime τ_1 = (15 ± 2) ps and a contribution from dislocations with lifetime τ_2 = (154 ± 1) ps. The source contribution is plotted by dotted lines and consists of two components representing a contribution of positrons annihilating in the positron source spot and the covering foil. Residuals are expressed in units of one standard deviation are also plotted in the upper panel of Figure 2.14.

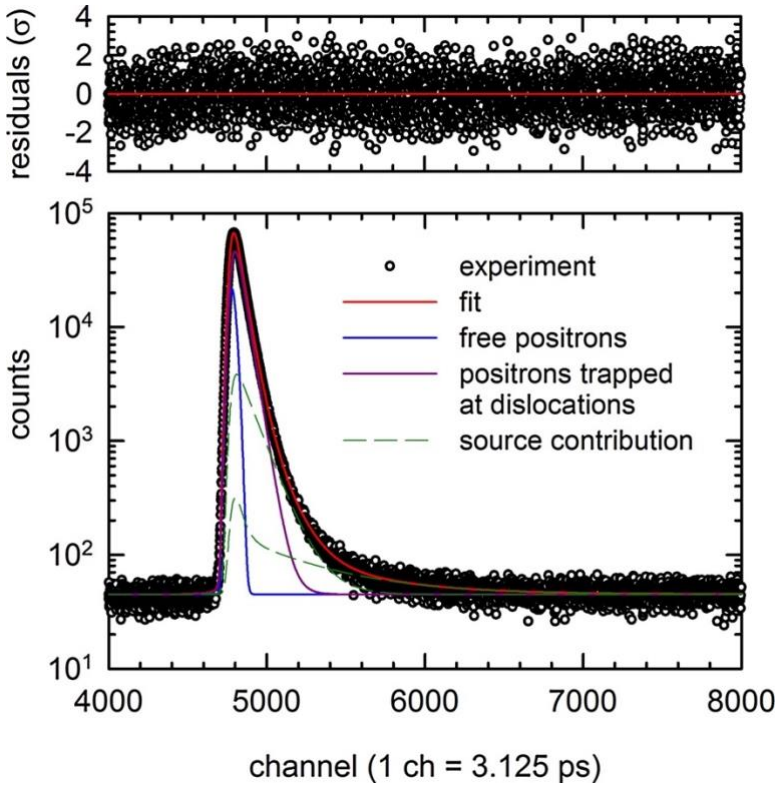

Figure 2.14: An example of PALS lifetime spectrum measured on plastically deformed steel. Fit of the spectrum is plotted by a thick solid line. Then, overall lifetime spectrum fit can then be calculated as a sum of exponential components with relative intensities, I_i, and lifetimes, τ_i, according to Equation 2.11. Residuals expressed in units of one standard deviation are plotted in the upper panel. [89]

Part of the work in this dissertation examines in-situ radiation damage with PAS measurements to investigate the mechanism for monovacancy formation. Displacements formed during the ion beam irradiation damage cascade are expected to relax and agglomerate into larger, surviving vacancy clusters that can be easily observed with PAS. Section 2.5 will highlight both ex-situ and in-situ radiation damage studies previously done using PAS.

Other methods measure indirect effects of defects on material properties, such as electrical resistivity, while positron directly probes vacancies and clusters [94] with an atomic resolution that cannot be attained by TEM. These methods will be briefly discussed in Section 2.7. However, PAS is a unique technique for monitoring defect formation and evolution on the atomistic level.

2.5 Radiation damage studies using PAS

This section highlights important radiation damage investigations using PAS in order to demonstrate how PAS has improved the understanding of irradiation defects. PAS has previously been used to study radiation damage in steels and other nuclear materials, but most studies are ex-situ after neutron or ion beam irradiation [95-97]. Several important mechanisms for defect

formation, kinetics, and interactions have been revealed from PAS measurements. The subsections will be divided by incident particle type: neutrons, helium, and heavy ions. The final subsection will cover in-situ ion damage investigations.

2.5.1 Neutron irradiation damage studies using PAS

Previous PAS studies on Fe-Cr alloys [98] and reactor pressure vessel (RPV) steels showed the utility of the PAS technique to probe extended defects in irradiated steels [99, 100]. In both cases, defect mobility was driven by dose rate and temperature, leading to irradiation hardening at higher observed doses. The studies suggest point defects and vacancy cluster defects induce the formation of dislocation loops. On Fe-Cr steels, Lambrecht and Malebra revealed that the main effect of Cr is the reduction of vacancy population compared to pure Fe, thus hindering vacancy cluster formation. [101] Previously, it was well-known from studies performed at high irradiation doses and temperatures that void swelling is significantly suppressed by adding Cr to Fe. But modelling efforts [102-104] had only suggested a mechanism, without experimental verification, that Cr atoms interact strongly with interstitials, and as a consequence, act as traps for 1-D migrating interstitial clusters which are sinks for vacancies produced in cascades, thereby reducing swelling. Lambrecht and Malebra's PAS results confirmed this mechanism by showing the main effect of Cr addition is to reduce the concentration of vacancies. [101] This PAS finding supports evidence that Cr is the main alloying element that governs the irradiation response of the ferritic/martensitic steels in terms of nanostructure evolution, and thus this study had direct impact to improving the understanding of irradiation performance of ferritic/martensitic steels for next generation fission and fusion reactors.

Looking closely at work done by Nagai et al. on RPV steels, positrons were even used to measure embrittlement from ultrafine Cu precipitates. Copper is known to play an important role in irradiation hardening and embrittlement of RPV materials. [105-110] Considering the RPV is perhaps the most critical safety component in a nuclear reactor, it is critical to understand drivers of RPV embrittlement. While positrons are usually used to measure vacancy-type defects, with just Doppler broadening measurements, this research effort was able to not only detect these sub-nanometer Cu precipitates (not seen by TEM or atom probe tomography, APT), but also reveal their size and chemical composition. This work confirmed the formation of Cu precipitates in RPV steel as a result of neutron irradiation and their recovery after annealing at approximately 650^{o}C. [99,111,112] Even though in-service thermal annealing of the embrittled RPV steels is common practice in several countries [113-115], PAS can be utilized to optimize the in-service annealing condition of the RPV steels from the microscopic mechanism. The PAS technique's potential capability to detect small precipitates is emphasized here as it could be highly useful for the study of precipitates in high-entropy alloys and other emerging novel alloys.

As another notable example, Eldrup and Singh [116] conducted a positron lifetime study to investigate crystal structure's effect on radiation tolerance. This study has direct implications for the understanding of void formation and void swelling in materials as a function of crystal structure. The samples were FCC Cu and BCC Fe irradiated with neutrons to 0.3 dpa at 100^{o}C [116]. After the irradiation, the specimens were annealed to see a difference in annealed

irradiation damage. The hypothesis explored if defects would again become mobile and recombine by the reintroduction of thermal energy into the system, leading to a measurable decrease in samples' positron lifetimes. The positron lifetime spectroscopy saw drastic differences between the Cu and Fe systems, which was later attributed to FCC stacking faults and dislocations acting as sinks for vacancies compared to BCC. Moreover, the effect of annealing in both cases saw decreases in overall defect concentration from positron spectroscopy, validating literature explanations of annealing radiation recovery in materials. [117, 118] This study serves as an excellent example for how positron spectroscopy can be useful for looking at vacancy-type defect behavior and dislocations in nuclear materials. Moreover, PAS is again proven to be an important experimental tool for the validation of results of modelling of radiation produced microstructures. The work in this dissertation seeks to compare defect measurements using PALS and DBS techniques to the theory behind radiation-produced monovacancies.

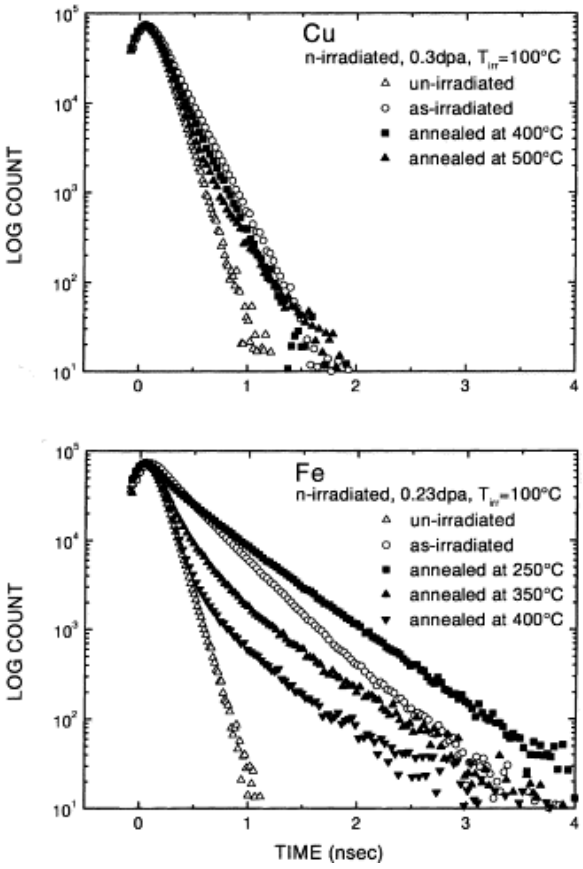

Figure 2.15: Positron lifetime spectra for annealed neutron-irradiated FCC Cu versus BCC Fe. Lifetime increases after irradiation were greater in BCC Fe versus FCC Cu, which can be attributed to FCC stacking faults and dislocations acting as sinks for vacancies compared to BCC. Moreover, the effect of annealing in both cases saw decreases in overall defect concentration from positron spectroscopy. [116]

2.5.2 Helium irradiation damage studies using PAS

Helium is produced at a high rate in stainless steel in LWR nuclear systems by the (n, α) reaction and has been the subject of intense investigation to reveal the fundamental interactions of He in materials. This includes He mobility, He-trapping at defects, and formation of He bubbles. [119, 120] Helium studies are directly relevant for understanding radiation damage in next generation reactors and nuclear fusion applications.

An important study applied depth-resolved DBS to investigate helium ion-induced defects in oxide dispersion-strengthened (ODS) alloys and steels [121]. It revealed the presence of dislocations and open volume defects in the pristine ODS Fe-Cr-Al alloys and measured the size and concentration of vacancy clusters induced by dual irradiation with Fe and He ions. It was found that positrons are a useful tool to study the onset of helium bubble nucleation for the material in the swelling incubation phase. Because positrons can detect smaller open-volume defects than TEM during the evolution of bubbles or void swelling, the technique is also capable of tracking the microstructural evolution before the fluence increases to the point where new internal features emerge in the material bulk, such as large cavities or blisters. This shows how positrons can complement or correlate to TEM data in these conditions. Moreover, the positron lifetime and Doppler broadening results showed a greater positron lifetime increase in the Fe9Cr relative to the ODS sample, shown in Figure 2.16.

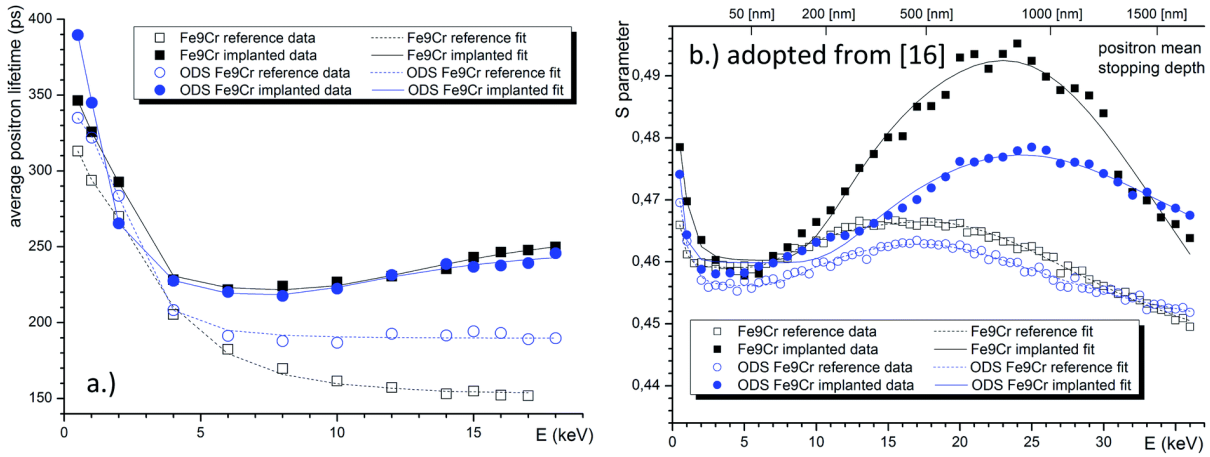

Figure 2.16: Positron lifetime and Doppler broadening results for helium implanted versus reference Fe9Cr versus its ODS variant. Positron lifetimes and the S-parameter increased after He+ implantation for both the Fe9Cr and its ODS variant. Comparing the increases, there is also evidence of the presence of a higher density of recombination centers in the oxide dispersion strengthened steel, suppressing the formation of large defect agglomerations. [121]

This study provided experimental evidence of the presence of a higher density of recombination sites in the ODS alloy suppressing the formation of large defect agglomerations. However, the effect of helium on the reduction of positron trapping at small vacancy clusters is competing with the effect of newly created vacancies, increasing the trapping. Helium stabilizes newly created vacancies and can suppress positron trapping and diffusion at these sites because of the

positively charged helium nucleus. Despite these factors limiting positron trapping, this study emphasizes the PAS technique's capability to investigate the microstructure and irradiation performance of complex materials like ODS alloys. [121-123]

2.5.3 Heavy ion irradiation damage studies using PAS

Ion irradiation is an important surrogate for nuclear material studies for simulating the neutron radiation damage generated in nuclear reactors without inducing radioactivity in materials. Further, defect studies by heavy ion irradiation offer distinct advantages over neutron irradiation, such as control, speed, cost, and production of systematic variations over a wide range of dpa, which facilitate fundamental studies of defect formation and evolution. [124] PAS is again useful for because of the capability to probe large vacancy-type defects down to atomic-scale vacancies, as explained in previous sections. In this subsection, several remarkable examples of depth-resolved PAS measurements in ion-irradiated materials are summarized.

A recent investigation on defects in Fe9Cr irradiated with Fe ions [125] combined depth-resolved DBS with TEM. The study revealed the gradual annihilation of radiation-induced vacancies by the visible dislocation loops in TEM. Small interstitial loops were observed with a large number of vacancies after 0.5 dpa, but at higher damage levels (1.0 dpa and 3.0 dpa), there were sharp decreases in defects measured by positrons. If the coarsening dislocation loops formed in BCC materials act as sinks for the vacancy clusters at high doses, it can explain the suppression of swelling behavior in Fe-based ferritic steels (see schematic in Figure 2.17). This investigation increased understanding of the interaction between vacancies and dislocation loops in BCC materials.

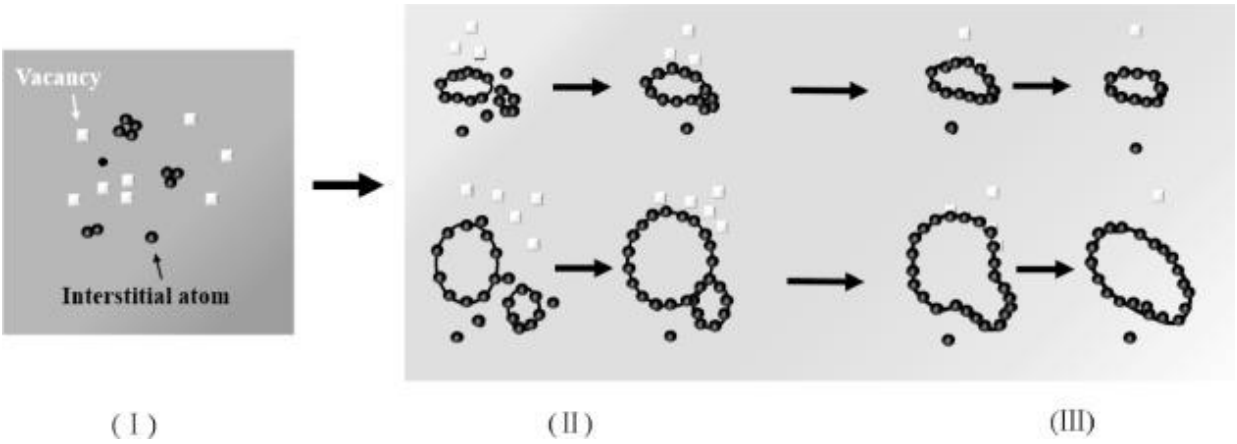

Figure 2.17: Schematic of evolution of dislocation loops and their interaction with vacancies: (I) in initial irradiated stage, interstitial atoms gather into disks and collapse to form interstitial dislocation loops; (II) interstitial dislocation loops coarsened by constantly absorbing interstitial atoms and coalesce the smaller loops directly, and they would gradually close to the surrounding vacancies or vacancies migrate towards loops in the growth process; (III) when interstitial dislocation loops encounter vacancies, they would annihilate/remove them. [125]

Another recent study [126] combined depth-resolved Doppler broadening and positron annihilation lifetime spectroscopies with TEM to identify vacancy clusters in self ion-irradiated Fe and measure their density as a function of depth. PAS measurements revealed structure of vacancy clusters and the change in their size and density with irradiation dose, even despite large voids in the pristine Fe samples. Along with TEM results, there was a correlation between the increase in the density of small vacancy clusters with irradiation and a remarkable reduction in the size of large voids. The radiation damage cascade led to shrinkage of preexisting voids associated with an enhancement in the formation of smaller vacancy clusters. This mechanism highlights the competing effects of different sinks within the material. On the one hand, sinks do eliminate interstitials produced under irradiation. On the other hand, they also exacerbate the formation of vacancy defects.

Another study on thin Fe-Cr films combined positron spectroscopy with TEM and APT to look at high radiation resistance by varying Cr alloying content. [127] The PAS results are given in Figure 2.18. The study revealed that the well-known resistance to radiation in Fe–Cr alloys may arise from vacancy clusters stabilizing around Cr atoms, which then act as sinks for radiation-induced defects. Cr atoms were found to not act as a sink for interstitials, but instead form defect complexes with vacancies. These complexes would act as sinks for irradiation-induced vacancies and interstitials. Also, lower Cr content yielded smaller defect clusters which were efficient sinks for radiation damage, but larger quantities of Cr formed a defect structure that was less homogenous and larger in size, resulting in less efficient damage recombination.

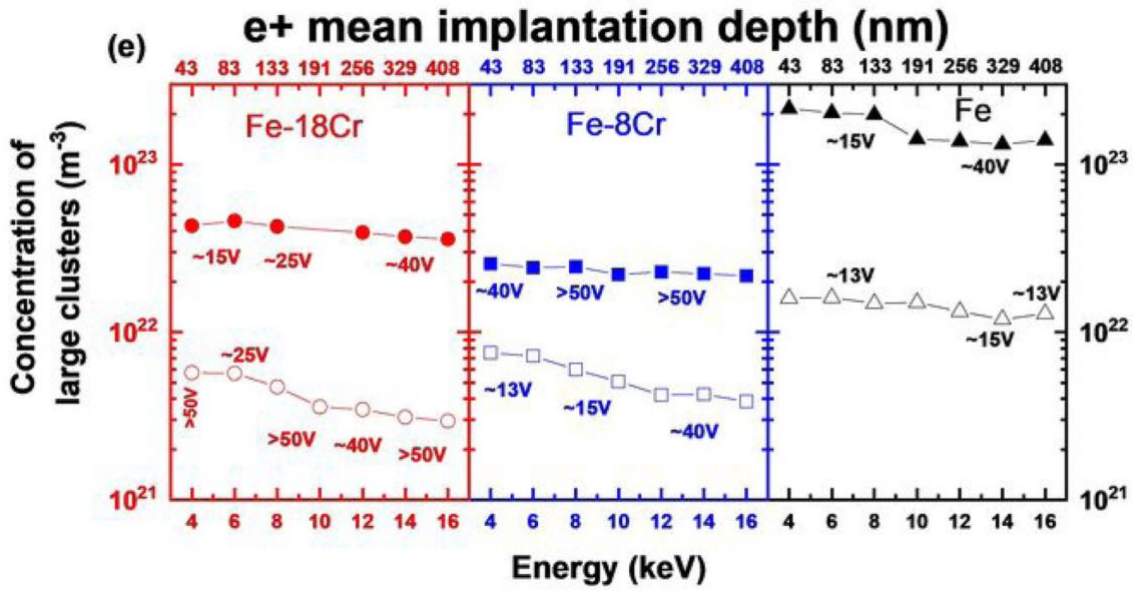

Figure 2.18: Comparison of large vacancy clusters before and after 0.06 dpa irradiation in Fe-Cr alloyed samples versus reference Fe. Irradiated values are in filled symbols. Irradiation is found to increase the concentration of large clusters in all cases, and there is a strong effect of

Cr alloying on reducing the concentration of vacancy clusters (not observable with TEM) induced by irradiation. [127]

2.5.4 In-situ ion irradiation damage studies using PAS

Despite advances with ex-situ irradiation measurements such as the studies detailed above, in-situ experiments are still needed to understand the true defect content of materials during irradiation, as that will drive the materials' response in a number of contexts, including irradiation environments with added corrosion, pressure, or stress. Ex-situ experiments cannot give the same level of understanding because of the small size, high mobility, and inherent instability of defects outside of the radiation damage cascade.

Currently, there are limited experimental facilities to perform the needed in-situ measurements. Previous in-situ experiments have been limited to just Doppler broadening PAS [128-130] using low energy slow positrons with low penetration depth [131, 132]. Iwai and Tsuchida et al. [133] reported on the construction of in situ PAS with ion irradiation and the possibility of performing in-situ DBS during ion irradiation. They investigated Ni, Fe, and Al with DBS during ion beam on and ion beam off and observed promising in-situ behaviors only in Ni, but not in Fe and Al [131, 134]. The measurements showed a difference in the S-parameter value of Ni between the ion beam on and ion beam off. An interesting temperature dependence for vacancy clustering in Ni was also observed. Other in-situ DBS efforts were performed, but they still only focused on comparing the S and W parameters with the ion beam on versus off.

2.6 Defect studies in oxides using PAS

In general, PAS is also a popular investigative technique to investigate oxides and other semiconductors. Positron annihilation spectroscopies have been widely applied to study materials such as SiC, ZrO_2 and ZnO. [135-138]. Cation vacancies in oxides are readily observable, and in fact they have been shown to be responsible for many optoelectronic properties of these compounds. [139] However, oxygen vacancies are small and positively charged, and therefore not readily observable with positively charged positrons. In addition, the possibility of metal vacancy–oxygen vacancy complexes with multiple oxygen vacancies makes detailed defect identification difficult.

As for irradiated oxides, outside of silicon, defect characteristics are not well understood in these materials and dedicated PAS studies are scarce in the literature. One notable study by Haseman et al. [140] was conducted on neutron irradiated ZnO. It was found that the neutrons created vacancies which then further clustered into vacancy clusters and large voids. The large increase in positron lifetime indicated a void size of about 100 vacancies, highlighting the capability of positron lifetime measurements to quantify void sizes in irradiated oxides such as this.

Another notable study by Derby et al. on iron-oxide thin films combined PAS with grazing incidence X-ray diffraction (GIXRD) and four-dimensional scanning/transmission electron

microscopy (4DSTEM). [141] Specifically, the study looked at defects in iron oxides grown from physical vapor deposition (PVD) or thermal oxidation in air. It was found that oxide defect concentration is largely dependent on initial defect structure. PAS data showed that formation of vacancies and vacancy clusters during growth increases as the crystallinity in the film decreases. The dense, single-crystal PVD oxide contained the fewest number of structural defects and the smallest positron lifetime, as there are no grain boundaries or large voids in this film. This film should contain only lattice defects formed during growth. [142] On the other hand, the polycrystalline, thermally grown oxide was the only sample with large voids. This indicated that oxide defect content depends greatly on oxide growth conditions. Thus, how the oxide forms during corrosion is dependent on the initial defect concentration in the material, so preexisting defects have a profound impact on overall material performance.

Beyond just oxide growth, this dissertation is also sought to expand the capability of PAS to study radiation tolerance of these oxides. Doppler broadening spectroscopy can be developed to infer overall vacancy-type defect concentrations from irradiation in oxides. Moreover, novel PALS observations of aged oxide layers were developed to measure predominant defect types and defect dynamics from irradiation on oxidized materials. The discussion here is primarily focused on point defect behavior during oxide growth, and not the corrosion mechanism or defect transport within different layers of the oxide. However, defect content from irradiated oxides has direct relevance to corrosion mechanisms. Sickafus et al. hypothesized that an oxide's radiation tolerance will depend on the chemistry of the oxide, and the oxide's crystal lattice disruption from non-equilibrium radiation defects [143, 144]. Amorphization is the ultimate failure mode from lattice disruption, which could lead to a volume change in the component and the ultimate failure of a material during use [145]. Understanding an oxide's stability under irradiation is dependent on the lattice stability during the accumulation of point defects and the survival rate of unstable non-equilibrium point defects [146, 147].

2.7 Alternative point defect measurement techniques

Other than PAS, experimental techniques quantifying displacement damage are mostly indirect, including differential dilatometry [148], electrical resistivity measurements [149, 150], or short, intense ion beam pulses [151]. However, it is worth it to compare their merits in terms of sensitivity, resolution, the ability to directly identify defects, and the ability to measure interstitial point defects. Sensitivity is defined here as the ability to measure a vacancy cluster vs a set of individual vacancies. Resolution is defined as measuring the smallest vacancy sizes (e.g, one monovacancy). The merit of each technique is summarized in Table 2.4 at the end of this section.

First, differential dilatometry is just a very precise length measurement of a thin wire with defects heated up compared to the thermal expansion of a reference sample to see the difference in the dimensional change due to vacancy presence, as shown in Figure 2.19 [148]. The difference Δl_V of the length change between the deformed sample (shaded in Figure 2.19) and an undeformed reference sample upon linear heating is due to the irreversible annealing out of deformation-induced free volumes. The irreversible contribution Δl_V is superimposed to the reversible linear thermal length expansion Δl_t. By subtracting the expansion difference between the deformed

and undeformed sample and assuming a uniform defect type, the size and concentration of said defects can be calculated. The approach works for larger voids, this is not a suitable method for differentiating between point defect clusters or small monovacancies because it assumes a standard defect identity a priori.

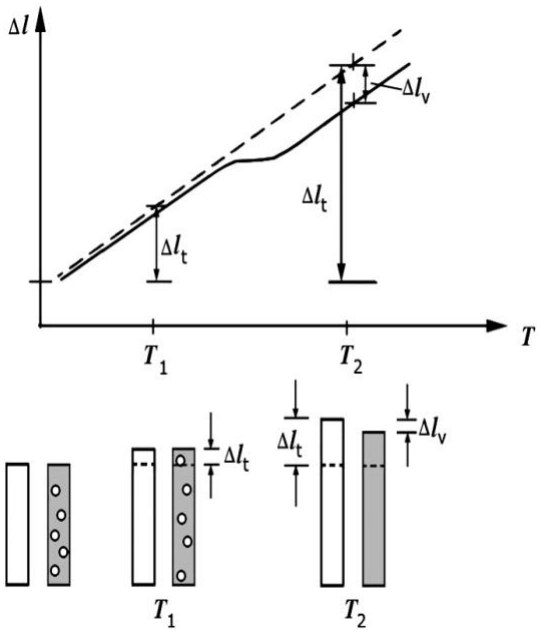

Figure 2.19: Schematic of a differential dilatometry experiment. By measuring the difference Δl_V of the length change between the deformed sample (shaded) and an undeformed reference sample (unshaded) upon linear heating is due to the irreversible annealing out of deformation-induced free volumes. [148]

Second, electrical resistivity measurements take advantage of the conductivity of the material. Point defects interrupt the electrical conductivity of the material as obstacles to electrical current, so the absolute resistivity difference can be calculated as a function of temperature to measure the defect's resistance. [149, 150] Similar to dilatometry, precise resistivity measurements are taken as a function of temperature. An example study on aluminum is shown in Figure 2.20 [149]. The resistance difference, Δρ, between the sample before and after linear heating is due to the reversible introduction of thermal defect volumes. Assuming a uniform defect type, the concentration of said defects can be calculated. This method is not sensitive to detect the difference between an array of vacancies versus vacancy cluster, but it has been used to detect monovacancies and their formation energies.

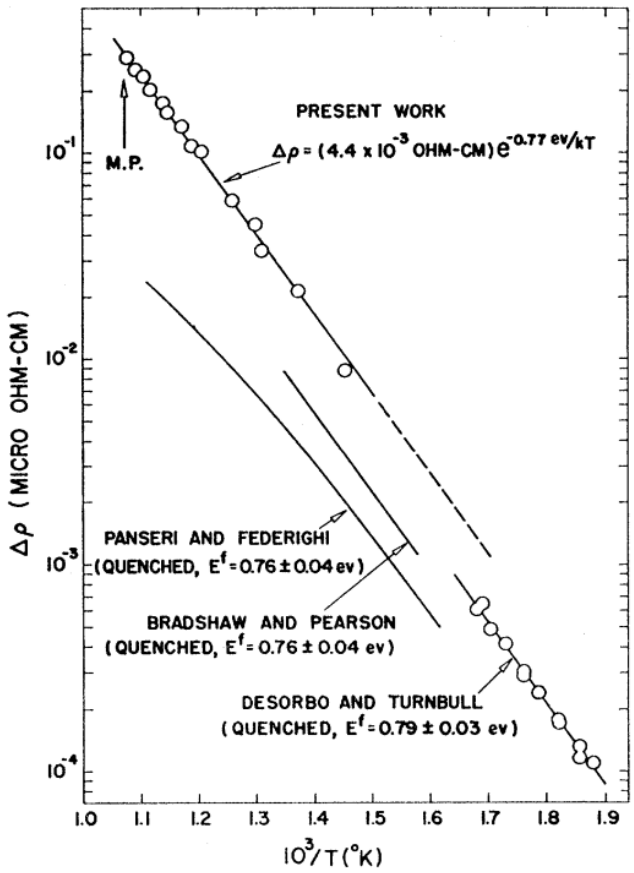

Figure 2.20: Comparison of the residual resistance values, Δρ, attributed to thermally generated vacancy-type defects in aluminum, from different investigations. The resistivity difference Δρ of a thin wire upon linear heating is assumed due to the reversible introduction of thermal defects. [149]

Thirdly, there are short-intense ion beam pulses, which utilize ion channeling to measure point defect effects after the displacement cascade. The experimental setup features an incident ion beam, which, if angled correctly, causes the incident ions will channel somewhat deeper into the material if they arrive parallel to the major crystal orientation. Ions travelling the interstices in between atoms, called channels, may experience little to no energy loss and stop deeper into the material. But, if there are defects within the lattice, the ion will not channel in the first place, or dechannel. Figure 2.21 [151] features a study done with incident lithium ions into silicon. The effect of channeling will appear as a bimodal ion distribution within the material after irradiation and a plateau between those two peaks, indicating the presence of the channels. However, if radiation damage from the incident ions in the short, intense pulse disrupts the lattice structure in the sample, there will be no channeling. The broad depth plateau seen in the longer irradiation time disappears and there is only a single damage peak, which resembles many damage simulations of incident ions where channeling is not expected. This method looks more directly at the recombination of point defects and the survival of the damage cascade, but it is not currently sensitive enough to measure or resolve individual point defects.

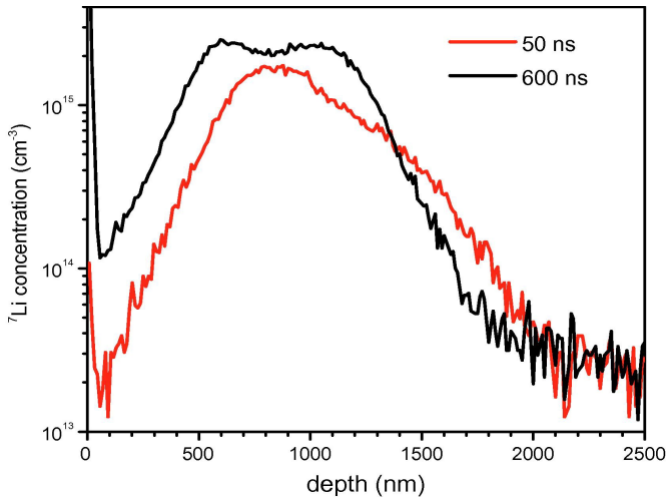

Figure 2.21: Depth profiles of $^7Li^+$ ions implanted into silicon under normal incidence. The black curve corresponds to a longer ion pulse length of 600 ns in which channeling can be observed from the bimodal ion distribution. The shorter pulse length 50 ns curve disrupts channeling, so only one peak is present. [151]

	Differential Dilatometry	**Resistivity**	**Short-intense ion beam**	**Positron Annihilation Spectroscopy**
Sensitivity (Array of vacancies vs. vacancy cluster)	No	No	No	Yes
Monovacancy Resolution	No	Yes	No	Yes
Direct Identification of Defect Type	No	No	No	Yes
Interstitial Defects	Yes	Yes	Yes	No

Table 2.4: Comparison of the various capabilities of positron annihilation spectroscopy and three alternative point defect measurement techniques: Differential dilatometry, resistivity, and short-intense ion beams. Sensitivity, monovacancy resolution, direct identification of defect type, and measurement capability of interstitial defects are compared.

3. Research Objectives

This research seeks to advance fundamental understanding of radiation damage phenomena in structural materials for nuclear reactor applications. These research advances have tangible impacts for not only nuclear reactors, but also nuclear waste storage, nuclear fusion, semiconductor processing (implantation), and medical isotope production. Ideally, design teams evaluate component integrity and material properties after simulating a complex set of perturbations. However, failure predictions are complex because they rely on interdependent physical models. For example, radiation damage and thermal stress may work in concert to degrade a 304 stainless steel baffle bolt such that nucleated void sizes are dependent on the temperature of the irradiation. The localized failure of a baffle bolt could create irregularities in flow of coolant through the reactor core, ultimately reducing core lifetime. [1] Capturing this interplay of effects is a significant task that is conventionally broken into parts and distributed across the research community at large. This research is to focus on radiation damage in nuclear reactor structural materials, specifically fundamental theory behind radiation damage point defects. This brings two questions. First, how can the population of radiation damage induced point defects be probed at their short-lived, atomic scale that captures and quantifies the influence of the surviving defect population? Second, how can the interplay of radiation point defects and oxidation/corrosion point defects influence overall point defect populations in passivating systems?

The first objective of this research is to validate rate theory predications of radiation damage in-situ defect populations. Most radiation damage studies are ex-situ, in that they feature pre-post or comparison studies of material defects after radiation damage has occurred. This creates a limited understanding of radiation damage point defect behavior without experimental validation of what happens to the point defect population during and after the damage. After all, point defects ultimately determine radiation-induced microstructural and material property changes. Thus, the incomplete understanding limits the current lifetime and safety analysis of major reactor components and the future evaluation of novel reactor materials.

The first hypothesis of this research asserts Wiedersich radiation damage point defect rate theory and radiation damage DFT simulations can be proved or disproved using in-situ positron annihilation spectroscopy. This research sought to experimentally bring new insight to the connection between DFT calculations of defects during radiation damage, theoretical predictions of point defect populations, and post-mortem irradiation studies of defect and material property changes. This hypothesis is explored throughout the remainder of the dissertation by way of simulation, execution, and discission of novel positron annihilation spectroscopy experiments. Confirmations and shortcomings are discussed, and the findings are summarized in the context of the point defect rate theory model.

The second objective of this research is to validate theoretical predictions of predominant defect identities within passivating systems. Oxides are often modelled as semiconductors with a predominant defect type or charge carrier dominating transport in the oxide layer, thus controlling its growth rate. However, discussions of oxide layers are limited to simulation and experimental

charge transport studies across the entire oxide, even though the point defect behavior within different parts of the oxide may be different from behavior at the oxide interfaces. However, this leads to limited understanding of all oxide interfaces, especially in mixed oxides with multiple different interfaces, phases, and/or stoichiometry. Depth-dependent experimental studies on oxide interfaces are necessary in order to understand defect behavior and ultimately, corrosion performance of different metals for safety and corrosion protection of new and existing nuclear structural materials.

The second hypothesis of this research asserts defect measurements from positron annihilation spectroscopy can be used to prove or disprove predominant defect identities and defect distributions within passivating oxide layers. This research sought to experimentally connect DFT simulations of oxide layer defect behavior, electrochemical studies on oxides, and post-mortem irradiation microscopy studies with complementary defect information from positron spectroscopy. This hypothesis is explored throughout the dissertation with the execution of novel positron annihilation spectroscopy experiments and relating those experiments with previous simulations and experiments on known oxide layers. The validations and limits of positron experiments will also be discussed alongside previous studies of oxide layers.

4. Ex-situ PAS measurements and results on nuclear relevant materials

4.1 Positron annihilation spectroscopy methodology

Low energy, depth-resolved Doppler broadening spectroscopy (DBS) and positron annihilation lifetime spectroscopy (PALS) are not very common techniques, so facilities that can perform these measurements are rare. Most of the work presented here utilized the PAS beamline facilities at the Institute of Radiation Physics at Helmholtz-Zentrum Dresden – Rossendorf (HZDR) for experimental positron annihilation spectroscopy (PAS). In order to perform the work at the facility in Dresden, Germany, several user proposals were proposed and awarded. The facility is able to characterize the defect types and their densities at different depths. DBS measurements were conducted at the apparatus for in-situ defect analysis (AIDA) [1] on the slow positron beamline (SPONSOR) [2]. A schematic of the DBS system is shown in Figure 4.1 [3]. Positrons were implanted into each sample with discrete kinetic energies E_p in the range between 0.05 and 35 keV, which allows for depth profiling from the surface down to about 2 µm.

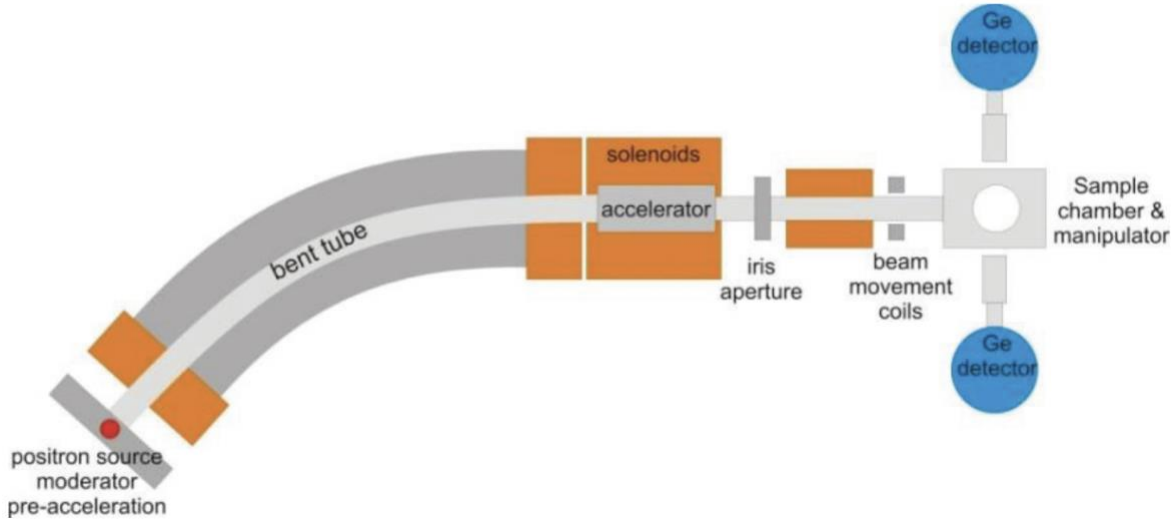

Figure 4.1: A schematic of the Slow Positron System at Rossendorf (SPONSOR) where the DBS measurements were conducted. An Na-22 source is used as a source for positrons, which are then magnetically guided toward the sample with solenoids. The accelerator allows for tunable positron implantation energies, and the annihilation radiation is detected with Germanium detectors arranged face-to-face and perpendicular to the beam line. [3,4]

The first step to guiding positrons toward the target after they are emitted from the source is positron moderation, which is the conversion of as many high energy positrons as possible into slow positrons with an energy of some eV. Most simple slow positron beams use tungsten in the form of a thin film transmission moderator. The fast positrons are passed through the tungsten

moderator where they undergo thermalization and a small fraction of them reemerge with a kinetic energy equal to the work-function of the moderator material. The moderation efficiency of W is typically only 10^{-3} to 10^{-2} percent. Then, in order to magnetically guide the moderated positrons from the source to the sample, a vacuum system surrounded by Helmholtz coils and solenoids provides the magnetic field for the positron transport as schematically depicted in Figure 4.1 and Figure 4.2. SPONSOR has a distance from source to sample of about 3 m, so it requires a vacuum which ensures a mean free path for the positrons to reach the target. A rough calculation of the mean free paths depending on the vacuum results in a pressure of at least 1.7 x 10^{-5} Torr necessary for this distance. [2] The validity of this estimation can be proved by a simple measurement of the dependence of the count rate of the positrons, having the lowest energy, on the vacuum pressure. Decreases of the positron count rate start at 2 x 10^{-5} Torr and above. SPONSOR is operated in a vacuum range between 3 x 10-7 Torr and 5 x 10-6 Torr which is proved to be completely sufficient. Four Helmholtz coils and nine solenoids create an axial magnetic field with a magnetic flux density of 10 mT. The solenoids are polyethylene cored and wound with insulated copper wire of 2 mm in diameter. [2] The same magnetic wire was used for the Helmholtz coils. Adequate spacing between coils and the vacuum walls must be maintained in order to prevent electrical breakdowns between the vacuum tubes at high potential and the coils at ground potential. In addition to this distance, it is very important to avoid pointed ends and unrounded edges which bundle the electric flux lines and increase the electrical field and thereby the risk for electrical breakdowns. Furthermore, a valve in front of the sample chamber is advantageous because it makes possible the separation of the vacuum at the source and accelerator part from that of the sample chamber and therewith a faster change of samples without breaking the vacuum of the whole beam line.

Depth-resolved variable energy positron annihilation lifetime spectroscopy (PALS) was also done to assess defects of samples at different conditions. The PALS experiments were performed at the mono-energetic positron spectroscopy (MePS) beamline, which is one of the end stations of the radiation source ELBE (Electron Linac for beams with high Brilliance and low Emittance) at HZDR (Germany) shown in Figure 4.2 [3, 4]. PALS measurements require a pulsed beam, so the moderated DC beam was compressed into short bunches using electromagnetic fields. The basic components of a pulsed positron beam system consist of a reflection type chopper, a sub-harmonic pre-buncher and a double harmonic buncher. [5] A periodic acceleration and deceleration of the positrons lead to overall compression in time at a certain focal point. The arrival time of the positron bunch at the target is then provided by the bunching electronics.

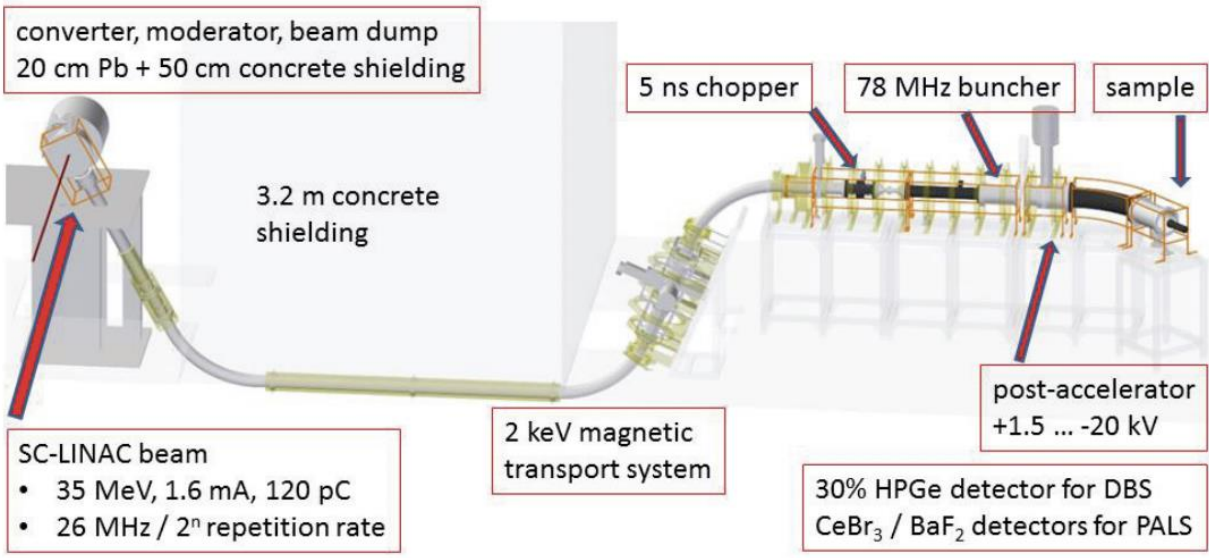

Figure 4.2: A schematic of the Monoenergetic Positron Source at ELBE where the PALS measurements were conducted. [3] The incident electron beam is delivered by the superconducting electron linear accelerator (SC-LINAC). Electron bremsstrahlung radiation with a continuous spectrum up to the electron beam energy is then converted by pair production into electrons and positrons inside the converter and inside the following tungsten moderator. The positrons are then guided toward the sample, and annihilation radiation is detected by the HPGe, $CeBr_3$, and BaF_2 detectors. Note the energy resolution of the HPGe detector at 511 keV was 1.09 ± 0.01 keV.

For the PALS measurements of the annihilation γ rays, $CeBr_3$ scintillator detector coupled to a Hamamatsu R13089 PMT was utilized for the gamma quanta acquisition and the signals were processed by SPDevices ADQ14DC-2X digitizer [6]. The time resolution function was about 0.230 ns. The resolution function required for spectrum analysis includes two Gaussian functions with distinct intensities and relative shifts, which both depend on the positron implantation energy, E_p. All spectra contained at least 10^7 counts. A typical lifetime spectrum N(t) is described by Equation 2.4 [7]. Spectra were deconvoluted into a few discrete lifetime components using the PALSfit software [8].

4.1.1 Sources of Uncertainty in PAS measurements

The major source of error in the PAS measurements is the statistical uncertainty from the fitting software, such as PALSfit [8], used to extract figures of merit from the PAS spectra. Thermalized positrons have very small momentum compared to the electrons upon annihilation, a broadening of the 511 keV line is observed mostly due to momentum of the electrons, which was measured with one or two high-purity Ge detectors (energy resolution of 1.09 ± 0.01 keV at 511 keV). For demonstration, peak broadening in PAS raw data is presented in Figure 4.3. The figure shows an example Doppler broadening spectra for pure chromium versus chromium oxide (air oxidized for 5 days) measured by 5 keV positrons (after background subtraction). Oxide layers are expected

to have higher overall defects than the pure metal, which is confirmed by the increased broadening of the 511 keV peak in the relatively high-defect chromium oxide versus pure chromium. These spectra are the basis for DBS analysis and the extraction of the S-parameter for measuring overall defect concentration, which will be discussed in subsequent sections.

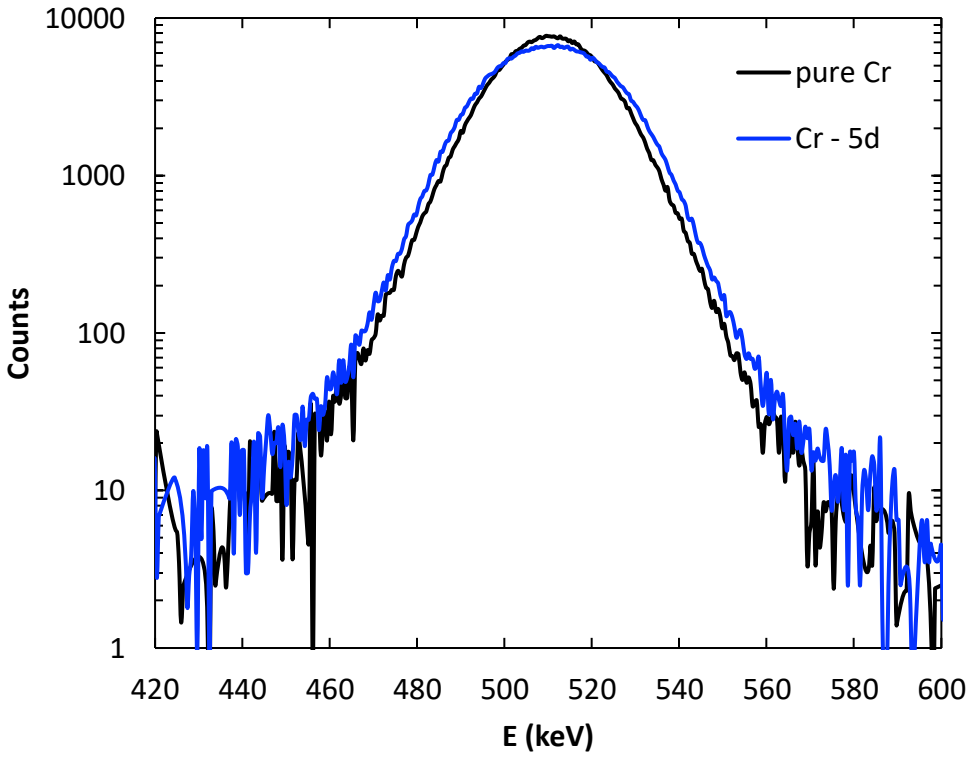

Figure 4.3: Doppler broadening spectra for pure chromium versus chromium oxide after background subtraction. The increased broadening of the 511 keV peak is evident in the relatively high-defect chromium oxide versus pure chromium, which is also reflected after DBS analysis in the S-parameter (to be discussed in subsequent section). Note that the chromium oxide was oxidized in air for 5 days and the incident energy of the positrons was 5 keV.

For PALS, spectra distortions from background artifacts can be introduced from reflected positrons or distortions from the incoming positrons such as out of phase bunching of positrons or inefficiently chopped positrons. However, these background artifacts can be accounted for the PALS analysis in PALSfit [8] by fitting one additional lifetime component of negligible intensity. For demonstration, two comparison PAS lifetime spectra are presented in Figure 4.4 for lifetime spectra (after background subtraction) for pure chromium versus air-oxidized chromium for 5 days. The time on the x-axis is time after the 5 keV implanted positron bunch, or the “start signal”. Each lifetime spectrum has a different slope because of the different defect lifetimes and intensities within the spectrum. After fitting the lifetime spectrum can be fit according to Equation 2.11, the fitted spectrum can be expressed as lifetime components and their intensities. Further analysis of these samples and their component lifetimes will be discussed in a subsequent section. However, in both DBS and PALS, the main source of error in PAS is statistical error during

fitting. For this thesis, all spectra contained at least 10^7 counts, which kept the statistical fitting errors less than 0.2% of the reported fit values for DBS and PALS results. Because the spectra contain a high number of counts, error bars are smaller than the size of the symbols used for data points in results in Chapters 4 and 5, so error bars reside within the respective symbols.

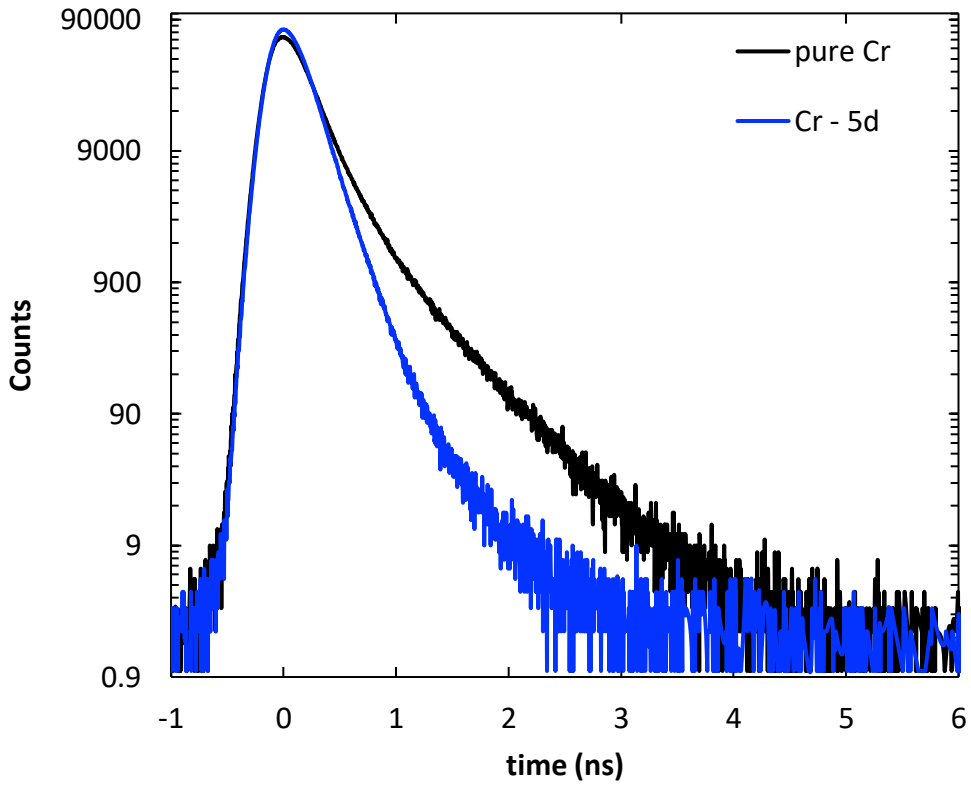

Figure 4.4: Lifetime spectra for pure chromium versus chromium oxide after background subtraction. The time on the x-axis is time after the positron bunch, or the "start signal". The different slopes of the lifetime spectra are evident between the chromium oxide versus pure chromium. These spectra used during PALS analysis to calculate the fitted lifetime components and their intensities (to be discussed in subsequent section). Note that the chromium oxide was oxidized in air for 5 days and the incident energy of the positrons was 5 keV.

Other than fitting uncertainties, detector resolution can be another major source of error. Especially for Doppler broadening data acquisition, the detector energy resolution around 511 keV should be as high as possible and constant across results. The energy resolution will strongly influence the resulting spectra, as lower resolution detectors will obscure peak broadening effects. For results in this thesis, the HPGe detector energy resolution was 1.09 ± 0.01 keV at 511 keV. For PALS, the timing resolution of the detector is also of importance because lifetime spectra are the combination of the detector resolution function and decaying lifetimes. The timing resolution of the detector setup is already included as the resolution function, which again is a sum of two Gaussian functions representing the beginning of the spectrum [6].

4.2 Studying defects in Cr-oxide using PAS

4.2.1 Introduction to importance of defects in Cr-oxides

Oxidation and corrosion of metals and alloys has been studied for decades because of their technological importance. Oxidation can occur at different temperatures, altering point defect types and concentrations, which play an important role in corrosion. Chromium, specifically, has been widely studied and implemented because the passivating chromium oxide film formed during oxidation can be highly corrosion resistant [9-12]. Unalloyed chromium is not used as a construction material by itself, but in many cases the primary reason for adding chromium to alloys is precisely the development of a corrosion resistant oxide layer. When a sufficient concentration of Cr is added to iron, nickel, or cobalt based alloys, Cr_2O_3 is formed in a continuous layer on the surface and ion transport is reduced to the point where corrosion of the underlying metal is substantially suppressed. Ion mobility is slower than in Fe_2O_3 [13, 14]. Point defects play an important role in regulating the effectiveness and establishing the limits of Cr_2O_3 corrosion protection, so significant theoretical, experimental, and modelling efforts have been undertaken to understand the nature of point defects that control oxidation and their diffusion mechanisms. [EXC15-31] Several theoretical efforts have focused on growth kinetics of the oxide layer. [15-17] There is still a large discrepancy in the reported self-diffusion coefficients and defect formation energies from various experimental studies. [17-25] In recent years, some modelling efforts have focused on self-diffusion coefficients in pure Cr, Cr_2O_3, and Cr-containing alloys using density functional theory. [28-31] While each of these approaches provides its own insights on the nature of point defects' charge state, mobility, and formation energies, PAS can probe smaller point defects and their agglomerations.

Previous positron studies investigated the relative defect content of corroded iron alloys containing chromium [32-35] using DBS, however the PALS technique can also provide a quantitative assessment of the defect type and size.

4.2.2 Methods and sample preparation used to study defects in Cr-oxide using PAS.

Polished Cr samples (1200 grit) were oxidized in air at 700°C for 24 hours (24 h) and 5 days (5 d) using a box furnace. The samples were sent to the Institute of Radiation Physics at Helmholtz-Zentrum Dresden – Rossendorf (HZDR) for positron annihilation spectroscopy (PAS) to characterize the defect type and density at different depths for the grown oxide layers. Details on the PAS data acquisition are given in Section 4.1. For lifetime measurements, PALS spectra were then deconvoluted into a few discrete lifetime components using the PALSfit software [8], which directly show evidence of different defect types (sizes) and their corresponding relative intensities, quantifying the overall concentration of each defect type.

4.2.3 Results of PAS study on Cr-oxide defects

Figure 4.5 shows the results from the DBS experiment on the as-polished, annealed for 24 h and 5 days samples, as well as an ultra-high vacuum (UHV) annealed Cr-reference. DBS results are often presented in terms of S-parameter versus energy (E_p), where S is defined as the fraction of positron annihilation with free and valence electrons. Decreases in the S-parameter correspond to reductions in the overall defect density in the material. The positron implantation depth is estimated according to a Makhovian implantation profile [36]. To obtain more quantitative information about defect densities across sample thickness and approximate thicknesses of the oxide layers, the VEPFit code [37, 38] has been utilized. The code numerically solves the positron diffusion equation and provides characteristic parameters i.e., positron diffusion lengths and ranges of individual layers in multi-layer systems. It allows for fits of $S(E_p)$ curves for multilayered systems and provides thicknesses and effective positron diffusion lengths L_+ (a parameter inversely proportional to defect concentration) for each layer within a stack. The calculated L_+ and corresponding defected layer thicknesses are presented in Table 1.

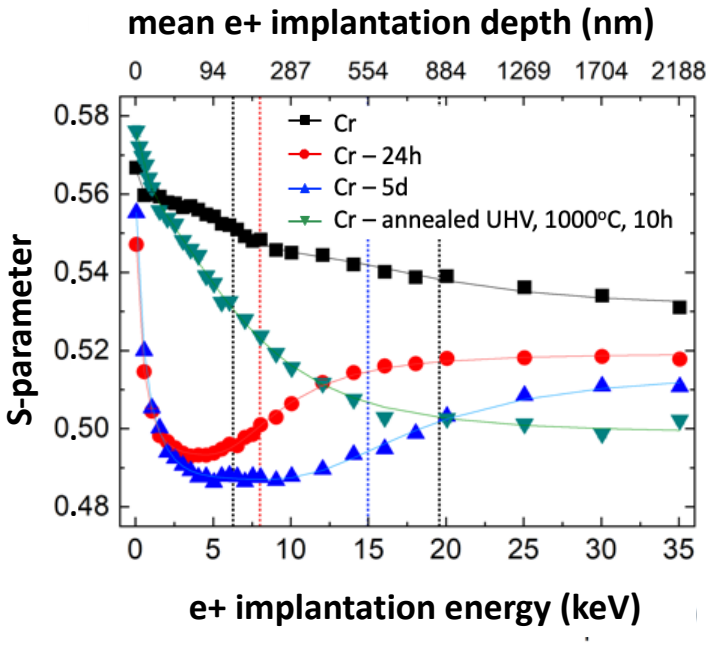

Figure 4.5: S-parameter for a reference UHV 1000 °C, 10 h annealed Cr, as-polished Cr, and Cr oxides annealed to both 24 h and 5 d from DBS. The curves are fitted using the VEPfit code [37,38] and vertical lines represent interfaces between specific regions of different open volume (Cr - polished sample) or between the oxide and Cr (oxidized samples).

Sample name	**d_1 (nm) [oxide]**	**$L_{+,1}$ (nm) [oxide]**	**$L_{+,2}$ (nm) [substrate]**
Cr – 24h	205±80	8±4	44
Cr – 5d	576±281	13±4	119
Cr-UHV-annealed	-	-	131±11

Table 4.1. Calculated using VEPFit code thickness, and effective diffusion lengths, L_+, for the oxidized and a reference sample

PALS measurements evaluate defect microstructure in the oxide layers and further characterize the decrease of defect concentration as a function of annealing time in Figure 4.6. The 5 day oxidation decreased the average defect size (τ_{av}) and defect density compared to the 24 h sample, in agreement with DBS (Figure 4.5). In addition, the slow decay of the average lifetime as a function of E_p in the first 50 nm confirms the persistent surface effects observed in the S-parameter, especially for the as-polished Cr sample.

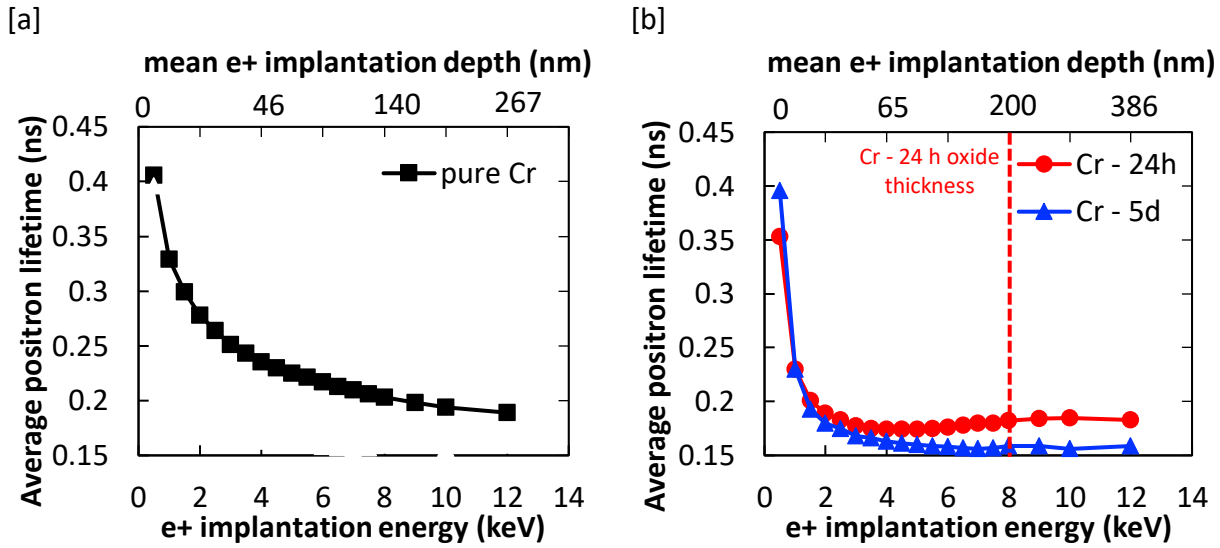

Figure 4.6: Average positron lifetime τ_{av} for as-polished [a] Cr and [b] Cr oxides. The red line indicates the average oxide thickness for the 24 h annealed sample.

Notably, the largest achievable E_p = 12 keV during PALS did not allow positrons to probe as deep as DBS. Thus, in the 24 h sample, only the deepest implanted positrons at E_p > 8 keV are sampling the bulk Cr metal, resulting in the average lifetime converging toward the as-polished Cr sample. The average oxide layer thickness is marked in Figure 4.6 to highlight the expected depth of the 24 h metal-oxide interface. In the case of 5 day Cr oxide, the available positron energy was not enough to implant positrons into Cr-bulk, hence the obtained signal originates purely from the oxide layer.

By fitting the PALS data using the PALSfit code [8], specific lifetimes and their relative intensities were obtained, which represent defect sizes and concentrations within the oxide layers, respectively (Figure 4.7). Larger lifetimes correspond to larger defect complexes, and higher intensities of respective lifetimes reflect higher associated relative defect densities. Two lifetime components were analyzed for each sample, as seen in Figure 4.7 (the third component originating from the surface ortho-positronium was omitted for clarity due to its residual intensity). Thus, the first component corresponds to smaller defects while the second component corresponds to larger vacancy clusters.

[a]

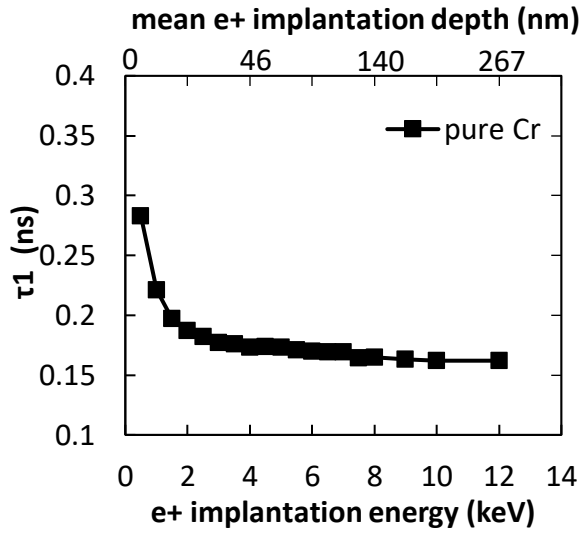
mean e+ implantation depth (nm)
0
46
140
267
pure Cr
τ1 (ns)
e+ implantation energy (keV)

[b]

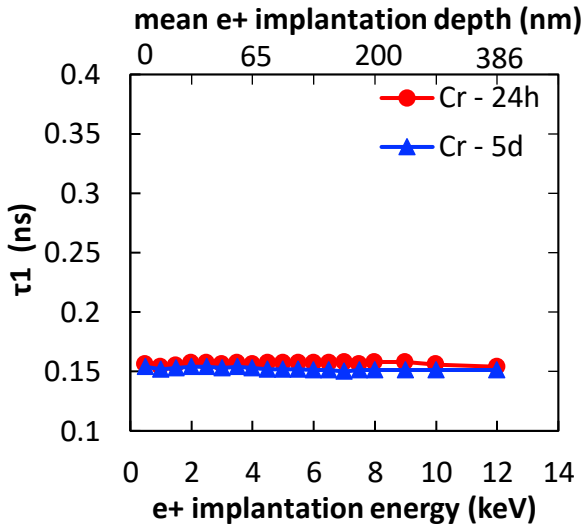
mean e+ implantation depth (nm)
0
65
200
386
Cr - 24h
Cr - 5d
τ1 (ns)
e+ implantation energy (keV)

[c]

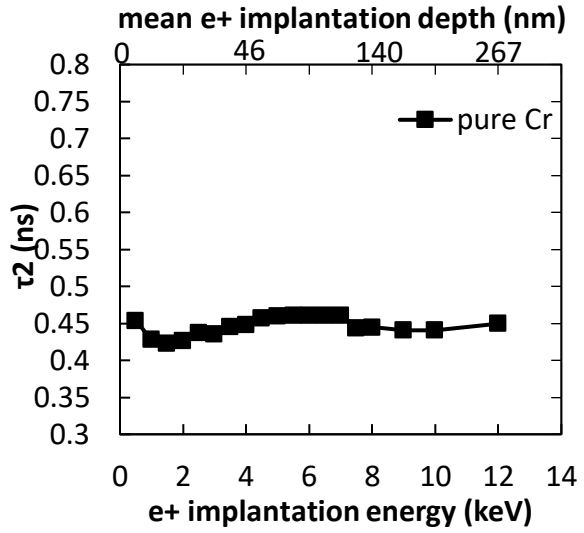
mean e+ implantation depth (nm)
0
46
140
267
pure Cr
τ2 (ns)
e+ implantation energy (keV)

[d]

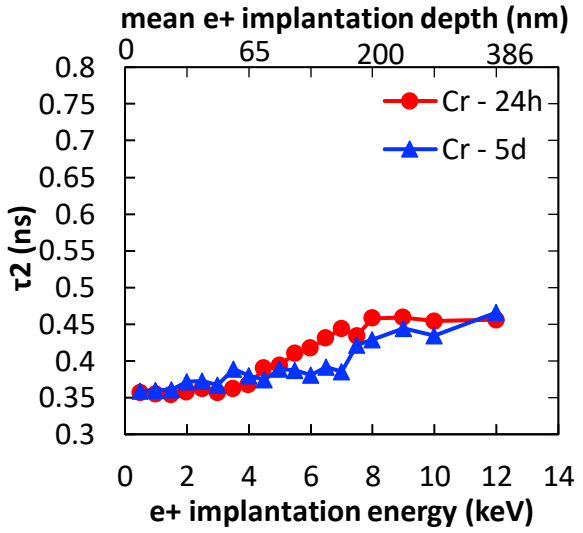
mean e+ implantation depth (nm)
0
65
200
386
Cr - 24h
Cr - 5d
τ2 (ns)
e+ implantation energy (keV)

[e]

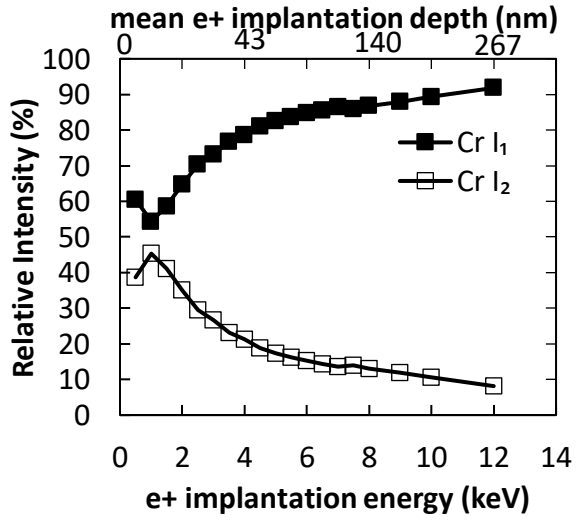
mean e+ implantation depth (nm)
0
43
140
267
Cr I1
Cr I2
Relative Intensity (%)
e+ implantation energy (keV)

[f]

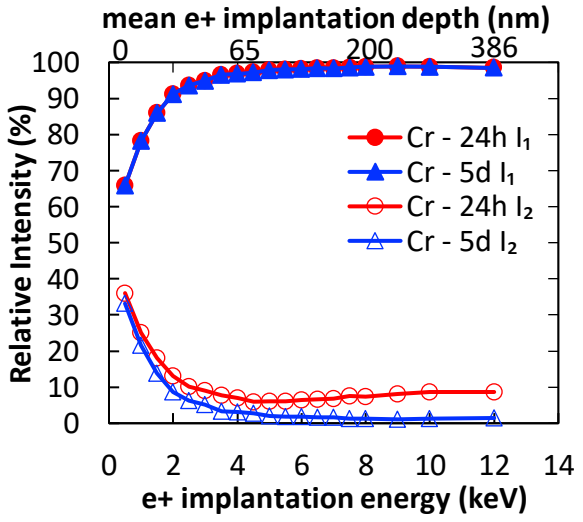
mean e+ implantation depth (nm)
0
65
200
386
Cr - 24h I1
Cr - 5d I1
Cr - 24h I2
Cr - 5d I2
Relative Intensity (%)
e+ implantation energy (keV)

Figure 4.7: Positron lifetime components τ_i (a) and their relative intensities I_i (b) calculated from PALS spectra decomposition for as-polished Cr versus air oxidized Cr.

4.2.4 Discussion on defect concentration in oxidized pure chromium

In the as-polished Cr sample, despite the near surface effect, τ_1 monotonically decreases to about 161 ps throughout the thickness, but it shows no saturation yet. The further decrease in τ_1 is expected for larger E_p as evidenced from $S(E_p)$. The value of the bulk lifetime in Cr metal reported in the literature is 120 ps [39]. The first (161 ps) component is larger than for bulk delocalized annihilation but lower compared to the value of 184 ps for Cr monovacancy [40], suggesting this component is likely associated with positron annihilation at dislocations [41]. Dislocations act as shallow positron traps [42, 43] wherein positrons have a low binding energy (10 to 100 meV) [44]. Consequently, thermal positrons are weakly localized in dislocations, and they get de-trapped and annihilate with lifetimes slightly above the bulk value. τ_1 is likely an average lifetime in the bulk and at dislocations. Positron trapping at dislocations in Cr_2O_3 is probable and has been previously observed [45]. The second lifetime component τ_2 is in the range of 450 ps, indicating the presence of large vacancy clusters of more than 15 vacancies. This measurement confirms an overall high defect level from polishing in addition to the near surface effects such as partial positron annihilation at surface states from back-diffused positrons [8, 46].

Figure 4.8 shows theoretical calculations of positron lifetimes in Cr_2O_3 for the delocalized (bulk lifetime) and localized (positrons trapped at vacancy like defects and their agglomerations) states obtained using the atomic superposition (ATSUP) method within two-component density functional theory (DFT) ab initio calculations [39]. For the electron-positron correlation, the generalized gradient approximation (GGA) scheme was used [40]. The calculations were performed by a collaborator at HZDR in Dresden, Germany.

Annihilation state	**Calculated positron lifetime (ps)**
Bulk	151.7
Chromium vacancy (V_{Cr})	197.4
Oxygen vacancy (V_O)	153.7

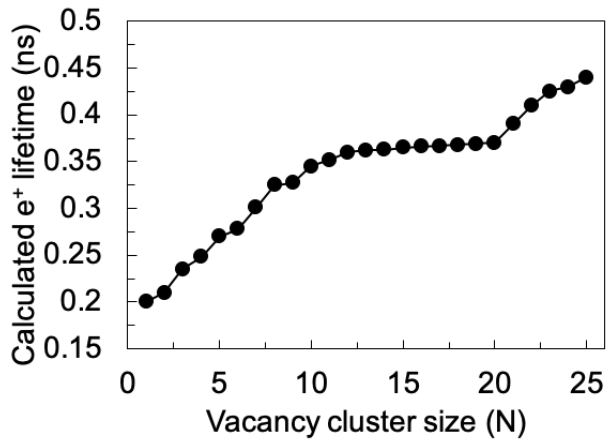

Figure 4.8: ATSUP simulated annihilation states for bulk and monovacancy configurations in Cr_2O_3. Calculated positron lifetime as a function of vacancy cluster size with N agglomerated

vacancies is also plotted. The spherical void was obtained by removing Cr and O atoms around a reference point and sorted by distance.

For the oxide samples, the first lifetime component τ_1 at 151 ps represents the bulk lifetime or positron annihilation at oxygen vacancies (see Figure 4.8 for a reference of low order vacancy defect configurations in Cr_2O_3). It should be noted that oxygen vacancies are typically positively charged, hence repulsing to positrons, however they are positron traps if they become neutral. Considering the low L_+ obtained for oxidized films from the VEPfit S(E_p) analysis, trapping at oxygen vacancies becomes a viable option. Another possibility is shallow trapping at dislocations not associated with vacancies [47]. The second lifetime component, τ_2 varies from 350 to 460 ps throughout the measured thickness of the oxide. This large lifetime indicates the presence of large vacancy clusters with more than 10 to ~25 vacancies (see Figure 4.8). This variance in lifetime values is more obvious in the oxidized samples indicating the increase of the cluster size at higher depths. Lastly, a positron lifetime representing the annihilation of surface positronium τ_3 can be found in the PALS data with an intensity dropping towards zero for larger implantation depths (with decreasing influence of the surface). The fit algorithm usually shows this component even if it has intensities less than 0.5 %. For PALS results, data points with less than 0.5 % intensity are not shown.

Two important trends emerge from the PALS lifetime intensity data after associating τ_1 with positron annihilation in the bulk, oxygen vacancy, or dislocation states, and τ_2 with large vacancy clusters. First, aging the oxide increase the relative intensity I_1 of τ_1 up to ~100% for the 5 days oxidation, compared to about 90% for 24 h. This strongly suggests that nearly all positrons annihilate at either the bulk Cr_2O_3 oxide, oxygen vacancies, or dislocations. Second, aged oxide layers show lower relative defect concentration. Increasing the oxidation time from 24 h to 5 day decreases the relative intensity I_2 of the defect cluster lifetime τ_2. These results confirm the trends from the DBS data, so increasing aging oxide layers results in relatively less overall measured defects within the grown oxide. This suggests that defects anneal with aging.

An important observation is that positron annihilation spectroscopy (DBS and PALS) and electrochemical measurements both consistently showed lower defect densities in 5 days air oxidized chromium than in the 24-hour sample. In other words, both fundamentally different experimental techniques can measure point defects separately with mutually complementary results. For positron annihilation lifetime spectroscopy (PALS), the positron lifetime signal pertaining to large vacancy clusters defects vanished from $I_2 \approx 10\%$ to zero comparing 24 h to 5 days of air oxidation, so no large vacancy clusters are observed in the 5 day sample at the same oxide layer depth. The PALS technique provides information about the size of neutral and negatively charged vacancies, and although larger vacancy clusters were observed in these oxides, the exact charge state cannot be probed. Isolated cation vacancies would be negatively charged and seen by PALS.

Combining the analysis from previous electrochemical studies and PALS reveals insight into the predominant defect species within the oxide. Electrochemical Mott-Schottky analysis [10,11,48-51] indicates the p-type semiconductor character of the chromium thermal oxides. The data suggests that oxygen interstitials and larger chromium vacancy clusters could provide charge carriers in the 24 h oxide. Longer oxidation time (5 days) may anneal larger vacancy-type defects and potentially leave oxygen interstitials as the predominant defect type. This could explain the relative decrease in defect densities after 5 days of air oxidation.

Density functional theory calculations performed by multiple authors [27-31] are divided on whether chromium or oxygen point defects are predominant within the oxide, be it vacancies, interstitials, or even Frenkel defects (composed by an interstitial atom and a vacancy). From the Mott-Schottky analysis, p-type behavior provides evidence that either chromium vacancies or oxygen interstitials are predominant. PALS experiments show no evidence of isolated chromium cation monovacancies in the oxide, even though cation monovacancies are negatively charged and readily observable by positrons, which leaves oxygen interstitials or larger chromium vacancy clusters as the likely predominant point defect types. In the DFT calculated migration energies, oxygen interstitials are also shown to be relatively more stable defects because contrary to the large lattice spacings generated by chromium monovacancies, smaller oxygen interstitials do not generate considerable local structural distortions to the lattice. This results in oxygen interstitials' low migration energy barrier [29], which would be necessary to drive diffusion and migration, especially compared to chromium vacancies' high migration energies [28-31].

However, both electrochemical and positron annihilation-based techniques do not prove the predominance or quantify the absolute population of oxygen interstitials. For reference, the thermal equilibrium concentration of oxygen interstitials in Cr_2O_3 at 700˚C was calculated using the formation enthalpies from DFT simulations [30] resulting in on the order of 10^{13} interstitials per cm^3. Even though 5 days of oxidation may not be enough time for thermal equilibrium conditions, the PALS lifetimes at longer oxidation time should trend toward the thermal equilibrium concentration, indicating that this oxide is significantly closer to equilibrium than the 24 h sample.

Positron annihilation spectroscopy and electrochemistry supports, but does not prove, the primary role of chromium vacancy cluster complexes and/or anion oxygen interstitials in dictating transport in Cr_2O_3 in thermally oxidizing environments. Positron spectroscopy results suggest the presence of larger vacancy cluster complexes within the oxide, which can provide charge carriers. When oxidizing pure chromium, the partial pressure of oxygen (P_{O2}) plays a critical role in dictating the semiconductor properties of Cr_2O_3 during oxidation, in particular, which point defect type dominates the oxidation diffusion process. At low P_{O2} (e.g., air oxidation), the outward transport of Cr interstitials dominates (n-type character) [24, 29, 52, 53]; whereas at high P_{O2}, chromium vacancies dominate (p-type character) [24, 29, 52, 53], but at the metal-oxide interface, relative oxygen mobility is significantly higher than that of Cr [30].

4.2.5 Conclusion

Section 4.2 showcases the capability of PAS in evaluating defects' evolution during growth of Cr oxide layers in a single study. Combining defect analysis from positron annihilation spectroscopy with electrochemical techniques such as Mott-Schottky analysis allows a comprehensive view on the defects in thermally grown oxides. It was found that, while the oxide layer increases in thickness as a function of oxidation time, the defect density is greatly reduced. Further illustration of this defect behavior as a function of oxidation time can be found in the oxidation discussion section in Chapter 6. The most likely predominant defects were identified as oxygen interstitials or chromium vacancy cluster complexes. This confirms the growth process for Cr_2O_3 is dependent on the transport of oxygen interstitials and chromium vacancy clusters while adding quantitative data to the process.

4.3 Studying defects in Fe-oxide using PAS

4.3.1 Introduction to importance of defects in Fe-oxides

Fe-based alloys are widely used in the nuclear industry as structural materials like steel due to their excellent high-temperature mechanical properties, corrosion resistance, and resilience to radiation [54-56]. Reactor environments expose these materials to a complex array of environmental variables such as radiation and corrosive impurities, which can work in concert to significantly reduce their service life [57].

Fe-based alloys react with oxygen or water vapor at high temperature to form an oxide film covering the metal surface, and this oxide layer functions as a barrier and separates the alloys from the corrosive medium to protect materials from corrosion [58, 59]. For example, when austenitic stainless steels are exposed to a primary nuclear water coolant environment, a passive film composed of an inner $FeCr_2O_4$ and an outer Fe_3O_4 formed on the surface of steel which protects it from corrosion [59-63]. The technological importance of these protective oxide films led to widespread investigation of their microstructures and conductivity [58-65]. Previous studies show that the predominant iron oxide grown at 600^{o}C is p-type semiconductor, but the oxides grown at 400 ^{o}C and 800 ^{o}C are n-type [66]. Increasing the oxidation time at a constant temperature can also improve the corrosion resistance of the oxide scale in corrosive media such as liquid lead-bismuth eutectic (LBE) [64]. It was found that not only the basic structure is important to passivity, the defects inside the oxide films also play a critical role for its protective properties [67, 68].

In addition, neutrons inside nuclear reactors are responsible for inducing displacement damage, point defects, microstructural changes in materials [69]. Microstructure changes include void formation and dislocation loops in ferritic/martensitic (F/M) steel [70]. Frazer et al. [70] studied the proton irradiation/corrosion coupling effects on the corrosion behavior of HT-9 F/M steel in static liquid LBE with 2×10^{-6} wt.% O_2 at 420-450 ^{o}C and found that irradiation enhanced the oxidation of materials. Deng et al. [71] studied the effect of irradiation on corrosion of 304SS in a primary nuclear water coolant environment and found similarly that irradiation enhanced the oxidation of materials. However, Jiao and Was [65] found that in 316SS in a simulated boiling

water reactor environment with a different oxide, α-Fe_2O_3, proton irradiation did not greatly enhance oxidation, but still found a large oxidation dependence on grain orientation. Therefore, irradiation can induce microstructure and compositional modification and alters defect densities in materials, so it must also affect the passive behavior of oxides formed on the surface of alloys [72]. It is of particular concern to determine which of the charge carriers within the semiconductor oxide serves as the predominant charge carrier. Previous studies thus far have focused on the effect of irradiation on p-type semiconductors generally [73, 74], but not on the oxides themselves.

This section investigates the effect of irradiation on structure and defects in iron oxide scales and subsequent corrosion behavior, which is an important step in determining the corrosion behavior of Fe-based alloys under nuclear extremes. The results and discussion will be split into different sections – first the 400^{o}C and 800^{o}C samples to investigate the effect of oxidation temperature on irradiation point defects, and then the 600^{o}C samples to investigate the effect of oxidation time on irradiation point defects.

4.3.2 Methods and sample preparation used to study defects in iron oxide using PAS

Polishing and Oxidation

Fe coupons (99.999%, Alfa Aesar) were metallographically polished to 1200 grit surface finish, then oxidized in air at different oxidation times and temperature conditions. The 400°C and 800°C samples were oxidized for 1 hour. The 600°C sample series was created for oxidation times at 1 hour, 4 hours, 9 hours, and 16 hours. Two samples were fabricated for each oxidation condition. One sample from each condition was subjected to proton irradiation. It is important to note that the various characterization techniques were performed on the exact same material (sample).

Herein, the nomenclature of thermally oxidized Fe is abbreviated as TF; the temperature of the air oxidation is added to the end of the abbreviation (i.e., TF400); the thermally oxidized, proton irradiated Fe is abbreviated as IF. The temperature notation is identical to its as-oxidized pre-irradiated baseline. The first set of oxidation temperature samples are thus TF400, IF400, TF800, IF800. The second set of oxidation time samples at 600^{o}C are: TF600, 1hr; TF600, 4hr; TF600, 9hr; TF600, 16hr; IF600, 1hr; IF600, 4hr; IF600, 9hr; and IF600, 16hr.

Prior work by Qiu et al. has investigated the electrical and structural properties of the identical unirradiated TF400, TF800, and TF600, 1hr subjected to liquid lead-bismuth eutectic (LBE) [64]. Figure 4.9 features cross-sectional SEM images of these oxides for reference [64]. To avoid the presentation of duplicate results, some structural properties such as oxide thickness and phase composition will be reference from [64]. Table EXF1 shows the oxide structure and thickness of TF400 and TF800. The approximate relatively oxide thickness of TF800 was calculated using the ratio 95:4:1 for iron oxidized at 1000° [75]:

	TF400	TF800
Composition	α-Fe_2O_3/Fe_3O_4/Fe	α-Fe_2O_3/FeO/Fe_3O_4/Fe
Oxide thickness (μm)	0.7	85.9
Relative oxide thickness (μm)	-	0.86/3.4/81.6
Note	A thin (~10 nm) top layer of α-Fe_2O_3 is present.	-

Table 4.1: Oxide thickness and phase composition of TF400 and TF800 samples oxidized in air from Qiu et al. [64]

	TF600, 1hr	TF600, 4hr	TF600, 9hr	TF600, 16hr
Composition	FeO/Fe_3O_4	FeO/Fe_3O_4	FeO/Fe_3O_4	FeO/Fe_3O_4
Oxide thickness (μm)	8	15	20	26
Oxidation Time	1 hour	4 hours	9 hours	16 hours

Table 4.2: Oxide thickness and phase composition of TF600 series samples oxidized at 600°C in air for different times [64]

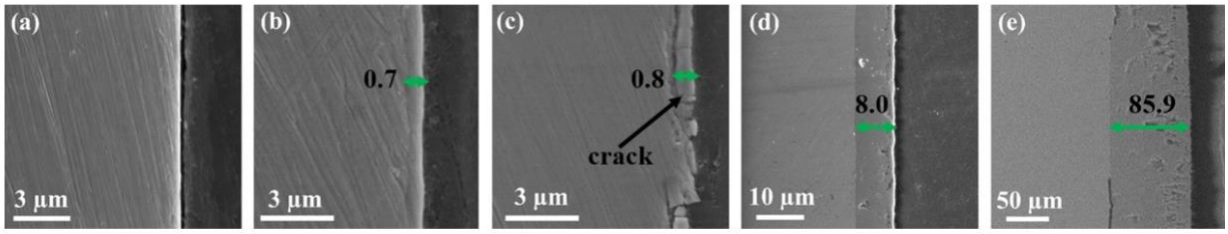

Figure 4.9: Cross-sectional SEM images of iron-oxidized at (a) 200 (b) 400°C (c) 400°C (d) 600°C (3) 800°C for 1hr [64]

A set of samples was then irradiated with 200 keV protons up to a fluence of $6.02*10^{16}$ ion/cm^2 on the 200 kV Danfysik ion implanter at the Ion Beam Materials Laboratory (IBML) at Los Alamos National Laboratory. The sample stage was actively air-cooled to keep the samples near room temperature and below ~35°C during the approximately 23-hour-long irradiation. The corresponding damage profile was calculated using the Stopping and Range of Ions in Matter [76] software for each sample. In the SRIM calculation, a displacement threshold energy of 28 eV for oxygen atoms versus 40 eV for Fe atoms was assumed, and the quick K-P cascade mode was used. Both the irradiation and the SRIM calculation were performed at an angle of 5 degrees. The damage profiles are plotted in the following subsection.

Lastly, all samples were sent to the Institute of Radiation Physics at Helmholtz-Zentrum Dresden – Rossendorf (HZDR) for positron annihilation spectroscopy (PAS) to characterize the defect type and density at different depths for the grown oxide layers. Details on the PAS data acquisition are given in Section 4.1. For lifetime measurements, PALS spectra were then deconvoluted into a few discrete lifetime components using the PALSfit software [8], which directly show evidence of different defect types (sizes) and their corresponding relative intensities, quantifying the overall concentration of each defect type.

4.3.3 Results of PAS study oxidation temperature effects on Fe-oxide defects

Figure 4.10 shows the damage profile due to proton irradiation calculated in SRIM for both (a) IF400 and (b) IF800 samples [76]. The dpa profile and proportion of the dpa that is due to O vacancies are plotted on the left axis. On the right axis, the final proton distribution is shown. The oxide interfaces are shown by the vertical dotted line. Dpa and ion distribution results are based on a SRIM monolayer calculation, while the oxygen vacancy values are based on a full cascade calculation.

The damage profile for both materials is relatively flat up to a peak at about 0.03 dpa at a depth of 0.81µm [76]. In IF400, the 0.7-micron Fe_3O_4 oxide is primarily irradiated before the underlying metal substrate, and 10 nm-scale α-Fe_2O_3 top layer is included. Whereas for IF800, the relatively flat region of the dpa profiles is primarily in the 0.86-micron α-Fe_2O_3 top layer. However, the peak damage is in deeper into the α-Fe_2O_3 layer to a peak dpa of 0.3.

As shown in Figure 4.10a, the peak of the ion distribution is expected to be deeper in the material than the dpa peak. In Figure 4.10b, this difference is much smaller due to the presence of O and its lower displacement energy (28 eV vs. 40 eV for Fe, based on Konobeyev et al. [77]) The dpa peak in Figure 4.10a is shallower than in Figure 4.10b because of the higher density of the second layer and the consequently slightly faster energy loss of the protons.

[a]

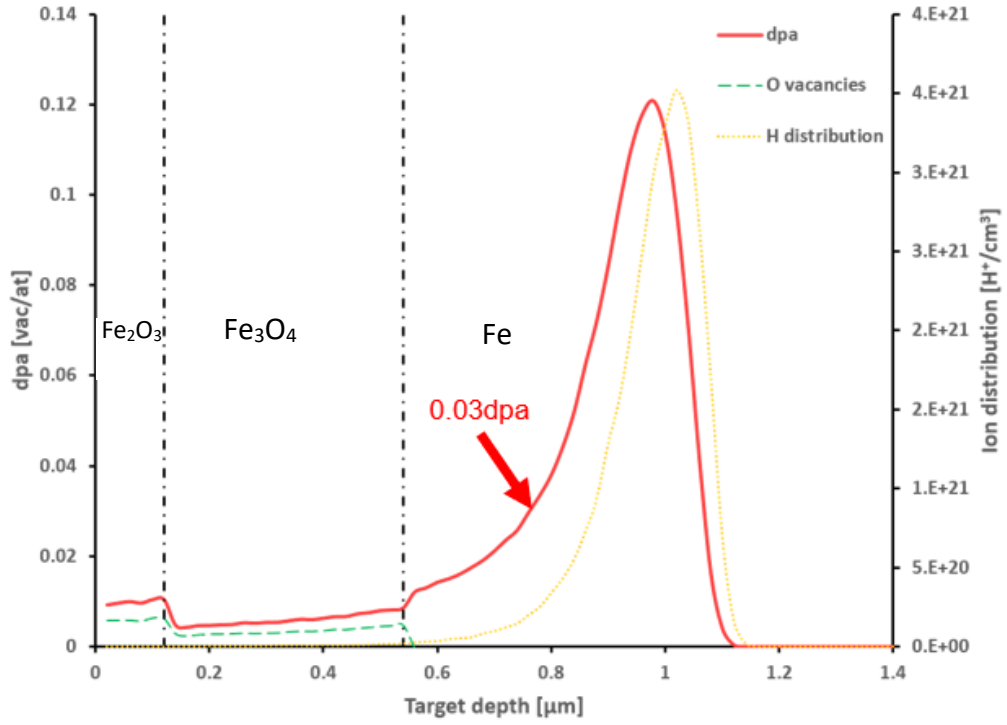
dpa
O vacancies
H distribution
Fe2O3
Fe3O4
Fe
0.03dpa
dpa [vac/at]
Ion distribution [H+/cm3]
Target depth [μm]

[b]

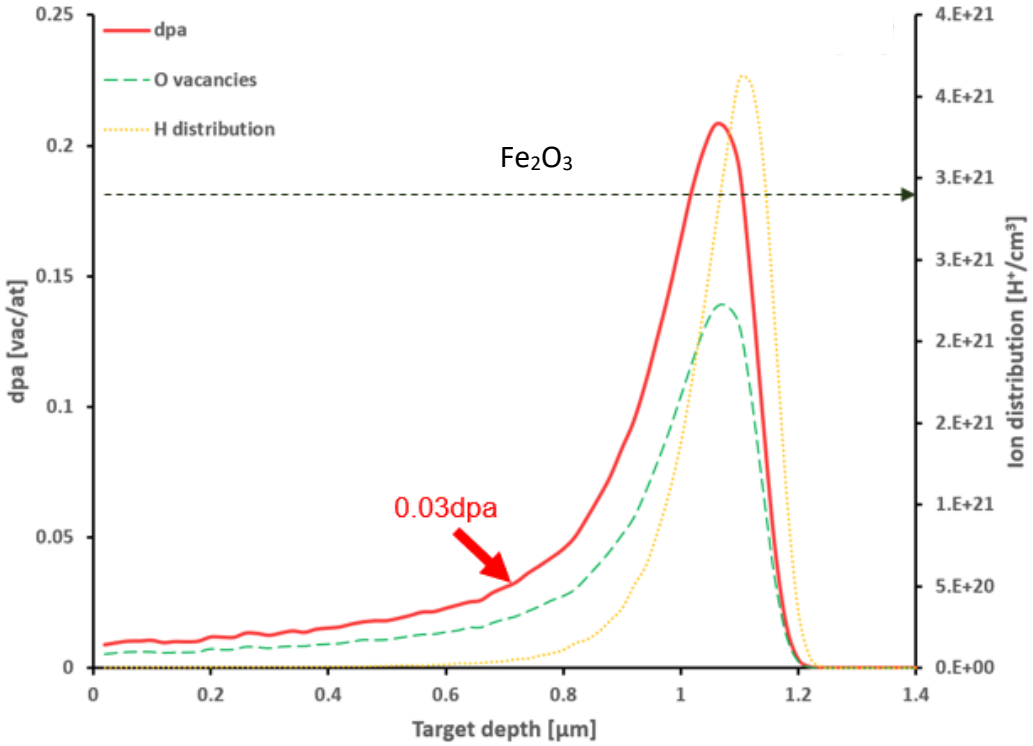
dpa
O vacancies
H distribution
Fe2O3
0.03dpa
dpa [vac/at]
Ion distribution [H+/cm3]
Target depth [μm]

Figure 4.10: Damage profile of proton irradiation calculated by SRIM for the (a) IF400 and (b) IF800 samples. The red arrow indicates the irradiation depth corresponds to 0.03 dpa with 200 keV protons. The total dpa, O-vacancies, and hydrogen distribution results are obtained based on a full cascade calculation mode, where threshold displacement energies of 40 eV for Fe and 28 eV for O are used.

Figure 4.11 shows the results from the DBS investigation of the TF400/IF400 and TF800/IF800 oxides. At positron implantation energies greater than 10 keV, the IF400 and IF800 oxides show an increase in S-parameter after radiation damage, compared to TF400 and TF800, respectively, indicating higher vacancy defect concentrations on average after proton irradiation. In the oxidized samples, the large decreases in the S-parameter in the first 50 nm are due to partial positron annihilation at surface states from back-diffused positrons. Positrons after implantation diffuse in any direction through the crystal, however, at low implantation energies, they can back diffuse to the surface and are trapped in the surface pseudo potential, where they annihilate after longer lifetimes on average compared to bulk or localized annihilation. This increases the S-parameter which accordingly scales with the positron lifetime.

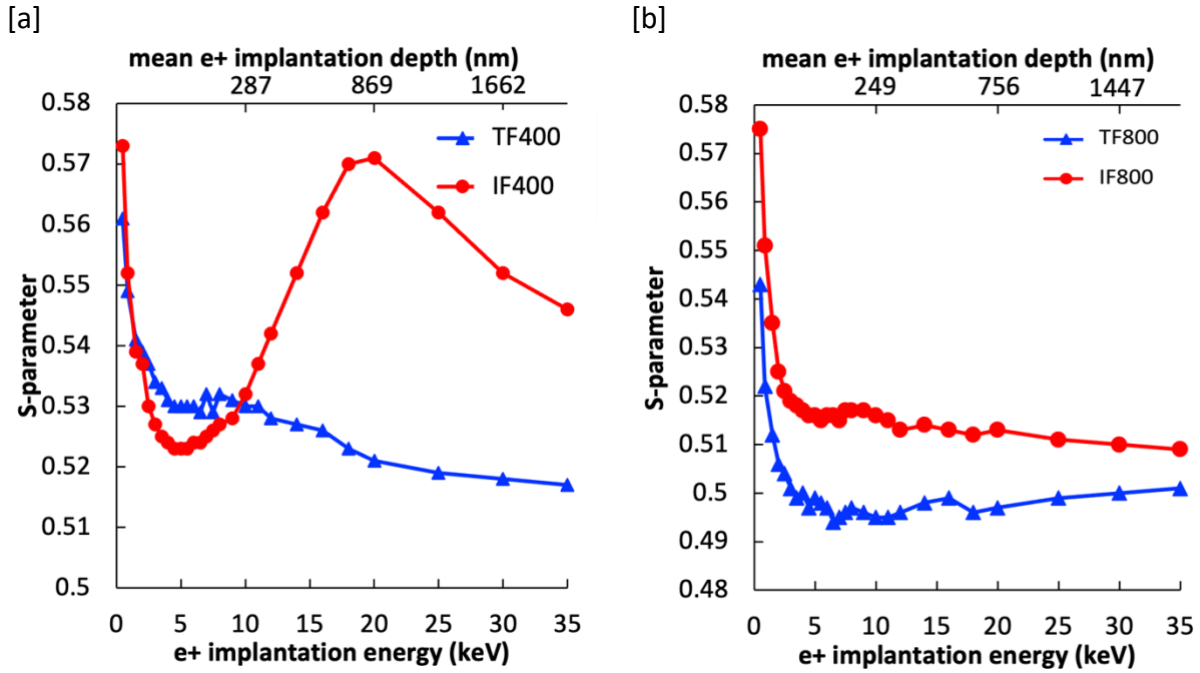

Figure 4.11: S-parameter for pre-irradiation and post-irradiation pure Fe oxidized in air at (a) 400°C, 1hr and (b) 800°C, 1hr from DBS.

From Figure 4.11b, the IF800 oxide shows a consistently larger S-parameter than that of TF800, indicating that proton irradiation results in a higher concentration of vacancy defects. Note that the S-parameter at each implantation energy is an average over a region that is spread out due to positron implantation/diffusion and does not correspond to a precise depth in the sample.

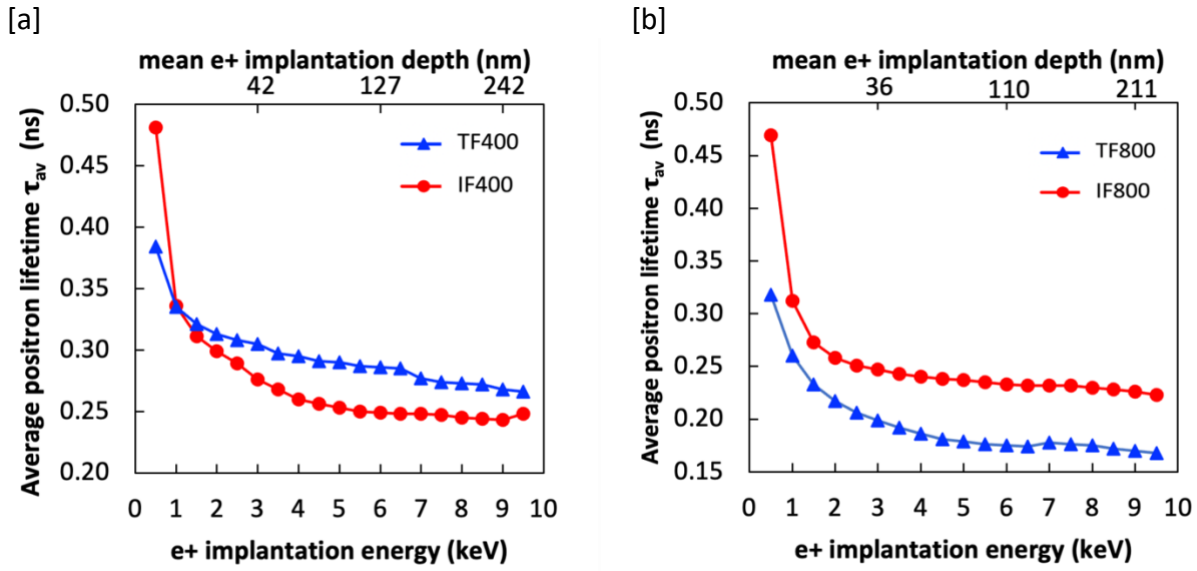

Figure 4.12: Average positron lifetime (τ_{av}) for pre-irradiation and post-irradiation pure Fe oxidized in air at (a) 400°C, 1hr and (b) 800°C, 1hr from PALS.

To evaluate vacancy defect microstructure in the oxide layers and further characterize the decrease of defect concentration as a function of annealing time, PALS results on the samples are presented in Figure 4.12 and Figure 4.13. From Figure 4.12a, the 400°C samples showed a decrease in the average defect size (τ_{av}) after irradiation (IF400) compared to the as-oxidized case (TF400). For the 800°C samples, the average defect size (τ_{av}) decreased after irradiation (IF800) compared to the as-oxidized case (TF800), as seen in Figure 4.12b. These findings agree with DBS results, as the S-parameter trends share the same overall behavior in the 0 – 10 keV region.

By fitting the PALS data using the PALSfit code [8], specific lifetimes and their relative intensities were obtained, which represent defect sizes and relative concentrations within the oxide layers, respectively (Figure 4.13). Larger lifetimes correspond to larger defect complexes, and higher intensities of respective lifetimes reflect higher associated relative defect densities. Two lifetime components were analyzed for each sample, as seen in Figure 4.13 (the third component originating from the surface ortho-positronium was omitted for clarity due to its residual intensity).

[a]

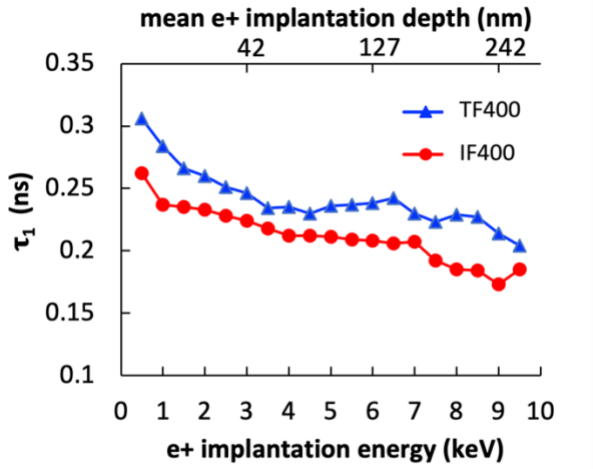
mean e+ implantation depth (nm)
42
127
242
TF400
IF400
τ1 (ns)
e+ implantation energy (keV)

[b]

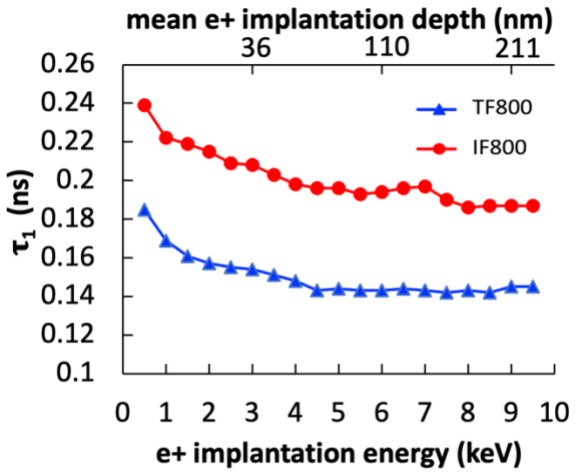
mean e+ implantation depth (nm)
36
110
211
TF800
IF800
τ1 (ns)
e+ implantation energy (keV)

[c]

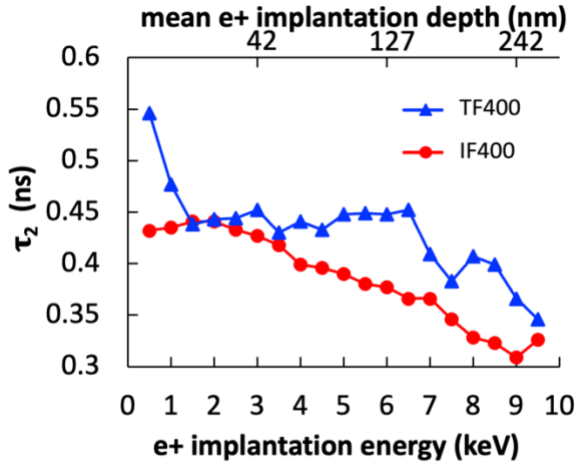
mean e+ implantation depth (nm)
42
127
242
TF400
IF400
τ2 (ns)
e+ implantation energy (keV)

[d]

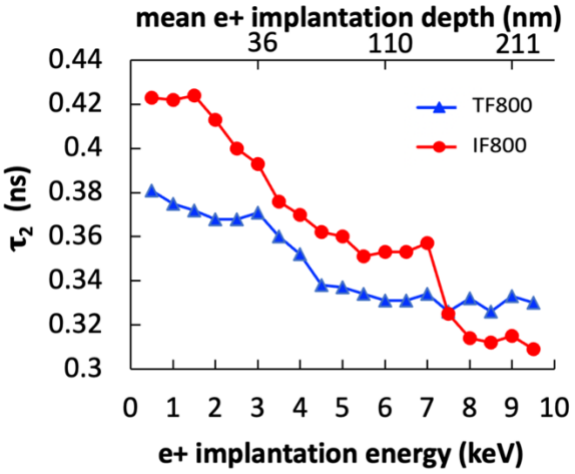
mean e+ implantation depth (nm)
36
110
211
TF800
IF800
τ2 (ns)
e+ implantation energy (keV)

[e]

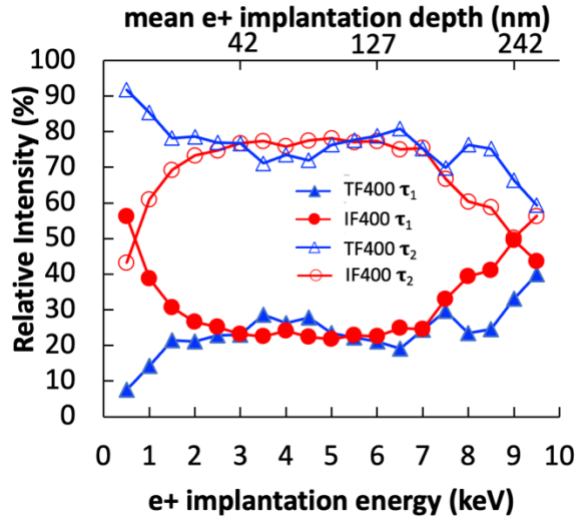
mean e+ implantation depth (nm)
42
127
242
TF400 τ1
IF400 τ1
TF400 τ2
IF400 τ2
Relative Intensity (%)
e+ implantation energy (keV)

[f]

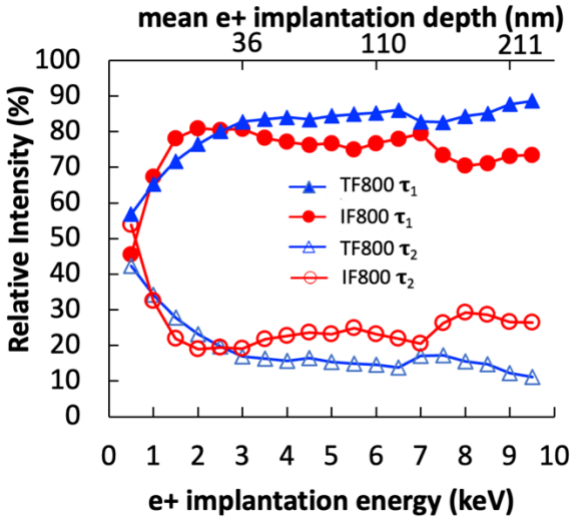
mean e+ implantation depth (nm)
36
110
211
TF800 τ1
IF800 τ1
TF800 τ2
IF800 τ2
Relative Intensity (%)
e+ implantation energy (keV)

Figure 4.13: Positron lifetime components τ_i (a,b,c,d) and their relative intensities I_i (e,f) calculated from PALS spectra decomposition for pre-and post-irradiation pure Fe oxidized in air at 400°C, 1hr (a,c,e) and 800°C, 1hr (b,d,f).

The 400°C samples showed a decrease in both τ_1 and τ_2 lifetime components after irradiation (IF400) compared to the as-oxidized case (TF400), indicating decreasing defect size for both components (Figure 4.13a,c). The 800°C samples generally showed an increase in both τ_1 and τ_2 lifetime components after irradiation (IF800) compared to the as-oxidized case (TF800), indicating increasing defect size (Figure 4.13b,d). Interestingly, the relative intensities of the defects sampled in the 400°C and the 800°C samples did not change much before and after irradiation (Figure 4.13e,f). With more information about the stoichiometry of the oxide layers from TEM, one could start to interpret the different defect states that might have been sampled by the positrons. It is noted that the largest achievable E_p = 12 keV during PALS did not allow positrons to probe as deep as DBS.

4.3.4 Discussion of PAS study oxidation temperature effects on Fe-oxide defects

Because the oxides studied in this work are multi-layered in nature, one needs to compare the S-parameter to the positron implantation depth relative to the oxide structure to have a reasonable understanding of vacancy defect distribution. For the DBS result shown in Figure 4.11a for the TF400/IF400 samples, the positron signals from the first 50 nm may be dominated by surface effects and back-diffusion. A pronounced increase in S-parameter was observed for the implantation energy range between 15 and 25 keV, which corresponds to a depth from ~500 nm to ~1200 nm, a range of thickness that covers the Fe_3O_4/Fe metal-oxide interface. Thus, it is very likely that vacancies may accumulate at metal/oxide interface, but this requires further corroboration by other techniques, such as Transmission Electron Microscopy (TEM). Therefore, because of increase in the average S-parameter (i.e., vacancy defect concentration) before the metal/oxide interface for IF400 after irradiation, suggests oxide vacancy content increases. The saturation of point defects at the metal/oxide interface could also be a reason for the increase in S-parameter, which has recently been observed by Owusu-Mensah et al [78].

To fully understand the change in the defect structures after irradiation, the lifetime components in the two films before and after irradiation must also be examined further. Lifetime data (Figure 4.13) indicate the presence of small and large vacancy clusters in the TF400 oxide while the TF800 contain much lower level of vacancies with smaller average size. The lifetime components in TF800 indicate the presence of dislocations and small percentage of cation vacancy related defects [79]. The increase in the first lifetime component, τ_1, after irradiation is due to the formation of small vacancy clusters of 2-3 vacancies, while the behavior of the second lifetime component τ_2 in IF800 indicates the evolution of large vacancy clusters that are not homogenous in size across the oxide layer thickness. In IF400, it is interesting to observe a significant decrease in τ_1 and τ_2 after irradiation signaling a decrease in the size of the cation vacancy related defects, which may be due to filling some of these vacancies with H^+ after its diffusion to the surface and these layers. Previous PAS measurements showed the effectiveness of H in filling and passivation of cation vacancies and cation vacancy complexes [80, 81]. It is important to mention that

positron cannot directly probe isolated oxygen vacancies because of their positive charge which prevent positron trapping.

The PALS measurement showed a reduction of vacancy size based on a comparison of τ_1 and τ_2 lifetimes after proton irradiation; in other words, vacancy cluster formation was not favored. For magnetite (Fe_3O_4), the migration energies of Fe vacancy and oxygen vacancy were reported to be 0.7 eV [82] and 1.95eV [13], respectively; whereas that of Fe^{2+} interstitials were found to be 1.60eV [14], thus slightly more mobile than oxygen vacancies. The n-type character of the TF/IF400 oxides suggest that metal vacancy is a minority defect and exists in a relatively neglectable concentration [17].

Since the thickness of α-Fe_2O_3 outer layer is approximately 0.86 μm, the irradiation in IF400 is expected to damage mostly the α-Fe_2O_3 phase. The DBS measurement (Figure 4.11b) detected an increase in vacancy concentration, along with the formation of larger sized vacancy clusters revealed by PALS (Figure 4.13) analysis. In other words, for TF/IF800, proton irradiation can result in higher concentration of defects and larger sized vacancies. Yano et al. found that anion transport is dominated by the recombination of Frenkel defects at low temperature (>300°C) and that the oxygen self-diffusivity (i.e., oxygen vacancy diffusion) can be raised by at least two orders of magnitude upon 0.1 dpa of proton irradiation in α-Fe_2O_3 at 450 °C [83]. Despite the undergoing discussion whether vacancy clusters reduce or enhance transport [78, 84-86], the clusters of vacancies in oxides could exhibit a higher mobility than mono-vacancies [84].

In conclusion, PAS suggests that proton irradiation increases the average vacancy concentration for all irradiated materials. The rise in vacancy concentration for the IF400 sample may be partially related to the accumulation of vacancies at the metal/oxide interface. PALS found that irradiation reduced the size of vacancy clusters in the IF400 sample, whereas an opposite effect was observed on the IF800 sample with evidence on the formation of vacancy clusters. This suggests it may be easier to form vacancy clusters from irradiation depending on the grown oxide. At the same irradiation level, Fe_3O_4 vacancy clusters in IF400 form less readily than Fe_2O_3 vacancy clusters in IF800. Further illustration of the defect behavior as a function of oxidation temperature can be found in the oxidation discussion section in Chapter 6.

4.3.5 Results of PAS study oxidation time effects on Fe-oxide defects

Figure 4.14 shows the damage profile due to proton irradiation calculated the SRIM for the 600°C samples. The dpa profile and proportion of the dpa that is due to O vacancies are plotted on the left axis. On the right axis, the final proton distribution is shown. Dpa and ion distribution results are based on a SRIM monolayer calculation, while the oxygen vacancy values are based on a full cascade calculation.

The damage profile for both materials is again relatively flat up to a peak at about 0.03 dpa at a depth of 0.81μm [76]. For IF600, there is a relatively flat region of the dpa profiles is primarily in the Fe_3O_4 layer. However, the peak damage is in deeper into the oxide layer to a peak dpa of 0.3.

As shown in Figure 4.14, the peak of the ion distribution is expected to be deeper in the material than the dpa peak. In Figure 4.14, this difference is much smaller due to the presence of O and its lower displacement energy (28 eV vs. 40 eV for Fe, based on Konobeyev et al. [77])

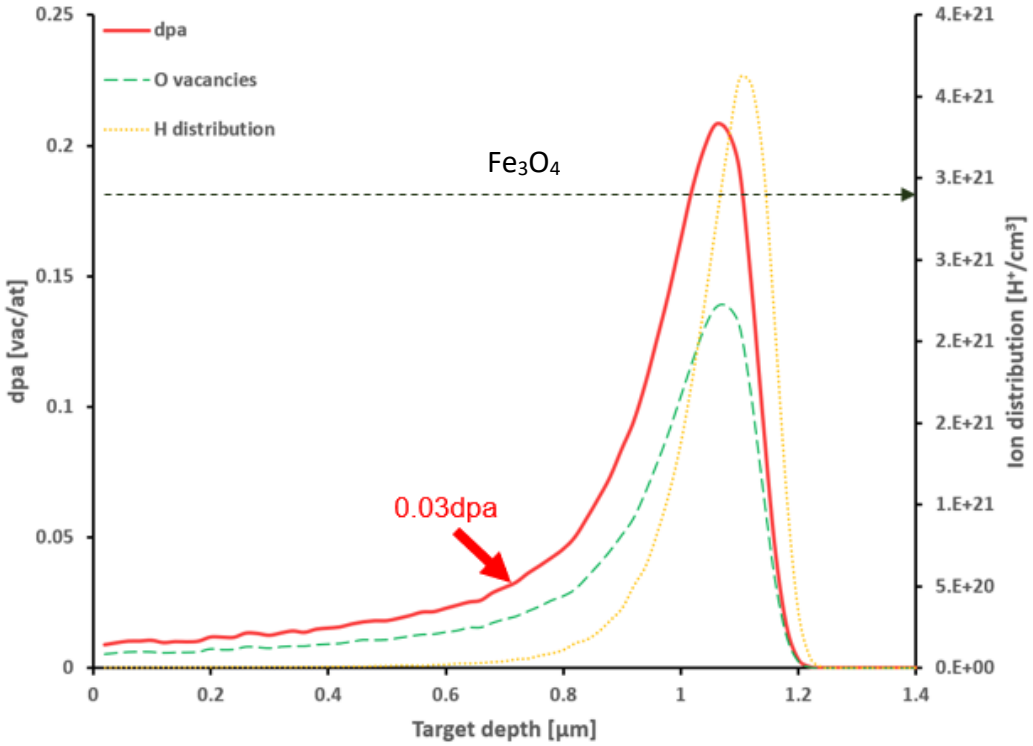

Figure 4.14: Damage profile of proton irradiation calculated by SRIM for the IF600 samples. The red arrow indicates the irradiation depth corresponds to 0.03 dpa with 200 keV protons. The total dpa, O-vacancies, and hydrogen distribution results are obtained based on a full cascade calculation mode, where threshold displacement energies of 40 eV for Fe and 28 eV for O are used.

Figure 4.15 shows the results from the DBS investigation of the 600°C oxides. The 600°C oxides show an increase in S-parameter after radiation damage, indicating higher vacancy defect concentrations on average after proton irradiation. Again, the large decreases in the S-parameter in the first 50 nm are due to partial positron annihilation at surface states from back-diffused positrons. Positrons after implantation diffuse in any direction through the crystal, however, at low implantation energies, they can back diffuse to the surface and are trapped in the surface pseudo potential, where they annihilate after longer lifetimes on average compared to bulk or localized annihilation. This increases the S-parameter which scales with the positron lifetime.

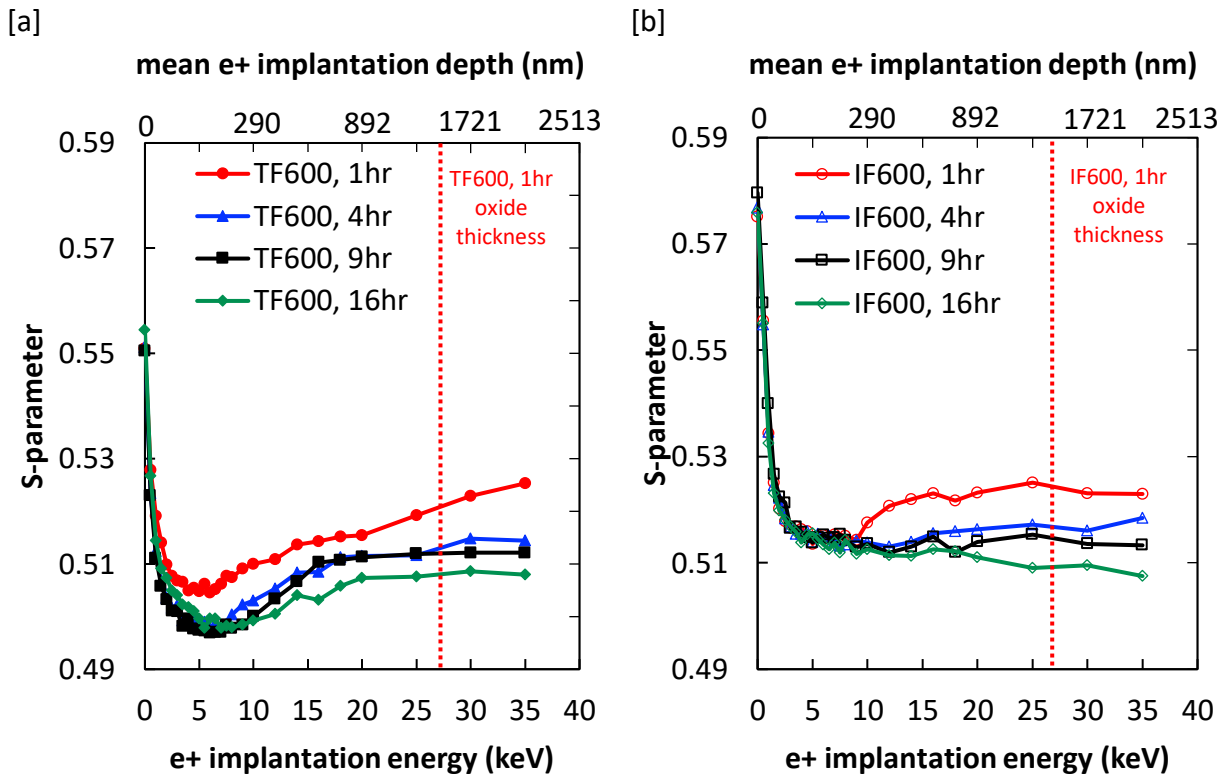

Figure 4.15: S-parameter for pre-irradiation and post-irradiation pure Fe oxidized in air at 600°C, 1hr from DBS.

The 600°C oxides show decreases in S-parameter with oxidation time, indicating lower defect concentrations over time. The 600°C oxides show increases in S-parameter after radiation damage, indicating higher defect concentrations after irradiation. The dotted line in the figure marks the thickness of the Fe_3O_4 interface within the oxide at 1.3 microns for TF600, 1hr and IF600, 1hr. The largest difference from radiation damage is in the top Fe_3O_4 layer of the oxide. Note that the S-parameter at each implantation energy is an average over a region that is spread out due to positron implantation and subsequent diffusion and does not correspond to a precise depth in the sample.

To evaluate vacancy defect microstructure in the oxide layers and further characterize the decrease of defect concentration as a function of annealing time, PALS results on the samples are presented in Figure 4.16 and Figure 4.17. From Figure 4.16, the 600°C samples showed a decrease in the average defect size (τ_{av}) after irradiation compared to the as-oxidized case. These findings agree with DBS results, as the S-parameter trends share the same overall behavior in the 0 – 12 keV region.

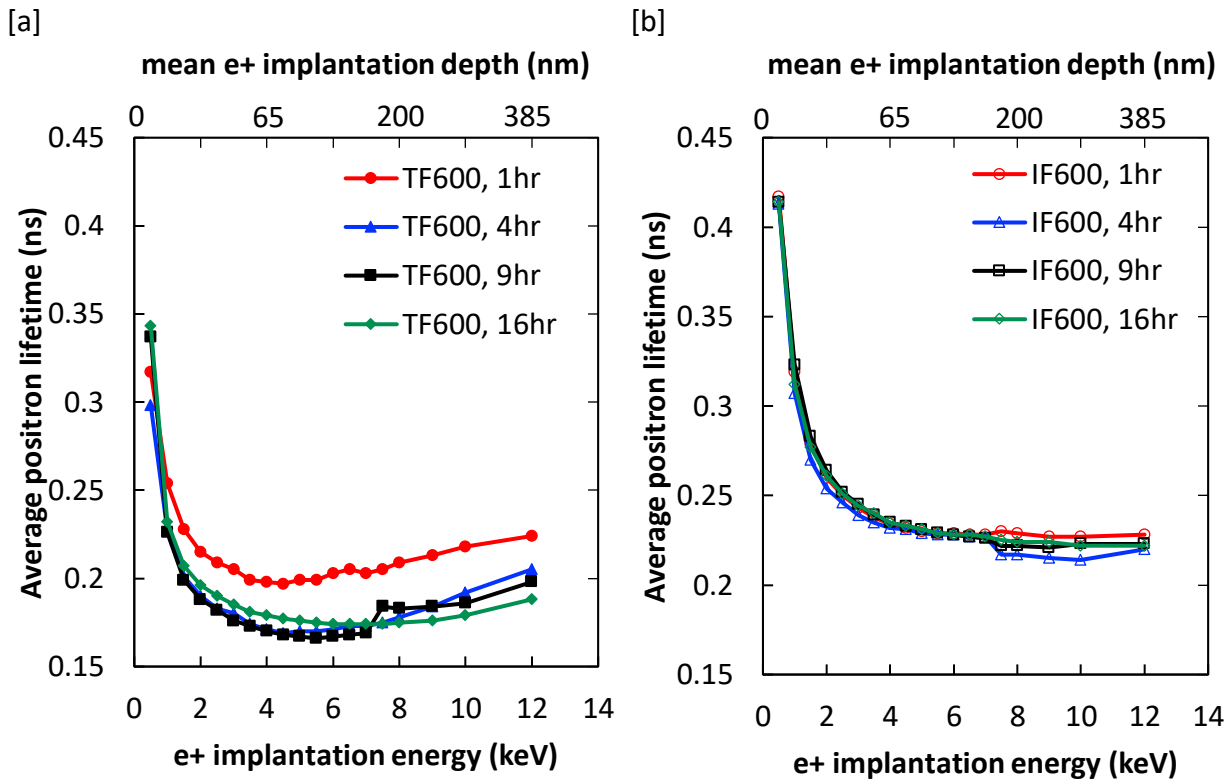

Figure 4.16: Average positron lifetime, τ_{av}, for (a) pre-irradiation and (b) post-irradiation pure Fe oxidized in air at 600°C from PALS.

By fitting the PALS data using the PALSfit code [R7], specific lifetimes and their relative intensities were obtained, which represent defect sizes and relative concentrations within the oxide layers, respectively (Figure 4.17 and Figure 4.18). Larger lifetimes correspond to larger defect complexes, and higher intensities of respective lifetimes reflect higher associated relative defect densities. Two lifetime components were analyzed for each sample, as seen in Figure 4.17 and Figure 4.18 (the third component originating from the surface ortho-positronium was omitted for clarity due to its residual intensity).

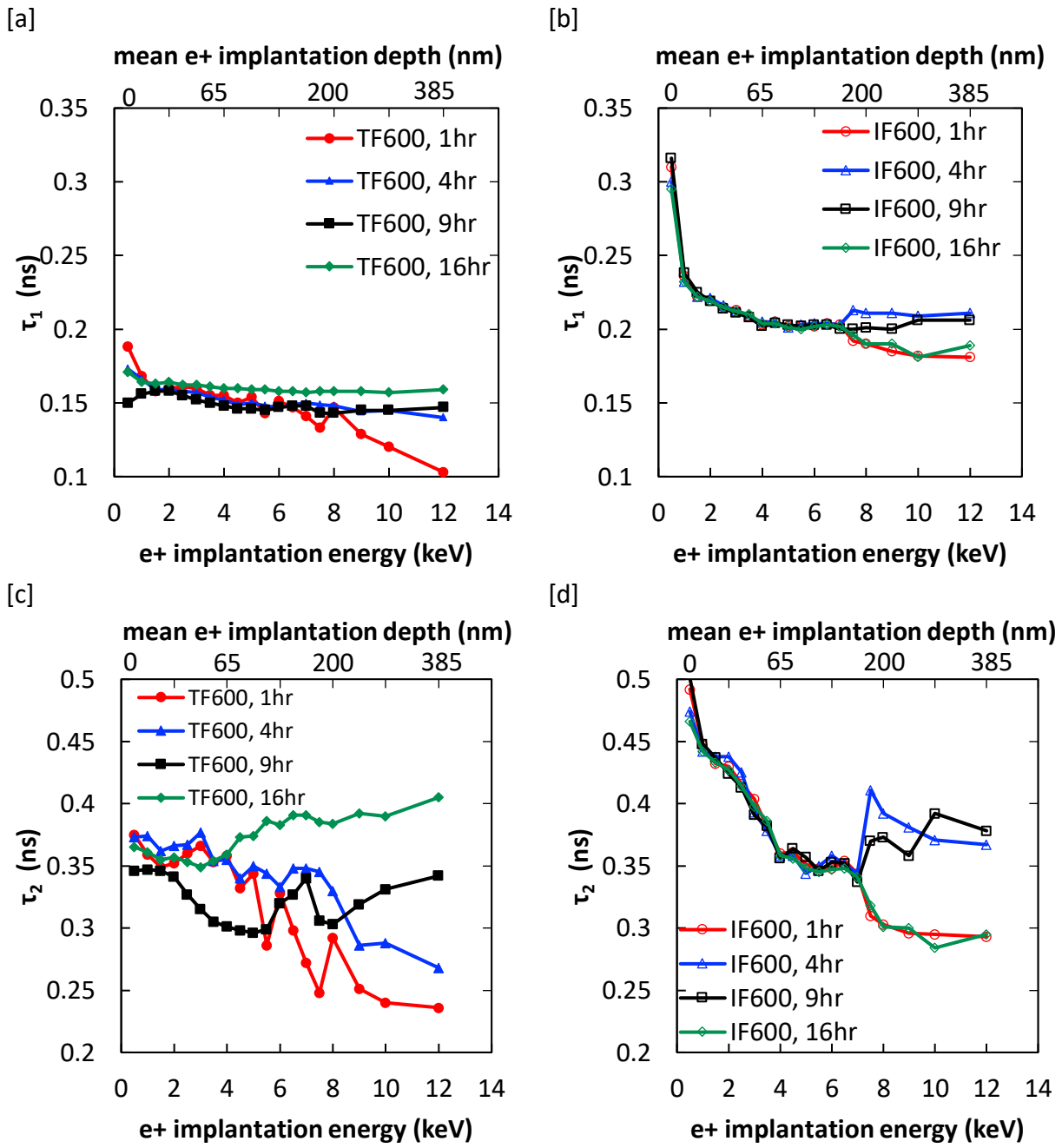

Figure 4.17: Positron lifetime components τ_i (a,b) calculated from PALS spectra decomposition for pre-and post-irradiation pure Fe oxidized in air at 600°C.

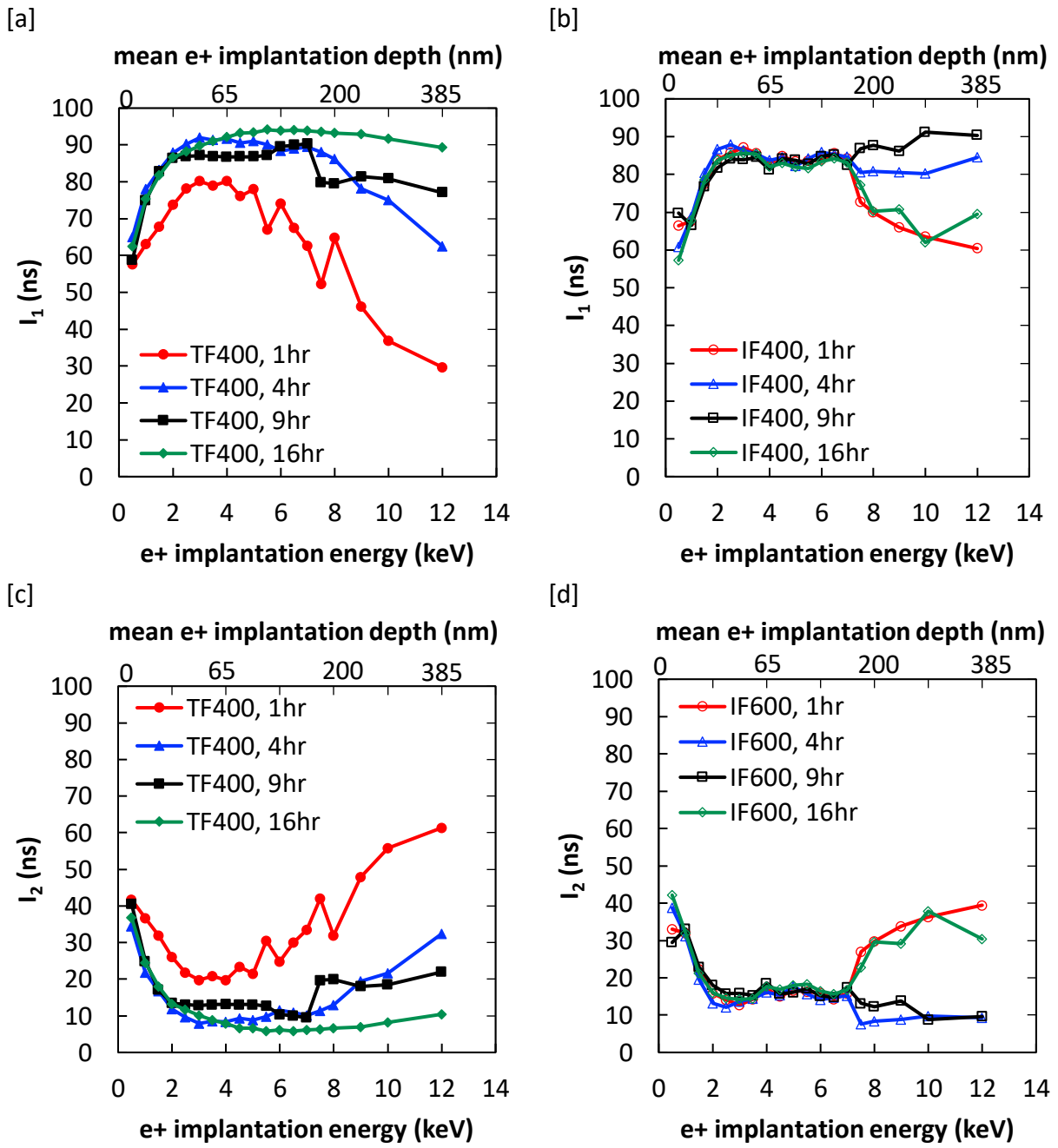

Figure 4.18: Positron lifetime components' τ_i relative intensities I_i calculated from PALS spectra decomposition for pre-irradiation (a,c) and post-irradiation (b,d) pure Fe oxidized in air at 600°C for different oxidation times.

The 600°C samples showed an increase in both τ_1 lifetime components after irradiation compared to the as-oxidized case indicating decreasing defect size for both components (Figure 4.17). Larger τ_2 lifetime components remain relatively constant in the unirradiated oxides, but the larger variance in τ_2 for irradiate oxides suggest more variance in the size of the larger defects after oxide irradiation.

Interestingly, except for the IF600, 16h, the relative intensities of the defects sampled in the 600°C samples did not change much before and after irradiation (Figure 4.18). After 16 hours of oxidation, the oxide seemed to exhibit more large defects, but this could be due to issues with data acquisition explained later. With the stoichiometry of the oxide layers assumed to be Fe_3O_4, one could start to interpret the different defect states that might have been sampled by the positrons. It is noted that the largest achievable E_p = 12 keV during PALS did not allow positrons to probe as deep as DBS.

Note there are observed discontinuities in the PALS analysis in Figure 4.17 and Figure 4.18 around 7 keV. During the PALS measurements, as positron implantation energy increased, the final acceleration scheme for implanted positrons was switched at 7 keV. Before 7 keV, incoming positrons at MePS had a transport energy of 2 keV and were being accelerated (or decelerated) to their final energy. After 7 keV, positrons had a much higher transport energy and were always decelerated at the sample to their final energy. This switching was attempted for the first time during the beamtime of the measurement, and there were problems with discharges (due to the huge difference between transport energy and final energy at the sample). Usually, that switching does not influence the lifetime parameters at all, but this issue combined with previously mentioned backscattering of positrons at low energies created discontinuities in analyzed lifetimes at 7 keV. Finally, to solve the problem, future experiments must install a larger sample chamber (to reduce the influence of discharges and distortions) and apply a uniform acceleration scheme (so that no switching at 7 keV will be necessary).

4.3.6 Discussion of PAS study oxidation time effects on Fe-oxide defects

The PAS results suggest that proton irradiation increases the average vacancy concentration for all irradiated materials. Without irradiation, the effect of oxidation time is mainly the stabilizing of defect sizes as the oxide layer grows thicker. The oxide defects are further away from the metal/oxide interface nonequilibrium defects as the oxide grows into the material, and the defect sizes sampled after long oxidation are likely the ones stabilized in thermal equilibrium. However, irradiation seems to dominate this thermal equilibrium in long oxidation, introducing an overall number of defects that are sampled as the predominant defects within the oxide. This suggests it may be easier to form persistent, surviving vacancy clusters from nonequilibrium defects from oxide irradiation rather than from nonequilibrium defects at the metal/oxide interface. Further illustration of the defect behavior as a function of oxidation time can be found in the oxidation discussion section in Chapter 6.

4.3.7 Conclusion

Proton irradiation increases defect concentration in all oxides because irradiation introduces non-equilibrium defects into the oxides, which already contain thermal defects from oxide formation. However, fundamental factors that govern their response to irradiation are very different. This is because proton irradiation is effectively damaging the magnetite (Fe_3O_4) film on IF400 and IF600 series oxides, whereas the case for IF800 is the hematite (α- Fe_2O_3) film.

The rise in vacancy concentration for the IF400 sample may be partially related to the accumulation of vacancies at the metal/oxide interface. PALS found that irradiation reduced the size of vacancy clusters in the IF400 sample, whereas an opposite effect was observed on the IF600, 1hr and IF800 samples with evidence on the formation of vacancy clusters. This suggests it may be easier to form vacancy clusters from irradiation depending on the grown oxide.

The defects are primarily determined by which oxide is grown at what temperature, because as the oxide grows thicker and closer to thermal equilibrium, there are not large changes in relative defect concentration. The main effect of ageing oxides is the stabilizing of defect sizes. However, irradiation seems to dominate this thermal oxide defects, introducing an overall number of defects that dominate and stabilize within the oxide. This suggests it may be easier to form persistent, surviving vacancy clusters from oxide irradiation nonequilibrium defects rather than metal/oxide interface nonequilibrium defects.

4.4 Studying grain boundary defects in Fe using PAS

4.4.1 Introduction to importance of grain boundaries as sinks for defects during irradiation

Other than dislocations, grain boundaries are perhaps one of the most important sinks for non-equilibrium point defects during irradiation. In rate theory, it is a critical sink component of the modeling. Therefore, it was of great interest to look at the differences in surviving irradiation defect concentration in a single crystal versus polycrystal material. Iron was selected as the candidate material for this grain boundary (GB) investigation because of its relative abundance, well-characterized defect lifetimes from previous positron studies, and relevance to nuclear reactor structural materials.

4.4.2 Methods and sample preparation used to study grain boundaries in iron using PAS

Single crystal and polycrystal Fe coupons (99.999%, Alfa Aesar) were metallographically polished to 1200 grit surface finish. Two samples were fabricated for each crystal condition. One sample from each condition was subjected to proton irradiation.

Samples were irradiated with 200 keV protons up to a fluence of $6.02*10^{16}$ ion/cm^2 on the 200 kV Danfysik ion implanter at the Ion Beam Materials Laboratory (IBML) at Los Alamos National Laboratory. The sample stage was actively air-cooled to keep the sample temperature below ~35^{o}C during the approximately 23-hour-long irradiation. The corresponding damage profile was calculated using the Stopping and Range of Ions in Matter [76] software for each sample and plotted in Figure 4.19. In the SRIM simulations, a displacement threshold energy of 40 eV for Fe atoms was assumed, and the quick K-P cascade mode was used. Both the irradiation and the SRIM calculation were performed at an angle of 5 degrees.

The samples were sent to the Institute of Radiation Physics at Helmholtz-Zentrum Dresden – Rossendorf (HZDR) for positron annihilation spectroscopy (PAS) to characterize the defect type and density at different depths for the grown oxide layers. Details on the PAS data acquisition are given in Section 4.1. For lifetime measurements, PALS spectra were then deconvoluted into a few discrete lifetime components using the PALSfit software [8], which directly show evidence of different defect types (sizes) and their corresponding relative intensities, quantifying the overall concentration of each defect type.

4.4.3 Results of PAS study on grain boundaries effect on defects during irradiation

Figure 4.19 shows the damage profile due to proton irradiation calculated the SRIM. On the right axis, the final proton distribution is shown. The damage profile is relatively flat up to a peak at about 0.03 dpa at a depth of 0.8 microns.

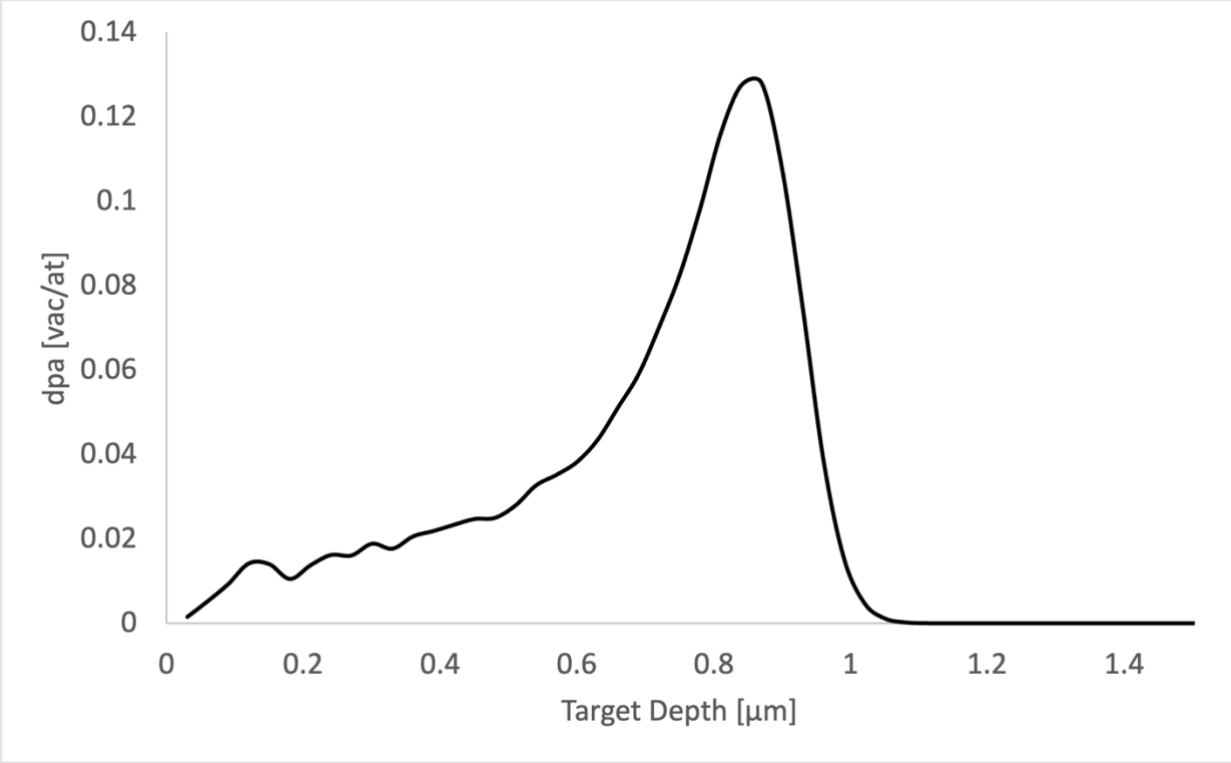

Figure 4.19: Damage profile of proton irradiation calculated by SRIM for the Fe samples. A threshold displacement energy of 40 eV for Fe was used.

Figure 4.20 shows the results from the DBS investigation of the Fe samples. Both show an increase in S-parameter after radiation damage, indicating higher vacancy defect concentrations on average after proton irradiation. The S-parameter curve looks similar to the damage profile, with the peak damage around 0.8 microns.

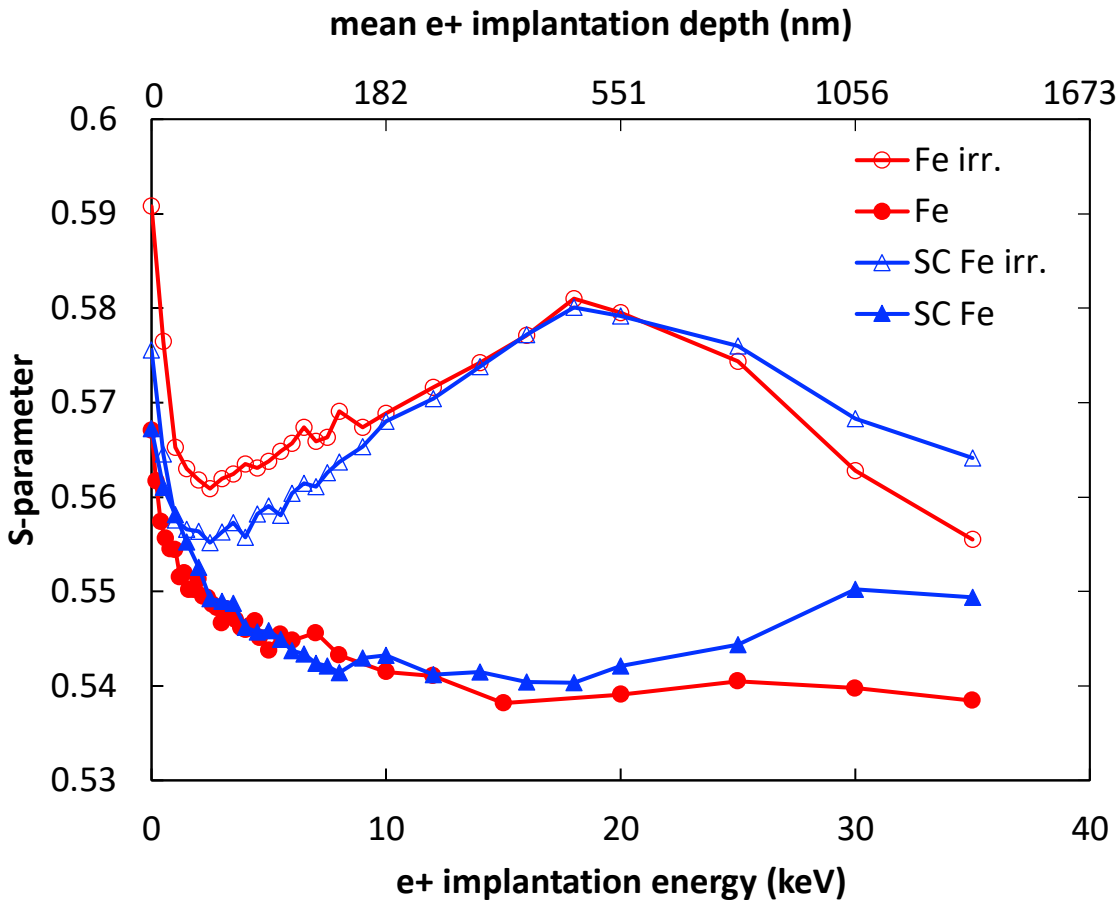

Figure 4.20: S-parameter for pre- and post-irradiation SC and polycrystal Fe from DBS.

In the oxidized samples, the large decreases in the S-parameter in the first 50 nm are due to partial positron annihilation at surface states from back-diffused positrons. Positrons after implantation diffuse in any direction through the crystal, however, at low implantation energies, they can back diffuse to the surface and are trapped in the surface pseudo potential, where they annihilate after longer lifetimes on average compared to bulk or localized annihilation. This increases the S-parameter which accordingly scales with the positron lifetime.

To evaluate vacancy defect microstructure in the oxide layers and further characterize the decrease of defect concentration as a function of annealing time, PALS results on the samples are presented in Figure EXC3. The increase in the average positron lifetime is comparable to the S-parameter increase in this region.

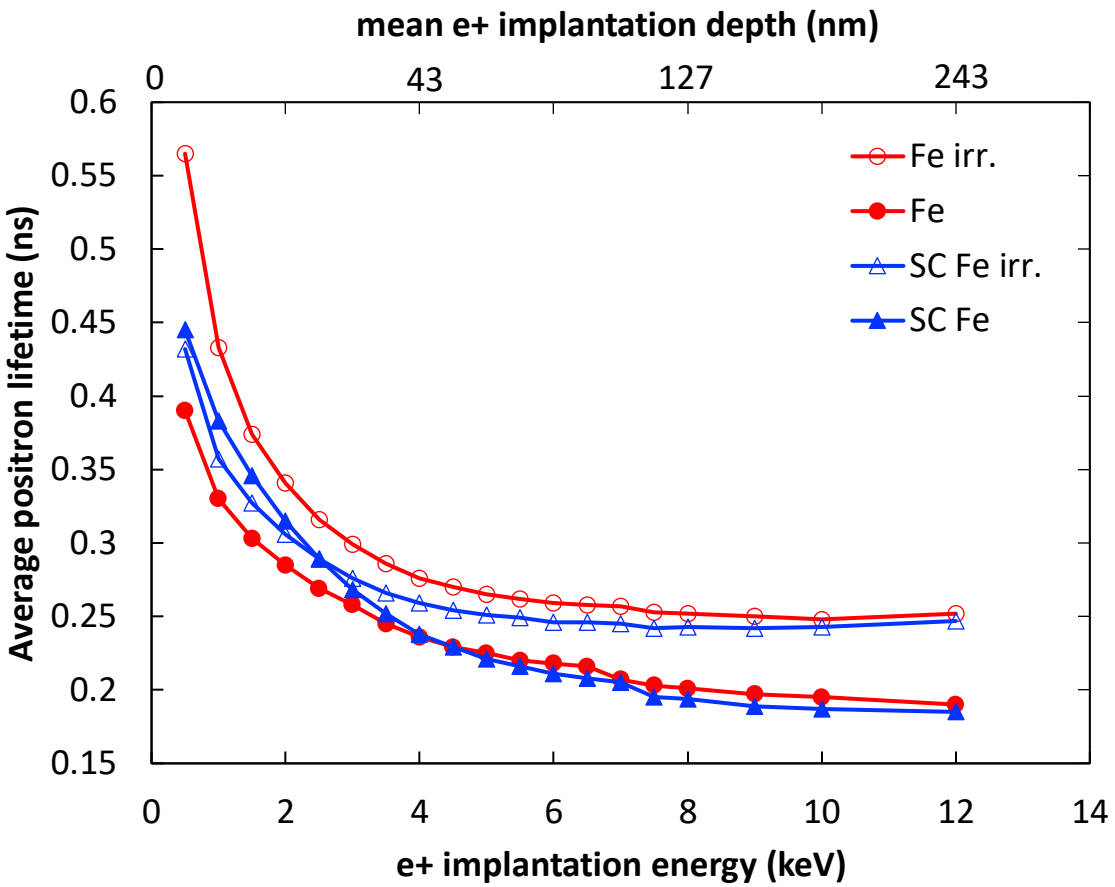

Figure 4.21: Average positron lifetime, τ_{av}, for pre- and post-irradiation SC and polycrystalline Fe from PALS.

By fitting the PALS data using the PALSfit code [8], specific lifetimes and their relative intensities were obtained, which represent defect sizes and relative concentrations within the oxide layers, respectively (Figure 4.22). Larger lifetimes correspond to larger defect complexes, and higher intensities of respective lifetimes reflect higher associated relative defect densities. Two lifetime components were analyzed for each iron sample, as seen in Figure 4.22. Note the third component originating from the surface ortho-positronium was omitted for clarity due to its residual intensity.

[a]

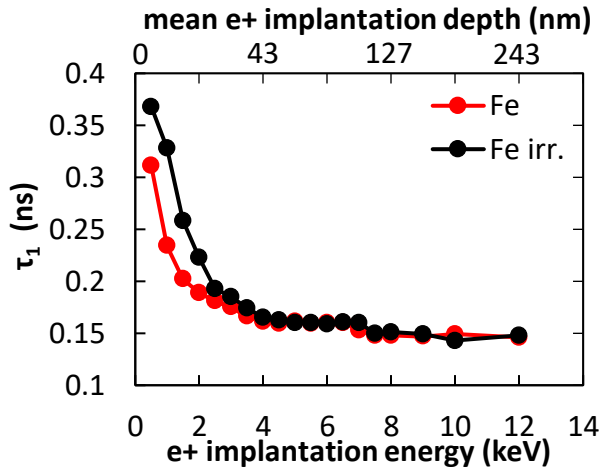
mean e+ implantation depth (nm)
0
43
127
243
Fe
Fe irr.
τ1 (ns)
e+ implantation energy (keV)

[b]

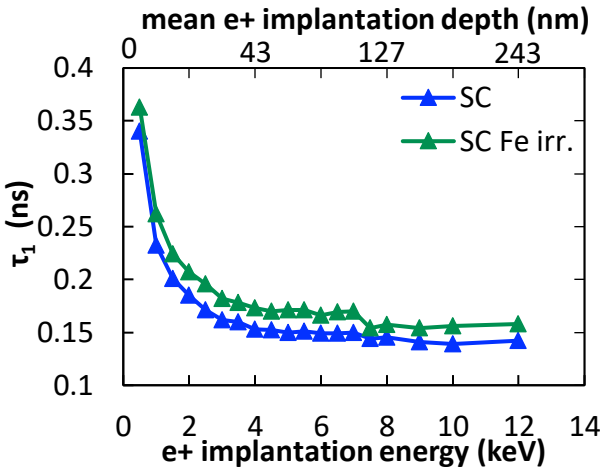
mean e+ implantation depth (nm)
0
43
127
243
SC
SC Fe irr.
τ1 (ns)
e+ implantation energy (keV)

[c]

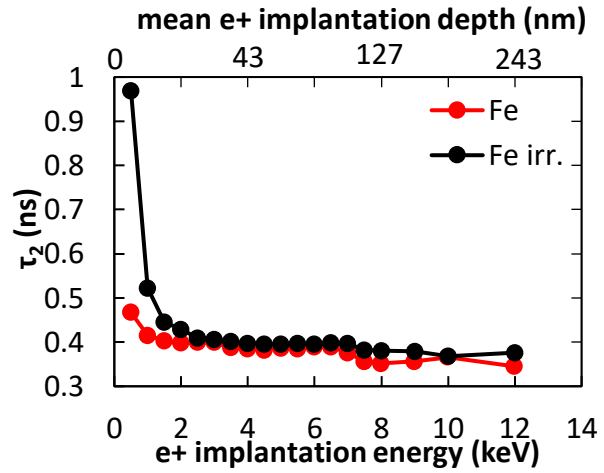
mean e+ implantation depth (nm)
0
43
127
243
Fe
Fe irr.
τ2 (ns)
e+ implantation energy (keV)

[d]

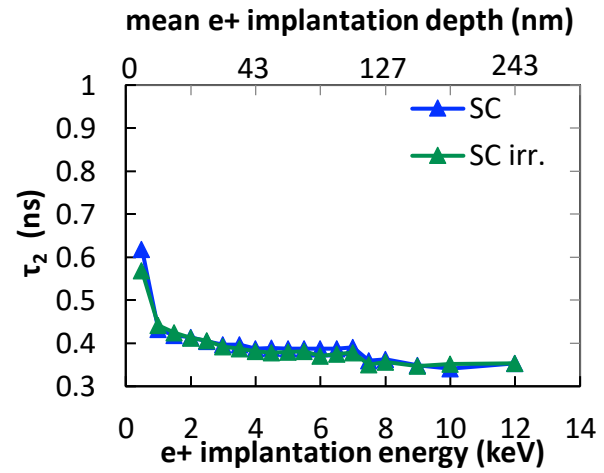
mean e+ implantation depth (nm)
0
43
127
243
SC
SC irr.
τ2 (ns)
e+ implantation energy (keV)

[e]

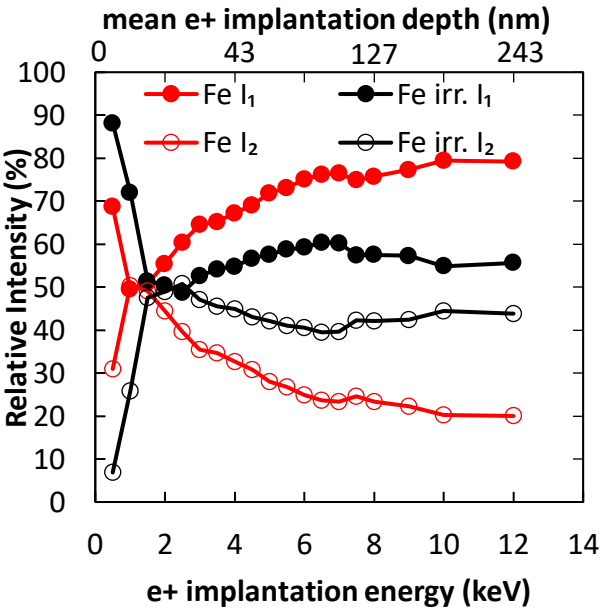
mean e+ implantation depth (nm)
0
43
127
243
Fe I1
Fe irr. I1
Fe I2
Fe irr. I2
Relative Intensity (%)
e+ implantation energy (keV)

[f]

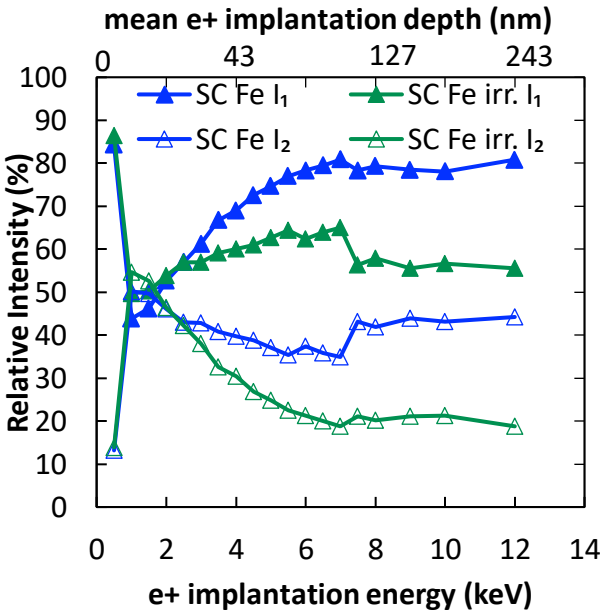
mean e+ implantation depth (nm)
0
43
127
243
SC Fe I1
SC Fe irr. I1
SC Fe I2
SC Fe irr. I2
Relative Intensity (%)
e+ implantation energy (keV)

Figure 4.22: Positron lifetime components τ_i (a) and their relative intensities I_i (b) calculated from PALS spectra decomposition for pre- and post-irradiation SC and polycrystal Fe from PALS.

With a τ_1 defect lifetime of around 150 ps (for E_p > 3 keV) this value is larger than the value for defect-free bulk (108 ps) and smaller than a vacancy value (190 ps) in pure Fe [87, 88]. For the case of pure iron, an additional component can be found representing a reduced bulk lifetime. Then, the first lifetime component here changed to around 160 ps which is very close to the lifetime of dislocations in pure Fe (165 ps) [87, 88]. Since the decomposition into three components was not very stable, only results from a two-component fit will be shown and discussed here. Note that τ_1 is likely a mixture of positron annihilation in the bulk state and dislocations. For τ_2, a lifetime value of around 400 ps would be a cluster containing more than 15 vacancies (if compared to pure Fe). See Table 4.3 for simulated positron lifetime values in monovacancies and vacancy clusters in Fe.

Fe vacancy cluster size	**e^+ Lifetime (ps)**
1	190
2	197
3	232
4	262
6	304
10	334
15	386

Table 4.3: Positron lifetime values in monovacancies and vacancy clusters in Fe. The table was reproduced from the data reported in Puska et al. [88]

4.4.4 Discussion of PAS study on grain boundaries effect on defects during irradiation

The irradiation seems to increase the defect concentration of the larger vacancy clusters in both polycrystal and SC Fe. From both doppler broadening and average lifetime measurements, the irradiation effect of the vacancy clusters looks similar in single crystal and polycrystal Fe. Analyzing the lifetime components, however, reveals small differences in the samples. Before irradiation, from Figure 4.22, the SC Fe seems to have slightly higher relative small defect concentration I_1 defects present than the polycrystal Fe, likely due to the GBs acting as sinks for polycrystal defects. After irradiation however, it seems the samples exhibit the same behavior, that is I_1 defect intensity is still slightly larger for the SC samples. Even though non-equilibrium defects are introduced from irradiation, the additional presence of grain boundaries could prevent large vacancy clusters from forming in polycrystal Fe.

4.4.5 Conclusion

In this experiment, grain boundaries were tested as sinks to nonequilibrium radiation defects by irradiating single crystal versus polycrystalline iron. Irradiation is known to create stable vacancy clusters in Fe, but grain boundaries prevent vacancy clusters from forming as monovacancies annihilate with existing grain boundaries. As expected, grain boundaries could prevent large vacancy clusters from forming in polycrystal Fe.

5. In-situ PAS measurements and results on nuclear relevant materials

5.1 Simulated PAS study of non-equilibrium radiation point defects in Fe

5.1.1 Introduction to the importance of PAS for non-equilibrium radiation point defects in Fe

First, it must be established that positron spectroscopy is an appropriate tool for in-situ work. In order to assess the feasibility of directly combining in-situ PALS with ion-beam before experimental measurements, Section 5.1 provides the theoretical and computational background necessary for an in-situ combined experiment. An overview is depicted in Figure 5.1, explaining the parallels between this simulation section and future experimental approaches. The simulation models the radiation damage from the ion beam and coincident positron implantation for positron spectroscopy.

Iron was carefully chosen as the candidate material for the simulation. Cladding and fuel are exposed to the highest dose in a nuclear reactor environment and thus are expected to see significant property changes depending on the type of reactor and material chosen. Fe-based alloys are widely used in the nuclear industry as structural materials like core steel due to their excellent high-temperature mechanical properties, corrosion resistance, and resilience to radiation [1-4]. Because reactor environments expose these Fe-alloys to a complex array of environmental variables such as radiation and corrosive impurities, it is especially important to fully characterize iron's irradiation performance for safety analysis.

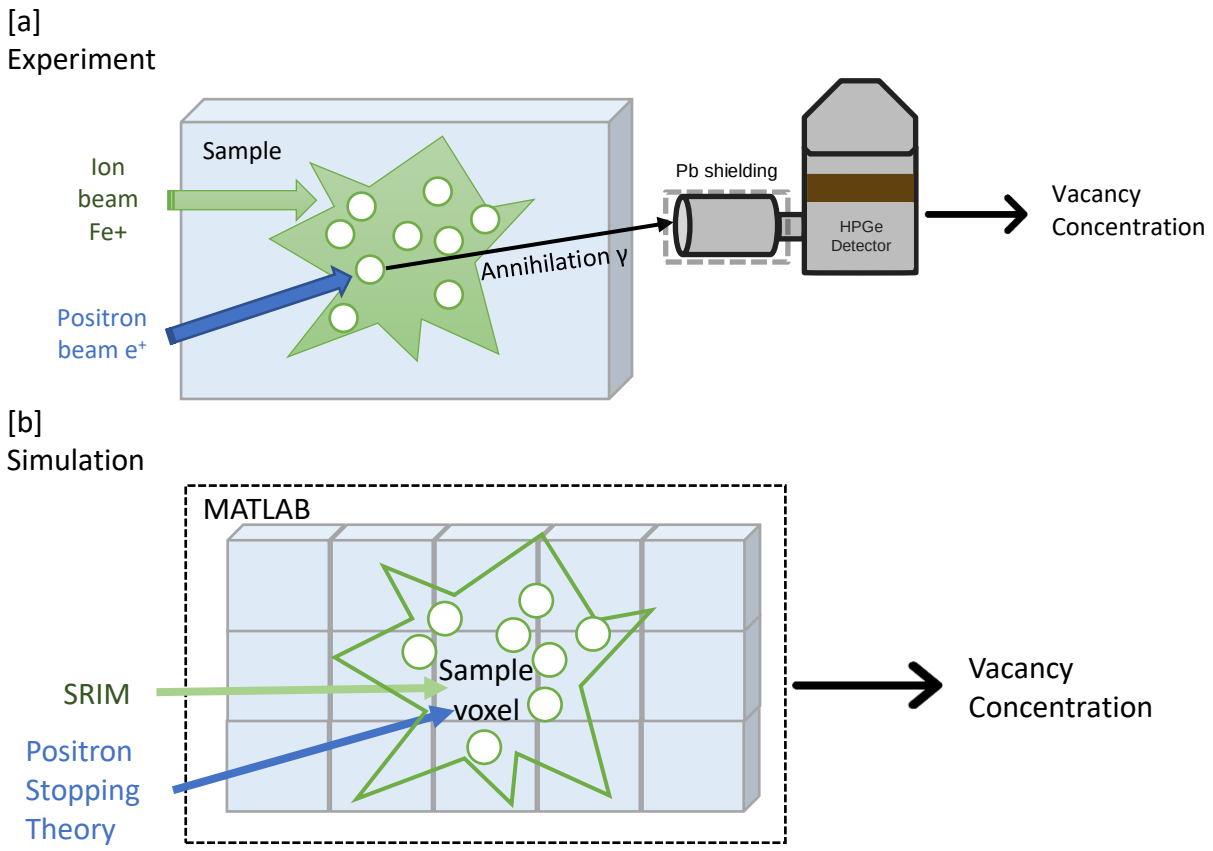

Figure 5.1: Schematic overview of methods from hypothetical experiment and modelling efforts. [a] A future experimental effort would involve in-situ positron spectroscopy (DBS and PALS) on small, radiation-induced defects from a coincident ion beam. Conversely, [b] the MATLAB simulated experiment of an in-situ simultaneous irradiation and PALS experiment on vacancy concentration was carried out using radiation damage and positron stopping theory.

5.1.2 In-situ PAS and radiation damage modeling and simulation methods

To analyze radiation damage vacancies in nuclear reactor structural materials, this in-situ model simulated Fe^{2+} ion beam irradiation with coincident, simultaneous positron lifetime spectroscopy on a pure Fe sample. Iron was selected as the candidate material for this simulated experiment because of its well-characterized defect characteristics from previous positron studies and its relevance to nuclear reactor structural materials.

The model simulation of in-situ ion beam irradiation and positron annihilation spectroscopy performed used a voxel approach in MATLAB [5] to simulate the radiation damage from the ion beam and coincident positron implantation from the positron beam. The sample is split into model geometric cubes, called voxels, and local information about ion beam and positron beam effects for each voxel is stored as a 3D matrix in MATLAB [5]. Ion beam damage and positron implantation rates are stored in these 3D voxel matrices for locations inside the sample, and two matrices: (1) vacancy concentration from ion radiation damage and (2) positron implantation rate

from coincident positron beam are overlaid to calculate how many in-situ monovacancies in a single voxel are 'seen' by incoming positrons. These calculations can compare theoretical results to future experimental efforts combining ion beam irradiation and simultaneous positron annihilation spectroscopy.

Even though the positron beam in an experiment is likely coming in at an angle relative to the ion beam, the positron implantation profile should overlap the expected damage region from the ion beam. Further, it is ideal for the positrons to implant and sample locally within the maximum damage region from the ion beam. To do this, the incoming positron beam must be energetically narrow relative to the ion beam FWHM so all incoming positrons sample the near-constant dpa region. Figure 5.2 shows a 3D representation of the overlap between the incoming beams. Ion and positron beam percentages are shown at different x-y positions in the sample, that is, what percent of particles from the overall beams will be present at each location. The positron beam width is narrower than the ion beam, so positrons will primarily locally sample the damage region from the ions.

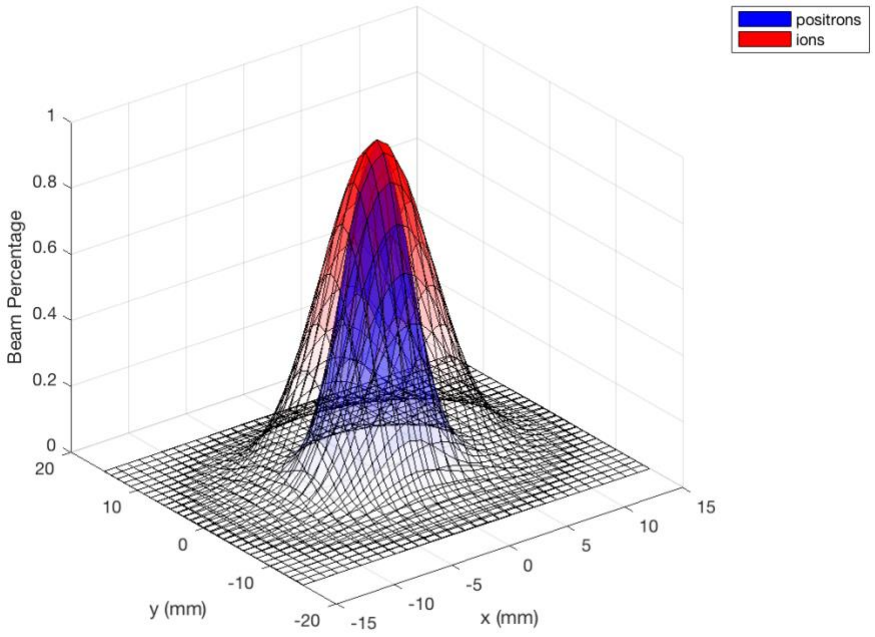

Figure 5.2: 3D representation of overlap between beam intensities from ion irradiation and positron implantation. Normalized beam percentages are shown for comparison, or what percent of particles from each incoming beam is present at different x-y locations in the sample. Ideally, the positron beam intensity profile should be narrow and fit inside the ion beam in order for the positrons to sample locally within the maximum damage region left by the ion beam.

The radiation damage in Fe was simulated using the parameters of the tandem ion beam at Los Alamos National Laboratory (LANL) Ion Beam Materials Laboratory and standard radiation damage rate theory (Equation 1). SRIM-2008 [6] was used to determine the vacancy formation

rate from the ion beam. In the SRIM simulations, a displacement threshold energy of 40 eV was assumed for Fe [7]. These simulations were run in the full cascade mode. At this point, it is important to note that full cascade delivers about a factor of two higher dose rate as the quick Kinchin-Pease (K-P) model. The quick K-P model only follows the primary knock-on atom path through the material, but the detailed model considers all the secondary knock-on atoms causing chains of further displacements within the material. Further, the quick K-P model is the same model used in MCNP calculations and is highlighted in the ASTM standard by R. Stoller et al. [7, 8]. For discussion, one may use the calculation as a guideline and divide the dose rate caused by the incoming ion beam by a factor of two for the quick K-P model. In either case, incident positrons will sample only a fraction of total damage delivered (~10^{-3} defects sampled), so the differences between detailed cascade and quick K-P model does not change the feasibility of this proposed experiment. In order to truly compare the measured defects as a function of dose rate to the calculated nonequilibrium surviving defects one would absolutely have to use detailed modeling calculations (e.g., MD).

The model characterizes the ion beam intensity (in μA/mm^2) using a Gaussian beam profile and beam FWHM of 10 mm for incident 2 MeV Fe^{2+} ions into pure Fe at room temperature, 293.15 K. The ion beam intensity is assumed to be the symmetric in the x-y directions, perpendicular to the ion beam propagation into the sample (z), and the sample is irradiated to a total fluence of 5.65 x 10^{14} ions/cm^2. Combining vacancy calculations from SRIM-2008 [6] and the ion beam intensity from the LANL beam parameters, the model then calculates the dpa rate (in dpa/s) in the Fe sample at different locations inside the sample. The expected vacancy concentration is calculated from the standard rate theory calculation (Equation 2.5) using the dpa rate within the sample. The expected vacancy concentration is stored as a 3D matrix measuring radiation damage at each position inside the sample. This radiation damage cascade matrix was then overlaid with the positron implantation rate matrix to calculate a 3D matrix with the observable monovacancy concentration 'seen' by the positrons, giving the PAS-observable monovacancy concentration at each location inside the sample.

The positron implantation rate was simulated using the parameters of the positron beam at the Helmholtz-Zentrum Dresden-Rossendorf (HZDR) in Dresden, Germany [9-11] and a Mahkov positron implantation profile from literature (Equations 2.7 and 2.9) [12, 13]. The positron beam intensity (in positrons/s·mm^2) is calculated from a Gaussian beam profile with FWHM of 6 mm for a fluence of 10^6 positrons/s. Similar to the ion beam, the positron beam intensity is symmetric in the x-y directions, perpendicular to the beam propagation (z).

The positron implantation rate is the probability that a positron will be at a particular voxel, or that a positron will thermalize at a particular location inside the sample (Equation 2.9), and thus be available to interact with a vacancy within a voxel. Again, subsequent migration of the positrons was neglected in this analysis. The implantation rate normalized the number of positrons found at a particular location within a voxel to the total number of positrons in the incoming beam. Finally, the 3D radiation damage cascade matrix was overlaid with the positron implantation rate 3D matrix to calculate a 3D matrix of the PAS-observable monovacancy concentration at each location inside the sample. This calculation assumes both beam centers

are concentric and aligned normal to the sample surface. The average PAS-observable vacancy concentration over the entire 3D matrix for each location in the sample is shown in the results.

5.1.3 Results and Discussion of PAS study on non-equilibrium radiation point defects in Fe

The damage profile from SRIM was used to calculate a dpa-dependent vacancy concentration using Equation 2.5, and Figure 5.3 shows the vacancy concentration in 4 different planes, or slices, of the implanted Fe. The increase in vacancy concentration trend between 0-400 nm from the damage profile in the can also be observed here.

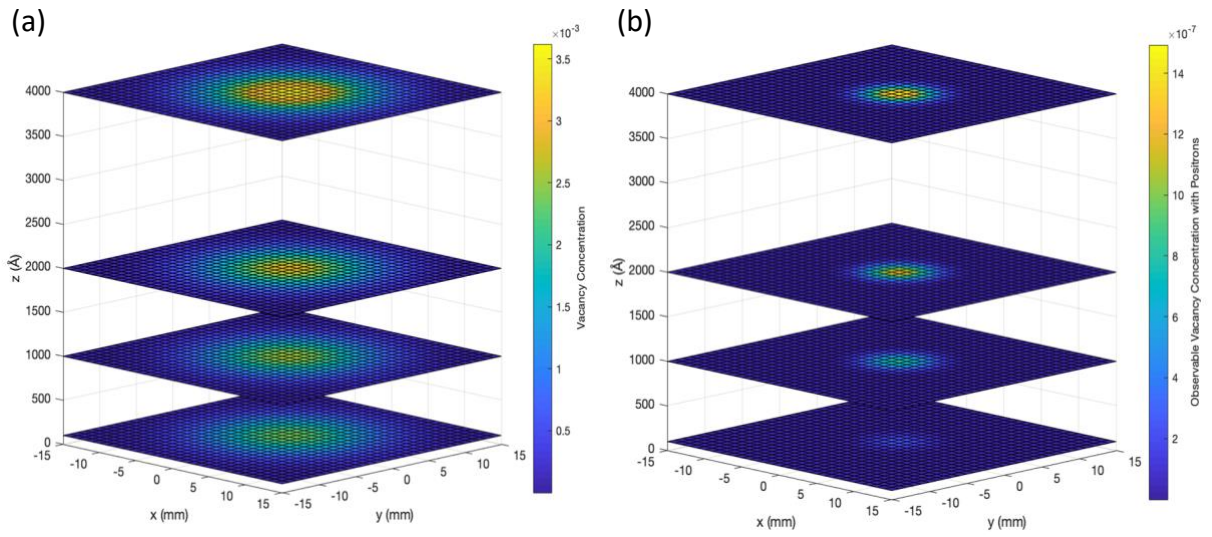

Figure 5.3 (a): Calculated vacancy concentration due to radiation damage cascade in-situ by 2 MeV Fe^{2+} ions into Fe. Slices taken at 10, 100, 200, and 400 nm. The ion beam is incoming from the (centered at (0,0,0)). Damage increases as depth increases along the center line of the sample, as expected in SRIM calculations. (b): Simulated vacancy concentration after overlapping positron implantation profile from 16 keV positrons. Slices again taken at 10, 100, 200, and 400 nm. Damage still increases as depth increases along the center line of the sample, but less vacancies are observed by positrons than calculated by SRIM, seen in Figure 5.4a.

Finally, overlaying the expected vacancy concentration and positron implantation profile (Figure 5.3b) yields the observed vacancy concentration from monovacancy-sampling positrons, the expected results of an in-situ experiment accounting for the sampling efficiency and positron vacancy interaction as outlined above. The positron implantation profile used in the Figure 5.3b was for 16 keV positrons. The decrease in observed vacancy concentration in Figure 5.3b versus the calculated vacancy concentration in Figure 5.3a is due to the fact not all monovacancies will be sampled by incoming positrons. The model used does not include diffusion of positrons after implantation, and positrons may in fact sample more vacancies during diffusion than calculated here. However, the same trend of increasing vacancy concentration from 0 – 400 nm along the centerline can be seen.

The total observed vacancy concentration inside the sample is calculated by summing over vacancy concentration in all sample voxels. The simulation ran for 3 cases, one with the ion beam off, and the other two with the ion beam on at different beam currents. The observed vacancy concentration at different depths was calculated for each case by varying the incident positron energy from 2 to 16 keV. Increasing positron energy increases the mean implantation depth, sending more positrons to sample deeper into the material [12,13]. With the ion beam off, the observed concentration was small, $9.1 \cdot 10^{-33}$, and constant from 2-16 keV. Only thermal monovacancies at room temperature were present in the sample without the monovacancies from radiation damage. Turning on the ion beam drastically increased the observed vacancy concentration inside the sample to 10^{-4} -10^{-3} range. In agreement with rate theory [4], at low temperatures, the effect of thermal vacancies was determined to be negligible.

Simulated vacancy concentrations as a function of incoming positron energy for the two cases with the ion beam on are plotted in Figure 5.5. A trend of increasing vacancy concentration as a function of depth matches the SRIM damage cascade results in Figure 5.4, which is in good agreement with the 2 MeV damage simulations. Simulating the same experiment for a higher dpa case (an order of magnitude greater beam current) yields an increase in vacancy concentration, and the increase in vacancy concentration at higher depths inside the sample means the peak in the damage cascade around 500 nm becomes more pronounced. The vacancy concentration increases significantly when irradiated to 0.06 (high) dpa as compared to the defect concentration when the dose was decreased one order of magnitude to 0.006 (low) dpa. A future in-situ experimental setup could cycle the ion beam off after some time and measure the decay of the radiation damage monovacancies.

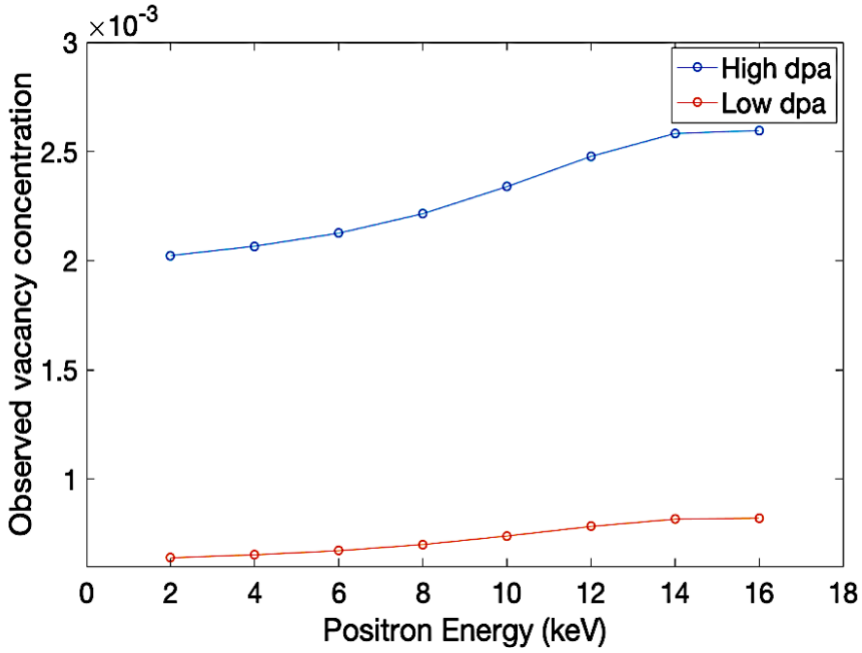

Figure 5.4: MATLAB simulated positron-observable monovacancy concentration as a function of dose, obtained by varying the incident sampling positron energy from 2-16 keV.

There are limits to the positron implantation and damage cascade simulation techniques used here. Positrons diffuse back to the surface and can form positronium, relevant for positron energies below 2 keV [14]. Second, the damage cascade simulates dpa rate, but only the formation of monovacancies without other extended defects such as divacancies, large vacancy clusters, or dislocation loops. Extended defects were not modelled in the PAS simulations here that are seen in previous ex-situ TEM results [15, 16] after the damage cascade. Even in the simulated high dpa case, the saturation limit of positron trapping may even be reached (about $1 \cdot 10^{-3}$), and in saturation positrons only detect the defect type with highest positron trapping rate. Future investigations should focus on resolving different trapping sites with PAS.

Despite these limits, the in-situ computational model in this work shows the effectiveness of PAS in capturing small vacancies associated with ion irradiation. The pulsed, variable energy positron beam allows one to use positrons for in-situ ion irradiated samples, a new ability in providing quantitative description for their density even in the case of positron trapping at monovacancies. Monovacancies are among the smallest defects, too small to observe with TEM, but are the embryos for larger vacancy clusters, dislocation loops, and voids. Observing increases in monovacancy concentration from the damage cascade offers new insights on the fundamental evolution and growth of larger defects. Positron spectroscopy is promising, non-destructive tool for the investigation of the damage cascade in-situ, and its effectiveness can even be seen when compared to ex-situ PAS of larger defects after the end of the damage cascade.

The promise of the in-situ technique for coincident ion irradiation and PAS is to directly observe the damage cascade in a way not previously possible. Studying the fundamental Frenkel-pair creation for vacancies in radiation damage is highly important and has been modelled in this work, but the full validation of standard rate theory cannot be entirely investigated without combining simultaneous PAS and ion irradiation in-situ experimentally. Monovacancy creation during ion irradiation, survival rate after radiation, and agglomeration of vacancies to extended defects can be studied by further developing the PALS and DBS techniques demonstrated here.

5.1.4 Conclusion

This theory and simulation result shows the effectiveness of PAS both in capturing small monovacancies associated with ion irradiation and in providing quantitative description for their size and density even in the case of saturated positron trapping at defects. Pulsed, variable energy positron beams allow for nondestructive investigations of radiation damage featuring small defects. Combining ion-irradiation and PAS techniques experimentally uniquely should allow one to probe the size and distribution of small defects as a function of dose in-situ.

Monovacancy concentration was shown in MATLAB simulation to increase in-situ with increasing dpa; however, surviving monovacancies ex-situ may not directly be detected as Fe monovacancies are unstable and often highly mobile unless trapped at impurities. The promise of using PAS techniques for additional in-situ studies for probing monovacancies and evolution of extended defects is demonstrated here because monovacancies are too small for ex-situ TEM

studies and unstable outside of the radiation damage cascade. Investigating monovacancy evolution in-situ is highly important, because they are embryos for larger, stable extended defects during and after irradiation such as vacancy clusters or voids.

5.2 Experimental PAS study of non-equilibrium radiation point defects in Si

5.2.1 Introduction to the importance of PAS for non-equilibrium radiation point defects in Si

Studies observe extended effects of radiation damage, but do not directly observe understanding the non-equilibrium defects from the damage cascade which drives the development of extended effects. The survival of defects is a dynamic problem, so experimental verification of either the displacement damage or its evolution has proven to be difficult. In-situ techniques must be employed to experimentally quantify and verify the evolution of the damage cascade. While experimental facilities with monoenergetic positron beams are limited, previous studies have demonstrated the usefulness of ex-situ VEPAS for studying surviving vacancy-type defects in ion-implanted and irradiated materials. [17]. Section 5.1 sought evidence that in-situ PAS investigation of defect evolution was indeed feasible. Section 5.2 is an experimental study of in-situ VEPAS during ion irradiation featuring 5 keV He^+ in silicon.

Silicon was chosen because it's defect dynamics at low doses are well-studied, mostly due to prolific use of ion implantation in the semiconductor industry. In addition, silicon wafers provide readily available defect free substrates for investigating contrasts with ion-induced defects. Ion implantation is one of the most important processing tools in Si integrated circuit technology, especially for dopant ions. The passage of an energetic ion (e.g., a dopant ion) through the Si lattice initiates a sequence of displacement events that leads to defect production and, at sufficiently high doses, to the crystal-to-amorphous (c-a) transformation of the irradiated area. This transformation is critically dependent on the irradiation parameters [18] and is controlled by a competition between damage accumulation and dynamic annealing. [1-3] The mass of the irradiating ion species, [18,19] the temperature of the substrate, [1,3] and the dose [1,20] and dose rate [1-3] of the irradiation all play an interdependent role. There are several experimental and simulation studies on the amorphization of Si after ion implantation, but mainly focused on investigating the surviving defects after the damage cascade or determining a phase transformation [21-23]. This experiment probes the evolution of ion implantation defects during the damage cascade, in-situ, which are ultimately responsible for the surviving defects so often under investigation.

5.2.2 Methods and sample preparation used to study non-equilibrium radiation point defects in Si

Commercially available n-type Si wafer defect free crystals were used to increase the contrast between defects induced via ion irradiation. VEPAS measurements were performed at the positron facility in the Helmholtz-Zentrum Dresden-Rossendorf (HZDR) in Dresden, Germany. Doppler broadening variable energy positron annihilation spectroscopy (DBS) measurements have been conducted at the apparatus for in-situ defect analysis (AIDA) [9, 10, 11] of the slow

positron beamline (SPONSOR) [9]. Positrons were implanted into each sample with discrete kinetic energies E_p in the range between 0.05 and 10 keV, which allows for depth profiling from the surface down to about 650 nm. Before performing any experiments with the ion beam, a characterization of the bulk Si was done with VEPAS, using positron energies from 0.5 – 10 keV. These results were compared after the beam cycling experiment and subsequent sample exposure to oxidation to characterize overall changes in sample structure during the experiment. A schematic of the experimental setup is given in Figure 5.5.

In order to measure the non-equilibrium vacancy defect survival, VEPAS was performed before and during ion irradiation for 30-minute intervals. This irradiation-measurement iteration pattern was performed 3 times to allow for relaxation of non-equilibrium defects. The objective was to observe how the open-volume defects from radiation damage change the S-parameter during and after ion irradiation. Depth-resolved positron measurements were taken for 30-minute intervals at E_p=2.45 keV (about 200 kcnts at 511 keV peak) before (b_i) and during (d_i) Si irradiation, where i is the irradiation iteration step. The ion irradiation implanted 5 keV He^+ with I_{ion} = 100 nA. 3 irradiation steps were performed. After the last irradiation, a DB-PAS measurement was taken at E_p=2.45 keV, labeled "after" (a).

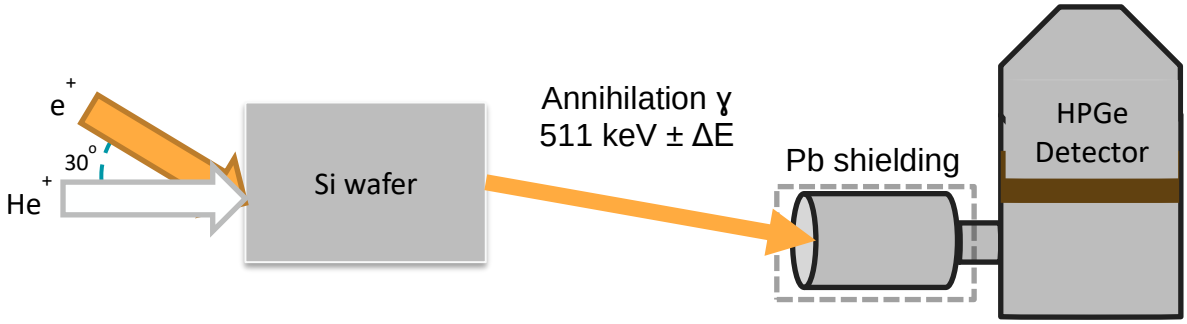

Figure 5.5: Schematic of the experimental setup featuring coincident ion and positron beams with HPGe detector.

Thermalized positrons have very small momentum compared to the electrons upon annihilation, a broadening of the 511 keV line is observed mostly due to momentum of the electrons, which is measured with one or two high-purity Ge detectors (energy resolution of 1.09 ± 0.01 keV at 511 keV). This broadening is characterized by two distinct parameters S and W defined as a fraction of the annihilation line in the middle (511 ± 0.70 keV) and outer regions (508.56 ± 0.30 keV and 513.44 ± 0.30 keV), respectively.

The He^+ ion gun used for irradiation was a Kaufman type with defocused beam area to about 5 mm beam diameter and the ion current up to 1 mA. The highest ion implantation energy available was used, 5 keV, in order to drive the ions as deep into the sample as possible as to minimize surface effects. The positron implantation energy was chosen to be at the maximum of the ion

implantation depth. Unfortunately, as of today no higher energy ion source is available at the positron facility.

Ideally, all implanted positrons would sample defects created by incoming ions, so both the ion and positron implantation profiles were simulated to find maximum overlap. The ion implantation depth profile was simulated using SRIM [6]. The beam fluence to damage conversion is based on SRIM Monte Carlo code simulations using the K-P mode with a displacement threshold energy of 40 eV for all the elements involved. The Mahkov positron implantation profile was simulated for positron energies (E_p) from 2.45 keV in Si. Figure 5.6 shows the overlapped ion and positron implantation profiles. A small maximum at $E_p \approx 3$ keV was found after irradiation overlaps with ion damage distribution, so $E_p = 2.45$ keV was chosen for the in-situ measurements, as seen in Figure 5.6.

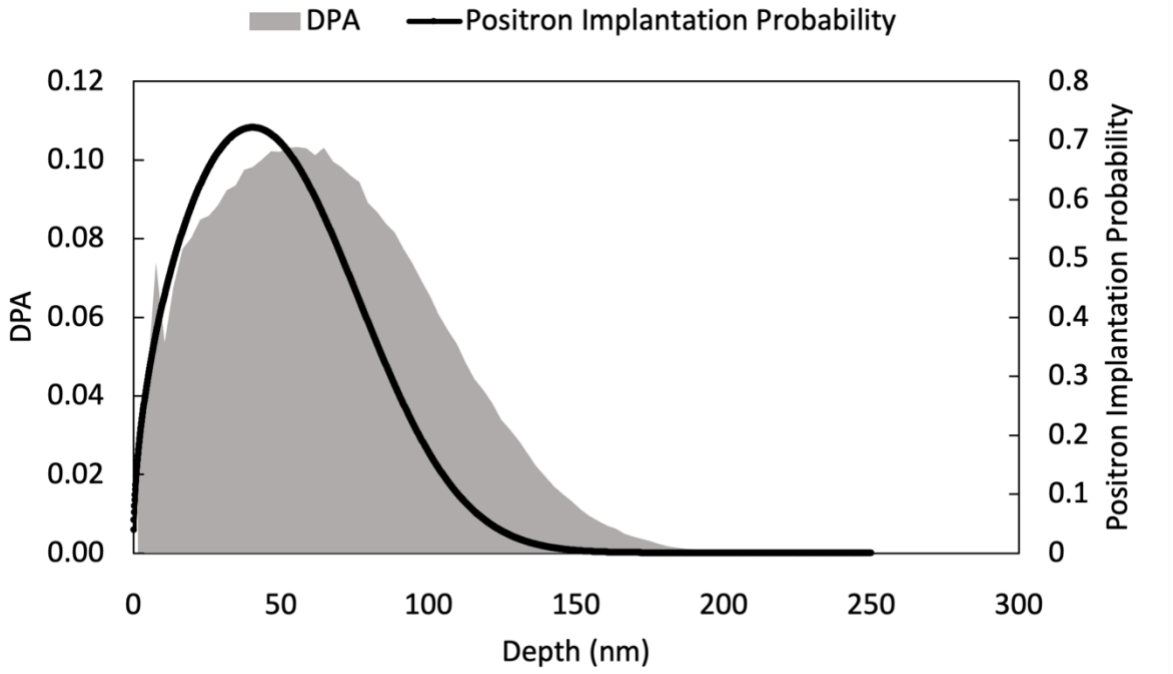

Figure 5.6: Ion implantation damage profile calculated from SRIM (shaded in gray) and positron implantation profile at 2.45 keV (black). The maximum overlap between positron implantation and ion damage was found at $E_p = 2.45$ keV, which determined the positron energy for the in-situ measurements.

After in-situ DBS, variable energy positron annihilation lifetime spectroscopy (PALS) measurements were conducted on two Si samples at the Mono-energetic Positron Source (MePS) beamline at HZDR, Germany [9, 10, 11]: one pristine and the post-irradiation Si sample. The MePS beamline is the end station of the radiation source ELBE, (Electron Linac for beams with high Brilliance and low Emittance) at HZDR (Germany) [10, 11] featuring a digital lifetime $CrBr_3$ scintillator detector 51 mm diameter (2”) and 25.4 mm length (1”) coupled to a Hamamatsu

R13089-100 PMT with a μ-metal shield and housed inside a solid Au casing with a homemade software employing a SPDevices ADQ14DC-2X with 14 bit vertical resolution and 2GS/s horizontal resolution and with a time resolution function down to about 0.205 ns. [24] The resolution function required for spectrum analysis uses two Gaussian functions with distinct intensities depending on the positron implantation energy, E_p, and appropriate relative shifts. All spectra contained at least 10^7 counts. For discussion on sources of uncertainty in data acquisition and analysis, please refer to the previous Section 4.1.1.

5.2.3 Results of PAS study of non-equilibrium radiation point defects in Si

DB-PAS measurements were recorded during each irradiation iteration step with the ion beam either on or off. The results are shown in Figure 5.7, featuring S-parameters from each 30-minute DBS VEPAS acquisition at E_p = 2.45 keV (about 200kcnts at 511 keV peak) before (b_i) and during (d_i) irradiation, where i, is the irradiation iteration step. The relative increase of S-parameter during irradiation steps suggests development of defects. Furthermore, monovacancies have been found to be unstable in Si, so the formation of more stable divacancies [25] was assumed, then further confirmed by PALS. The most important finding is the increased S-parameter values during each irradiation step with the ion beam on (d_i) compared to the measurements before an irradiation step (b_i) with the ion gun disabled, which visualizes most probably small fraction of non-equilibrium vacancies.

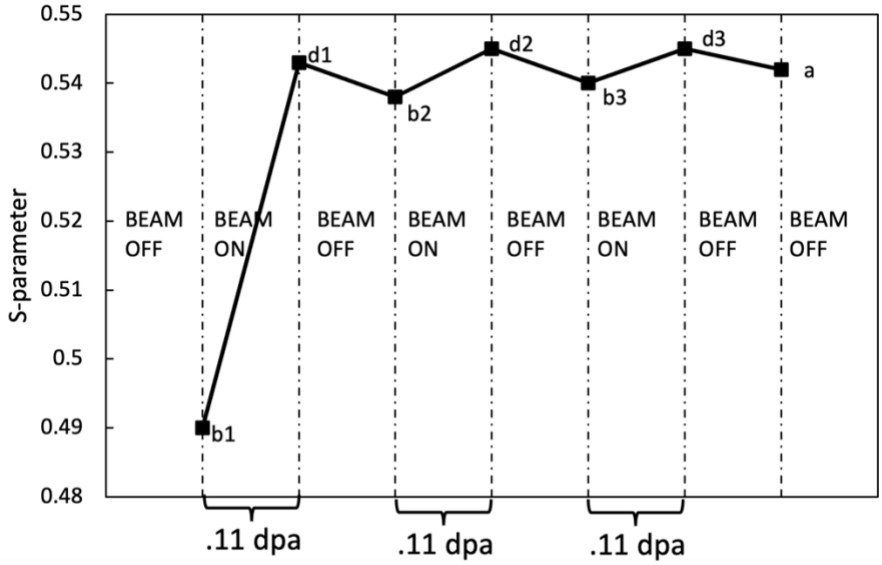

Figure 5.7: S-parameters from 30-minute DBS VEPAS acquisition at E_p=2.45keV (about 200kcnts at 511keV peak) before (b_i) and during (d_i), where i, is the irradiation iteration step. For all irradiation steps, I_{ion}=100nA.

Previous DBS measurements at E_p = 2.45 keV sampled the peak ion damage from irradiation, but other damaged regions in the sample were assessed with VEPAS after last irradiation iteration step i = 3. Figure 5.8 shows an increase in S-parameter after irradiation was seen at each positron

energy from 0.5 – 10 keV. For comparison in the following discussion, the S-parameter values in Figure 5.8 have been normalized to the bulk S-parameter value (S_B) for bulk silicon.

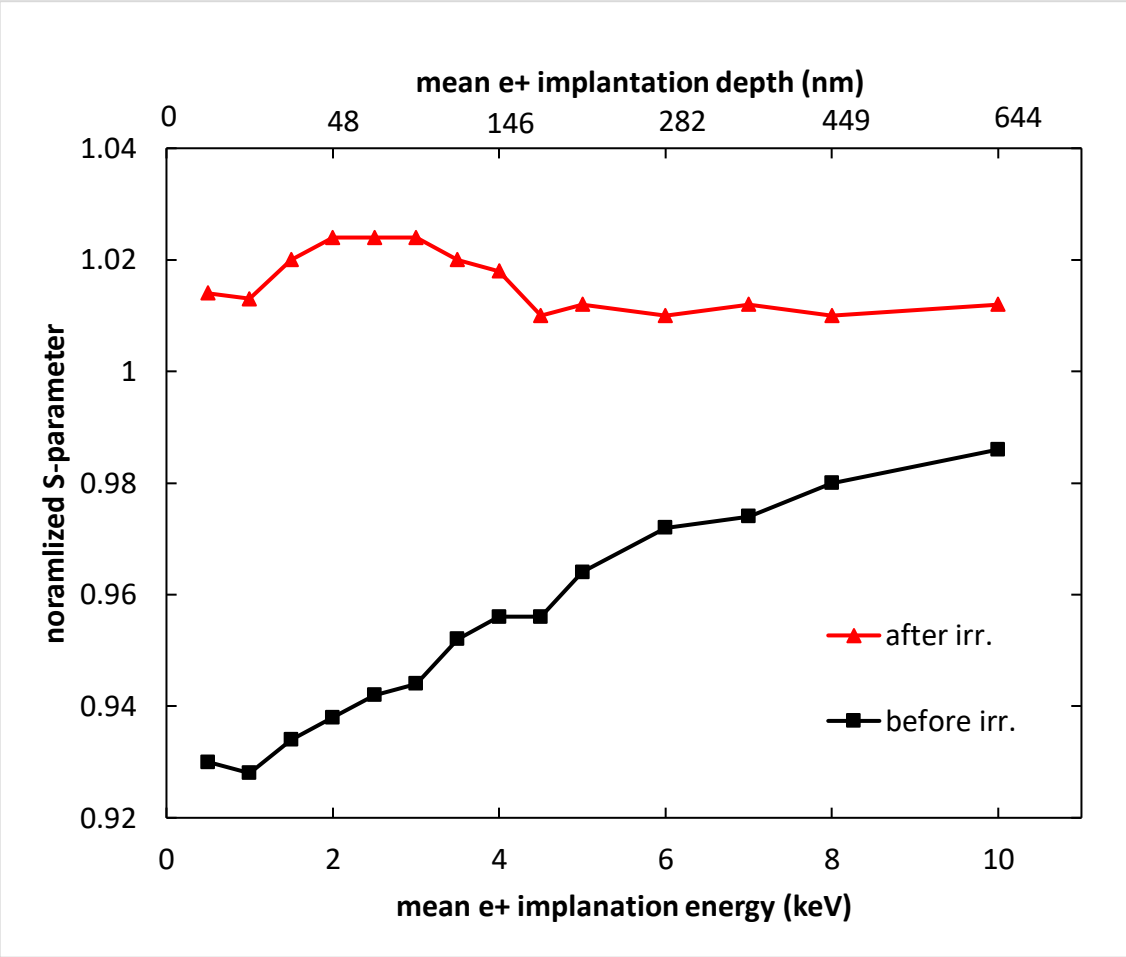

Figure 5.8: DBS measurements before (black squares) irradiation and after the last irradiation iteration step i=3 (red circles). The measurements used a range of positron energies from 0.5 – 10 keV, and the expected depth from the sample surface sampled is shown as well. The S-parameter values have been normalized to the bulk S-parameter value for silicon.

For PALS analysis, a typical lifetime spectrum N(t) is again described by Equation 2.11:

$$N(t) = \sum \left(\frac{1}{\tau_i}\right) \mathrm{I_i} \exp\left(-\frac{t}{\tau_i}\right) \tag{2.11}$$

where τ_i and I_i are the positron lifetime and intensity of the i-th component, respectively (ΣI_i=1). All the spectra were deconvoluted using the non-linearly least-squared based package PALSfit fitting software [8] into few discrete lifetime components, which directly evidence few different defect types (sizes) [see Figure 5.9]. The corresponding relative intensities reflect to a large extend concentration of each defect type (size). In general, positron lifetime is directly proportional to defects size, i.e., the larger is the open volume, the lower is the probability and longer it takes for positrons to be annihilated with electrons [12, 13, 14]. Positron lifetimes and

intensities were measured as a function of positron implantation energy, E_p, or mean implantation depth, $\langle z \rangle$.

[a] [b]

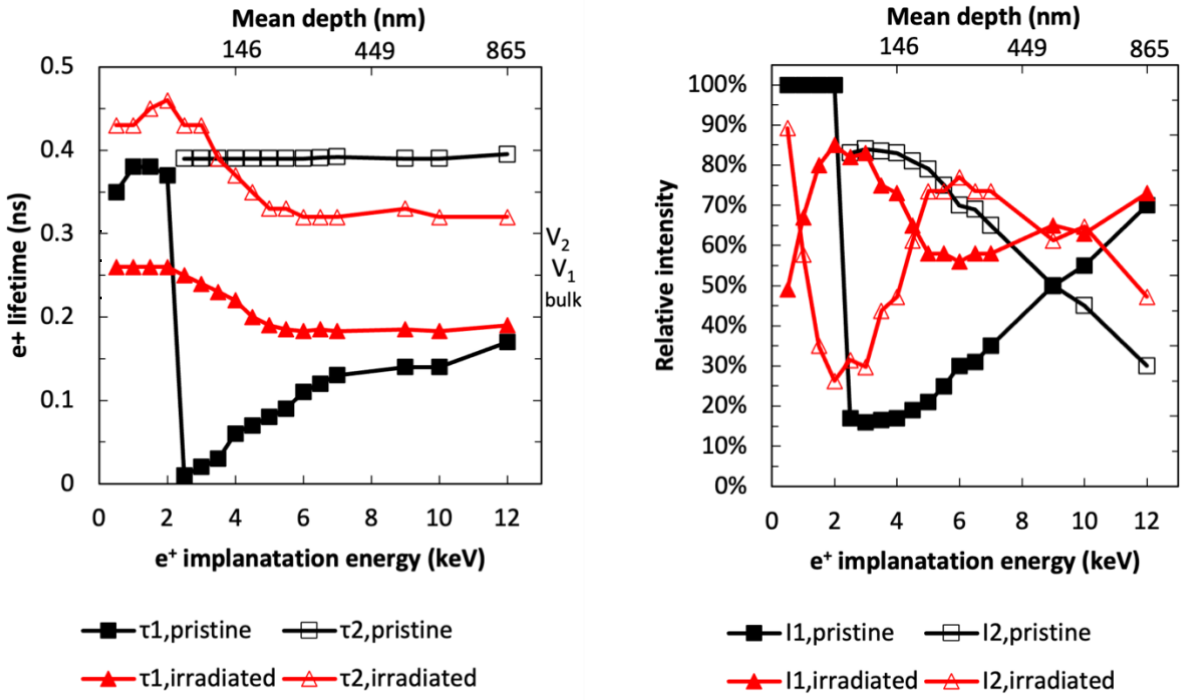

Figure 5.9: PALS analysis for pristine (closed symbols) and He^+ irradiated (open symbols) Si substrate. [a] The first τ_1 (squares) and the second τ_2 (circles) lifetime component as a function of positron implantation energy and mean positron implantation depth, <z> as well as [b] the lifetime components' relative intensities I_1 and I_2, respectively.

From PALS results in Figure 5.9, the first 40-50 nm region of the pristine sample is dominated by larger vacancy clusters (>5 vacancies [27]), since only a single lifetime component is detected, $\tau_1 \approx 385$ ps ($I_1 \approx 99$ %). This region likely consists of amorphous native SiO_2. In the deeper parts of the sample, two lifetime components have been detected, where τ_1 is the so-called reduced one and τ_2 represents a defect component. In this case, the defect component originates in fact from the oxide layer, because of a long Si positron diffusion length. Hence, implanted positrons can experience partial back diffusion to the surface. It is visible by monotonic change of relative intensities: the deeper the implantation, the more (less) intense is the first (second) component. Within the measured range, no full bulk annihilation was achieved. After irradiation, the 40-50 nm depth region is changed completely. The vacancy cluster size increases ($\tau_2 > 400$ ps; vacancy clustering), and a large number of most likely monovacancies (V_1 in Figure 5.9) is introduced $\tau_1 \approx 262$ ps [28]. It is possible that the oxide layer still exists, but it is likely much thinner. The profiles of relative intensities resemble the ion damage profile, especially the τ_2 profile. Deeper in the irradiated sample, a signature of divacancies (V_2) or slightly larger defects is found [27]. This

divacancy signature found in PALS agrees directly with the DBS results in which divacancies are also observed as the major defect fraction.

5.2.4 Discussion of PAS study of non-equilibrium radiation point defects in Si

Even though the incoming positrons only sample a small fraction of defects in the material, the difference in defects present with the ion beam off (b_i) versus on (d_i) is detectable and measurable, as seen in Figure 5.7. In addition to the increase in S-parameter after each irradiation, the difference in S-parameter between beam on/off seems to decrease with each iteration step, suggesting buildup of defects in the Si-bulk. This apparent defect buildup brought concerns of Si amorphization, that is, the additional dose received might have affected the underlying Si bulk crystal structure.

Note the dose per 30-minute irradiation is $9.8*10^{14}$ ions/cm^2. Figure 5.7 shows the S-parameters of each irradiation step as a function of dpa delivered, but the total dose delivered to the sample is an order of magnitude less than the figure cited by molecular dynamics study as the threshold for Si amorphization at $8*10^{16}$ ions/cm^2. [29]. An experimental Si amorphization study also suggests expecting limited amorphization because of recombination of point defects and surface annihilation from doses with light ions at low energies. [29-32] From SRIM, this incoming dose can be used to calculate overall dpa level. From each 30-minute irradiation, about 0.11 dpa was calculated to be expected.

Considering the existing DFT calculations (local-density approximation scheme with the Boronski and Nieminen enhancement) [28] of defect states in Si a change of the S-parameter with respect to its bulk value (S_B) corresponding to a monovacancy is $S/S_B \approx 1.018$. For a divacancy $S/S_B \approx 1.045$ is expected. The final in-situ S value after irradiation from the experiment lays between these two defect states indicating that the maximum cluster size is divacancy. In addition, the PALS divacancy signature agrees directly with the DBS results in which divacancies are also observed as the major defect fraction.

This study was limited to in-situ DBS due to the fact that the in-situ capability is only available at HZDR today, which can only measure relative changes in defect concentration, as opposed to PALS, which can quantify absolute changes. Future experiments should investigate the changes in absolute non-equilibrium defect population under irradiation and annealing. In-situ investigation under combination of extreme environments will promote understanding of non-equilibrium defect contribution to extended deformation effects of materials under corrosion, pressure, or stress.

The study was also limited by the range of ion implantation (peak range of approximately 100 nm) due to experimental limitations. Shallow ion implantations complicate analysis because of surface effects that are present within 100 nm, especially the positron implantation distribution superimposed with at least partial back diffusion of positrons to the surface. In the future, deeper ion implantations must be performed in order to combat the effect of diffusion and formation of positronium or other surface effects.

5.2.5 Conclusion

The effect of non-equilibrium defects from radiation damage in Si was investigated by in-situ depth-resolved DBS measurements during ion irradiation. Cycling the ion beam on and off allowed for investigation of non-equilibrium defect population during and after irradiation with positron spectroscopy. Significant increases in the defect population were observed as S-parameter values during irradiation (ion beam ON) were higher compared to after irradiation with the ion gun disabled (OFF), which indicates the presence of small fraction of non-equilibrium vacancies. The decreases in S-parameter after turning the ion beam off highlighted the importance of in-situ measurements for capturing relaxation of the non-equilibrium vacancies induced by irradiation.

From the absolute S-parameter increase the defect states were evaluated as mixture of mono- and bi-vacancies. Shallow ion implantation and DBS measurements limited this study to relative investigation of defect population, but in the future, in-situ PALS with irradiation could quantify true defect populations of non-equilibrium vacancies. Further in-situ studies are needed to understand the true defect concentration of materials during irradiation, as that will drive the materials' response in a number of contexts, including irradiation environments with added corrosion, pressure, or stress.

At the time of writing, only Los Alamos's Ion Beam Materials Laboratory and Dresden's HZDR facility are completing construction and testing of in-situ PAS beamlines, with schematics shown in Figures 5.10 and 5.11. Their designs feature coincident ion and positron beam in which positrons are incident on a sample that is simultaneously bombarded with an ion beam, providing non-destructive quantification of non-equilibrium and transient defects as they are produced. The experimental capabilities of these facilities needs to be expanded upon in order to verify theory, measurements, and simulations of the radiation damage cascade.

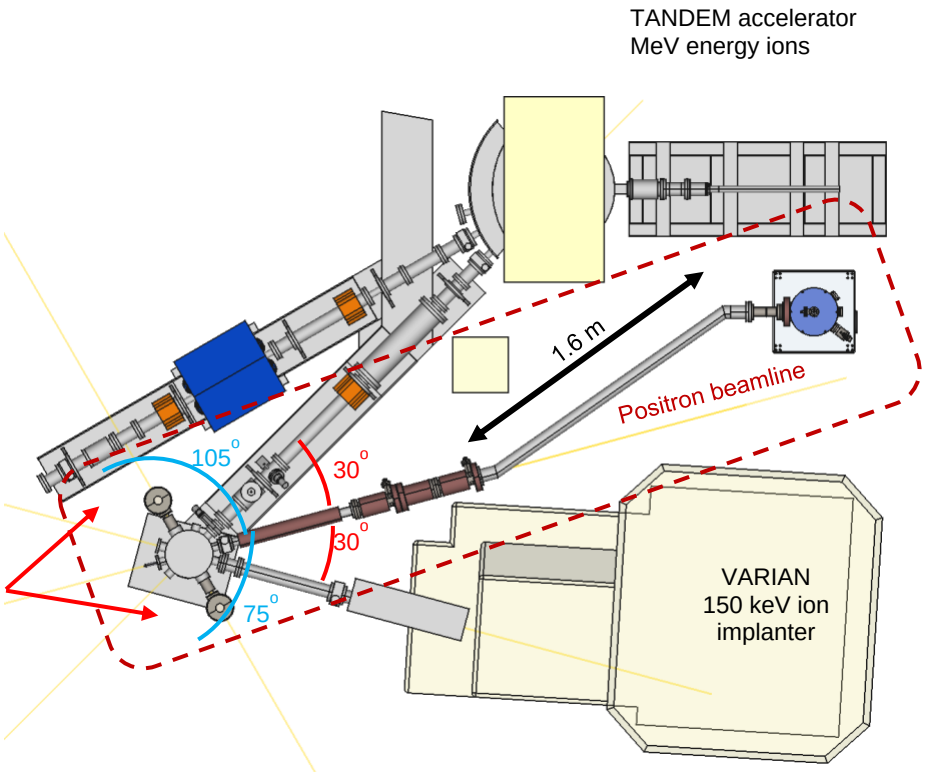

Figure 5.10: Los Alamos in-situ positron annihilation spectroscopy (iPAS) beamline built featuring the VARIAN and TANDEM ion accelerators. The final design will have 3 beams converging on a single target chamber. [33]

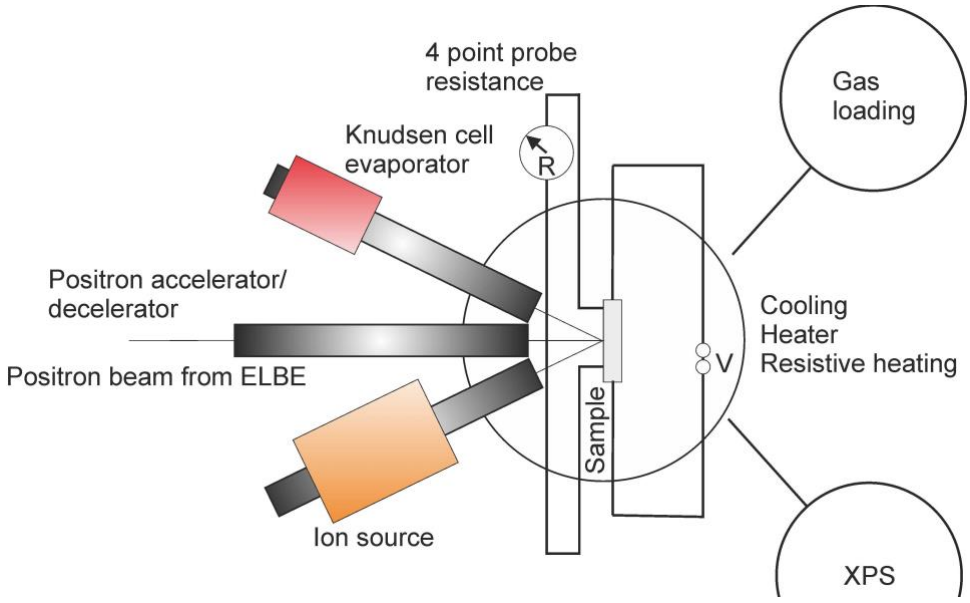

Figure 5.11: HZDR in-situ positron annihilation spectroscopy beamline under construction featuring an ion source with a 4-point resistance probe (for resistivity measurements). [34]

6. Discussion

6.1 Impact

To date, most studies used ex-situ testing methods to evaluate defects, which limited understanding of the nonequilibrium defects present during irradiation. Chapter 2 reviewed the current understanding of radiation-induced and oxidation-driven defects, which concluded that ex-situ experiments lack a direct relationship to the damage cascade from irradiation and rarely investigate fundamental point defects. This prevents truly predictive modelling and informed decision-making for material design in nuclear environments. In recent years, efforts have been made to analyze defect formation in-situ, allowing for direct, nondestructive observation of atomic-scale, short-lived nonequilibrium defects via PAS. The work in this dissertation looked comprehensively at the small, vacancy-type point defects responsible for radiation damage effects in different reactor environments. As for oxides defects, other modelling and experimental techniques have tried to capture defect behavior during oxidation, but experimental verification of small point defect behavior remained elusive. This dissertation also looked comprehensively to identify oxidation defects which are responsible ultimately for controlling the rate of corrosion in nuclear structural materials. A summary of the experimental and modelling efforts on point defects in this dissertation is described below.

6.1.1 Rate Theory

First, combining rate theory and PAS simulation allowed for observation of small monovacancies associated with ion irradiation. Monovacancy concentration was shown in simulation to increase in-situ with increasing dpa; however, surviving monovacancies ex-situ are difficult to detect. In MATLAB [1], the simulation combined in-situ Fe^{2+} ion beam irradiation and positron annihilation spectroscopy on pure Fe with Wiedersich rate theory [2] and a K-P model [3] of radiation damage in SRIM [4]. The nonequilibrium monovacancy defects were simulated to be observable with PALS, and in-situ vacancy concentration showed an increase with increasing dpa. Furthermore, a follow-up ex-situ PAS experiment on irradiated Fe confirmed the instability of monovacancies outside the damage cascade. Irradiation of single crystal and polycrystal Fe revealed only a small fraction of surviving monovacancies ex-situ. The two defect lifetimes measured after irradiation corresponded to large vacancy clusters and another lifetime component in between the bulk and monovacancy concentration – but close to the dislocation lifetime [5,6]. This confirmed the instability of the Fe monovacancy outside of the damage cascade, and how these vacancies do coalesce to form rather large vacancy clusters (> 15 vacancies) in Fe [6]. These two studies together started to probe at rate theory considerations, but an in-situ experiment was still necessary to probe the damage cascade and rate theory predictions directly.

The ion beam cycling experiment was the most direct test of rate theory considerations among the work presented in this dissertation. Cycling ion beam irradiation onto a silicon wafer led to detectable changes in positron trapping signal. Significant increases in the defect population were observed as S-parameter values during irradiation (ion beam ON) were higher compared to

after irradiation with the ion gun disabled (OFF), which indicates the presence of small fraction of non-equilibrium vacancies. This experiment confirmed two things. First, nonequilibrium defects present during a radiation cascade should be measurable and detectable with PAS. This is in line with previous experiments by Iwai and Tsuchida et al. on in-situ ion beam irradiation in Ni. [7] The investigation showed these nonequilibrium vacancies are indeed unstable, and they could be annihilated at strong defect sinks such as grain boundaries or via recombination with freely migrating interstitials during irradiation. Second, rate theory predications of nonequilibrium defect population can also be tested with PAS. However, the type of positron spectroscopy used in the study, Doppler-broadening, does not allow for quantitative measurements of the absolute defect concentration. Lifetime spectroscopy needs to be utilized as a measurement tool in order to directly make comparisons to or verify rate theory.

6.1.2 Oxidation

Defect behavior during irradiation and corrosion was also investigated on structural nuclear reactor materials with PAS, namely Fe and Cr, albeit ex-situ. The second aspect of this dissertation was to expand the capability of PAS to study nuclear material structural oxides. Doppler broadening spectroscopy can be developed to infer overall vacancy-type defect concentrations from oxidation. PAS is extremely helpful when investigating irradiated oxides, especially in isolating the effect of oxidation versus irradiation on vacancy-defect population. In this way, novel PALS observations of aged oxide layers were developed to measure predominant defect types and defect dynamics from irradiation on oxidized materials. While this dissertation references prior knowledge about oxide layers from literature electrochemical studies of semiconductors, this work is primarily focused on point defect behavior during oxide growth, not the corrosion mechanism or defect transport within different layers of the oxide.

Chapter 5 showcases the usefulness of PAS characterization to evaluate defects' evolution during growth of Cr and Fe oxide layers. Combining defect analysis from positron annihilation spectroscopy with electrochemical techniques such as Mott-Schottky analysis allows a comprehensive view on the defects in thermally grown oxides.

In chromium, it was found that, while the oxide layer grown in air at 700°C increases in thickness as a function of oxidation time, the defect density is greatly reduced. Figure 6.1 shows the Cr-oxide growth process and the vacancy clusters. PAS observed lower defect densities in 5 days air oxidized chromium than in the 24-hour sample, indicating annealing of defects in the oxide layer as the oxide layer grows.

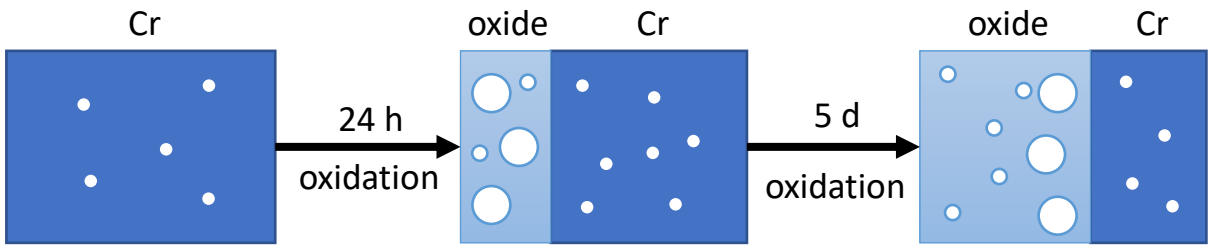

Figure 6.1: Schematic of Cr-oxide layer growth and large oxide defects annealing over time.

By interpreting PAS results with prior electrochemistry results, the most likely predominant defects were identified as oxygen interstitials or chromium vacancy cluster complexes. This confirms the growth process for Cr_2O_3 is dependent on the transport of oxygen interstitials and chromium vacancy clusters. This is important because chromium is a major alloying element in stainless steel, often utilized for its passivating oxide layer's corrosion protection. The identify and nature of predominant point defects in Cr_2O_3 has been debated for decades in contrasting results from theory, modelling, and experiment efforts. This effort sought to shed light on the nature of vacancy-type defects with PAS and is supported by other previous electrochemical efforts [8-13] and MD simulations of point defect migration energies [14-17].

In Fe-oxide, the nature of point defects is more complicated than chromium oxide because of the stoichiometric and microstructural differences in the Fe-oxide series, relative to single phase, corundum structure Cr_2O_3. Again, the basic oxide structure is important to passivity, the defects inside the oxide films also play a critical role for its protective properties [18, 19].

Two major variables were tested for oxide defect behavior: oxidation temperature and oxidation time. Different oxidation temperatures result in different oxides, as well as overall differences in positron trapping behavior. Oxidation at 400°C yields mainly Fe_3O_4, but 600°C and 800°C yield mixed oxides with α-Fe_2O_3/FeO/Fe_3O_4. [20, 21] On the other hand, oxidation time increases show a consistent decrease in defects, measured in decreases in the S-parameter and average positron lifetime. This suggests the annealing of large defects from older oxide layers, as shown in Figure 6.2 below.

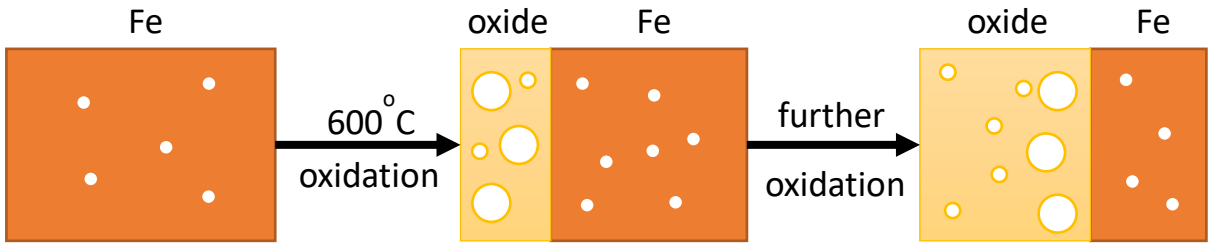

Figure 6.2: Schematic of Fe-oxide layer growth and large oxide defects annealing over time. Oxides were grown in air at 600°C.

There is a pronounced increase in S-parameter (and defect level) in the sample at the Fe_3O_4/Fe metal-oxide interface in the irradiated 400°C oxide. Thus, it is very likely that vacancies may accumulate at metal/oxide interface, but this requires further corroboration by other techniques, such as TEM and APT.

In addition, irradiated oxides allowed for investigation of the coupled effects of irradiation and oxidation. The coupled impacts of irradiation and oxidation are directly relevant to the coupled

radiation and oxidizing environments experienced by nuclear reactor materials. Overall, PAS suggests that 0.06 dpa proton irradiation at room temperature increases the average vacancy concentration for all irradiated materials. Furthermore, the rise in vacancy concentration for the irradiated oxides may be partially related to the accumulation of vacancies at the metal/oxide interface. Irradiation also has an impact on the defect sizes in the oxide. At lower temperatures 400°C, irradiation reduced the size of vacancy clusters, whereas an opposite effect was observed at 600°C and 800°C with evidence on the formation of vacancy clusters. This suggests it may be easier to form vacancy clusters from irradiation depending on the grown oxide. At the same irradiation level, Fe_3O_4 vacancy clusters in 400°C form less readily than Fe_3O_4 vacancy clusters at 600°C and Fe_2O_3 vacancy clusters in 800°C. This is shown in a comparison schematic in Figure 6.3.

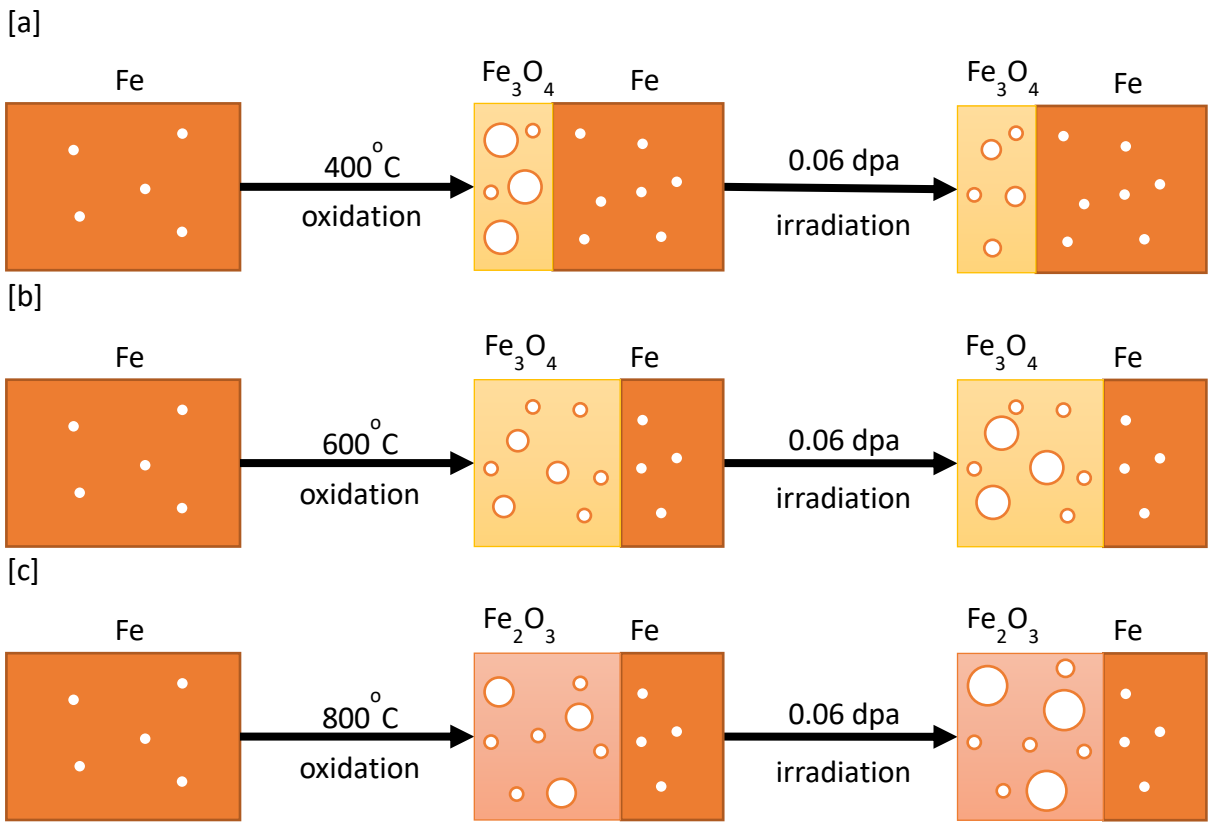

Figure 6.3: Schematic of Fe-oxide layer defects after irradiation at different temperatures. At 400°C, irradiation reduced the size of vacancy clusters; whereas an opposite effect was observed at 600°C and 800°C with evidence on the formation of vacancy clusters.

Oxide defects are primarily determined by which oxide is grown at what temperature, because as the oxide grows thicker with time and closer to thermal equilibrium, there are not large changes in relative defect concentration. The main effect of ageing oxides is the stabilizing of defect sizes. However, irradiation seems to dominate thermal oxide defects, introducing an overall number of nonequilibrium defects that then dominate and stabilize within the oxide. This suggests it may be easier to form persistent, surviving vacancy clusters from oxide irradiation nonequilibrium defects rather than metal/oxide interface nonequilibrium defects.

6.1.3 Conclusion

Radiation damage induces a state in matter that is far from equilibrium. The addition of corrosion increases the complexity of the nonequilibrium problem. Chemical species from corrosion couple with defects produced under irradiation, leading to different microstructural responses from the multitude of competing transport rates from nonequilibrium defects in the material. Thus, there is a continual need to advance understanding of these coupled effects to ultimately predict material response and enable the design of new materials that can better withstand these combined extreme conditions. The work in this dissertation advances toward a predictive understanding for how point defect transport can drive radiation damage and corrosion.

Positron spectroscopy is a useful tool to probe the size and distribution of small defects as a function of dose or oxidizing environment, and consequently, PAS was chosen as the primary investigative tool in this dissertation. PAS can detect monovacancies that are too small for ex-situ TEM studies and unstable outside of the radiation damage cascade. Investigating monovacancy evolution in-situ is highly important, because they are embryos for larger, stable extended defects during and after irradiation such as vacancy clusters or voids. PAS can also investigate point defects as a complementary technique to electrochemical techniques or APT studies in oxides.

6.2 Gaps and Future Work

The experiments and discussion thus far have provided unique insight to defect studies on materials in reactor environments using PAS. However, there are still several ways for improvement and expansion of the resolved findings. The following list explores these considerations.

- All PALS results benefit from supporting modelling work to estimate lifetimes of investigated defect states. In order to fully characterize the defects under observation, it has been suggested before to develop an advanced trapping model and to create of a database of positron parameters. With an advanced model, one could consider extracting more quantitative information about the defect density and defect size in conventional and novel materials from previous PALS experiments. [22, 23]
- All test cases would also benefit from continued defect characterization. Alternative methods such as TEM, Raman spectroscopy, and XRD could be useful to further quantify larger extended defects. Additionally, in-situ TEM [24] can be employed to replicate the efforts of in-situ PAS and quantify the evolution of larger defect populations, including not just dislocations and vacancy-type defects.
- In systems in which the predominant point defect population is positively charged or driven by interstitials, PAS is a limited investigation technique. For example, models of oxide growth in nuclear materials have centered on anion/cation mobility. In complex environments like these featuring interstitials or cations, PAS may only provide supporting evidence rather than a deciding argument on which point defect population drives film growth. [22, 23]

- There is significant opportunity for the advancement and expansion of PAS methods to other composite and alloy systems as well as varying environmental conditions. The work in this dissertation was limited to simple oxides, but future work could consider investigating point defects in Fe-based alloys such as steels. As for environmental conditions, In-situ PAS measurements during combined irradiation corrosion conditions (simulating the coupled conditions in a reactor environment) can reveal the combined effect of irradiation/corrosion on the material microstructure on an atomic scale that cannot be obtained from even current in-situ TEM investigations.
- To further improve the time scale of in-situ measurements, it is critical to develop positron facilities with higher beam intensities to enable data collection on the nanosecond time scale and develop in-situ measurements of atomic defects on nanoscale time scale. Advancing positron detection would also enhance the spectroscopy accuracy at determining defect type and behavior in nuclear materials research. For instance, further improvements in the timing resolution of PALS spectrometers would greatly advance PAS capability in defect sampling and characterization.
- Lastly, the development of more in-situ radiation damage positron facilities around the world would dramatically improve the understanding of the radiation damage cascade. At the time of writing, only Los Alamos's Ion Beam Materials Laboratory and Dresden's HZDR facility are completing construction and testing of in-situ PAS beamlines. Their designs feature coincident ion and positron beam in which positrons are incident on a sample that is simultaneously bombarded with an ion beam, providing non-destructive quantification of non-equilibrium and transient defects as they are produced. The experimental capabilities of these facilities need to be expanded upon in order to verify theory, measurements, and simulations of the radiation damage cascade.

7. Summary and Conclusion

Positron annihilation spectroscopy (PAS) techniques including both Doppler broadening spectroscopy (DBS) and positron annihilation lifetime spectroscopy (PALS) were employed to study irradiation and oxidation effect on vacancies point defects and vacancy clusters. PAS provides the ability to directly observe defects, nondestructively with great, versatile control of material parameters. The work in this dissertation features ex-situ PAS and in-situ irradiation PAS work, although the in-situ experiment was limited to DBS. For future work, it would be advantageous to expand the capability of in-situ PAS to utilize more quantitative defect characterization with PALS. Nevertheless, the work performed in this thesis contributes to the ever-growing applications of PAS for assessing nuclear engineering materials. The key findings are summarized as follows:

- With only one major oxide formed, Cr_2O_3, oxidation growth on chromium in air is suggested to be dependent on the transport of oxygen interstitials and chromium vacancy clusters. Cr_2O_3 oxide layer increases in thickness as a function of oxidation time, but the defect density is greatly reduced. (Chapter 4)
- Proton irradiation increases defect concentration in all oxides because irradiation introduces non-equilibrium defects into the oxides. (Chapter 4)
- Defects in an Fe-oxide layer are primarily determined by which oxide is grown at what temperature, because as the oxide grows thicker and closer to thermal equilibrium, there are not large changes in relative defect concentration. The main effect of ageing oxides is the stabilizing of defect size, as irradiation seems to dominate thermal oxide defects. (Chapter 4)
- Irradiation is known to create stable vacancy clusters in Fe, but grain boundaries prevent vacancy clusters from forming as monovacancies annihilate with existing grain boundaries. Grain boundaries prevent large vacancy clusters from forming in polycrystal Fe. (Chapter 4)
- Combining rate theory and PAS simulation allowed for observation of small monovacancies associated with ion irradiation. Monovacancy concentration was shown in simulation to increase in-situ with increasing dpa; however, surviving monovacancies ex-situ may not directly be detected as Fe monovacancies are unstable and often highly mobile unless trapped at impurities. (Chapter 5)
- Cycling the He^+ ion beam on and off allowed for investigation of non-equilibrium Si defect population during and after irradiation with positron spectroscopy. Significant increases in the defect population were observed as S-parameter values during irradiation (ion beam ON) were higher compared to after irradiation with the ion gun disabled (OFF), which indicates the presence of small fraction of non-equilibrium vacancies. (Chapter 5)

References

Introduction

[1] United States. (2022) *U.S. Energy Information Administration EIA*. Short Term Energy Outlook. United States. [Web Archive] Retrieved from the Library of Congress

[2] Fell, Gilbert, A., Jenkins, J. D., & Mildenberger, M. (2022). Nuclear power and renewable energy are both associated with national decarbonization. *Nature Energy*, *7*(1), 25–29. https://doi.org/10.1038/s41560-021-00964-w

[3] de Kirby, K., & Lovering, J (2021). A Socially Sustainable Future for Nuclear Energy in Emerging Markets. *The Breakthrough Institute: Oakland, CA, USA*.

[4] Rhodes, C. J. (2016). The 2015 Paris Climate Change Conference: COP21. *Science Progress (1916)*, *99*(1), 97–104. https://doi.org/10.3184/003685016X14528569315192

[5] World Nuclear Association (2022). World Nuclear Performance Report 2022 *World Nuclear Association. London, UK*

[6] Maziasz, P. J., & Busby, J. T. (2012). *Properties of Austenitic Stainless Steels for Nuclear Reactor Applications*. Elsevier, Oxford, England. Oak Ridge National Lab (ORNL), Oak Ridge, TN (United States), Comprehensive Nuclear Materials, Volume 7, 2020, 303-318. https://doi.org/10.1016/B978-0-08-056033-5.00019-7

[7] Chant, & Murty, K. L. (2010). Structural materials issues for the next generation fission reactors. *Journal of Materials (1989)*, *62*(9), 67–74. https://doi.org/10.1007/s11837-010-0142-3

[8] Zinkle, S. J. & Busby, J. T. (2009). Structural materials for fission & fusion energy. *Materials Today*, *12*(11), 12–19. https://doi.org/10.1016/S1369-7021(09)70294-9

[9] Locatelli, G. Mancini, M., & Todeschini, N. (2013). Generation IV nuclear reactors: Current status and future prospects. *Energy Policy*, *61*, 1503–1520. https://doi.org/10.1016/j.enpol.2013.06.101

[10] Was, G. S., Petti, D., Ukai, S., & Zinkle, S. (2019). Materials for future nuclear energy systems. *Journal of Nuclear Materials*, *527*, 151837–. https://doi.org/10.1016/j.jnucmat.2019.151837

[11] Jenkins, M.L. & Kirk, M. (2000). *Characterisation of Radiation Damage by Transmission Electron Microscopy*. Institute of Physics Publishing, Philadelphia, PA, CRC Press. https://doi.org/10.1201/9781420034646

[12] Corbett, J.W. & Ianniello, L. C. (1972). Radiation induced voids in metals (Research on neutron irradiation induced voids in metals). *Radiation Induced Voids in Metals (Research on Neutron Irradiation Induced Voids in Metals)*, 884P–884P.

[13] Norris, D.I.R. (1972). Voids in irradiated metals (Part I). *Radiation Effects*, *14*(1-2), 1–37. https://doi.org/10.1080/00337577208230470

[14] Stewart, D., Osetskiy, Y., & Stoller, R. (2011). Atomistic studies of formation and diffusion of helium clusters and bubbles in BCC iron. *Journal of Nuclear Materials*, *417*(1-3), 1110–1114. https://doi.org/10.1016/j.jnucmat.2010.12.217

[15] Hasegawa, A. Fukuda, M., Tanno, T., & Nogami, S. (2013). Neutron Irradiation Behavior of Tungsten. *Materials Transactions*, *54*(4), 466–471. https://doi.org/10.2320/matertrans.MG201208

[16] Maziasz, P.J. (1993). Overview of microstructural evolution in neutron-irradiated austenitic stainless steels. *Journal of Nuclear Materials*, *205*, 118–145. https://doi.org/10.1016/0022-3115(93)90077-C

[17] Simonen, E. P., & Brimhall, J. L. (1975). *Dependence of swelling on void surface reaction rate constants* (No. BNWL-SA-5377; CONF-751006-3). Battelle Pacific Northwest Labs., Richland, Washington (USA).

[18] Cawthorne, C. & Fulton, E. J. (1966). The influence of irradiation temperature on the defect structures in stainless steel (Electron microscopic studies of influence of irradiation temperature on defect structures in stainless steel). *Its Nature of Small Defect Clusters,* 1996*,* 446–460.

[19] Huebotter, Bump, T. R., Sha, W. T., Eggen, D. T., & Fulford, P. J. (1971). *Design, Research, And Development Implications of Metal Swelling In Fast Reactors*. (No. ANL-7786). Argonne National Lab., Illinois (USA).

[20] Edwards, D. J., Simonen, E. P., Garner, F. A., Greenwood, L. R., Oliver, B. M., & Bruemmer, S. M. (2003). Influence of irradiation temperature and dose gradients on the microstructural evolution in neutron-irradiated 316SS. *Journal of nuclear materials*, *317*(1), 32-45. https://doi.org/10.1016/S0022-3115(03)00003-5

[21] Grosse, M. (2012). *High-temperature oxidation in nuclear reactor systems* (Issue 22, pp. 265–300). Woodhead Publishing Limited. Elsevier Science & Technology, https://doi.org/10.1533/9780857095343.3.265

[22] Cattant, F. Crusset, D., & Féron, D. (2008). Corrosion issues in nuclear industry today. *Materials Today*, *11*(10), 32–37. https://doi.org/10.1016/S1369-7021(08)70205-0

Background

[1] De La Rubia, T. D., Averback, R. S., Benedek, R., & King, W. E. (1988). Role of Thermal Spikes in Energetic Displacement Cascades. *Physical Review Letters*, *60*(1), 76–76. https://doi.org/10.1103/PhysRevLett.60.76.3

[2] Nordlund, K. & Djurabekova, F. (2014). Multiscale modelling of irradiation in nanostructures. *Journal of Computational Electronics*, *13*(1), 122–141. https://doi.org/10.1007/s10825-013-0542-z

[3] Wiedersich, H. (1972). On the theory of void formation during irradiation. *Radiation Effects 12: 1-2,* 111–125. https://doi.org/10.1080/00337577208231128

[4] Garner, F. A. (2010). 10 - Void swelling and irradiation creep in light water reactor (LWR) environments. In *Understanding and mitigating ageing in nuclear power plants* (pp. 308–356). Elsevier Ltd. https://doi.org/10.1533/9781845699956.2.308

[5] Garner, F. A. (2020). 3.02 - Radiation-Induced Damage in Austenitic Structural Steels Used in Nuclear Reactors. In *Comprehensive Nuclear Materials* (Second Edition, pp. 57–168). Elsevier Ltd. https://doi.org/10.1016/B978-0-12-803581-8.12067-3

[6] Norgett, M. J., Robinson, M. T., & Torrens, I. M. (1975). A proposed method of calculating displacement dose rates. *Nucl. Eng. Des., V. 33, No. 1, Pp. 50-54*, *33*(1), 50–54. https://doi.org/10.1016/0029-5493(75)90035-7

[7] Lindhard, J. & Scharff, M. (1961). Energy Dissipation by Ions in the kev Region. *Physical Review (U.S.) Superseded in Part by Phys. Rev. A, Phys. Rev. B: Solid State, Phys. Rev. C, and Phys. Rev. D*, *124*(1), 128–130. https://doi.org/10.1103/PhysRev.124.128

[8] Bohr, N. (1913). II. On the theory of the decrease of velocity of moving electrified particles on passing through matter. *The London, Edinburgh and Dublin Philosophical Magazine and Journal of Science*, *25*(145), 10–31. https://doi.org/10.1080/14786440108634305

[9] King, W. E. Merkle, K. L., & Meshii, M. (1983). Threshold energy surface and Frenkel pair resistivity for Cu. *Journal of Nuclear Materials*, *117*(JUL), 12–25. https://doi.org/10.1016/0022-3115(83)90005-3

[10] ASTM Standards, *ASTM International*, PA, E706(ID), ASTM E693-12, (2012).

[11] MATLAB. Version 9.4.0 (R2018a). Natick, Massachusetts: The MathWorks Inc., (2018).

[12] Mehrer, H. & Seeger, A. (1969). Interpretation of Self-Diffusion and Vacancy Properties in Copper. *Physica Status Solidi*, *35*(1), 313–328. https://doi.org/10.1002/pssb.19690350132

[13] Bourassa, R. R. & Lengeler, B. (1976). The formation and migration energies of vacancies in quenched copper. *Journal of Physics. F, Metal Physics*, *6*(8), 1405–1413. https://doi.org/10.1088/0305-4608/6/8/003

[14] Kornbilt, L. (1980). Elastic Calculation of Self-Interstitial Formation Energies In FCC Metals. *Physical Review. B, Condensed Matter*, *22*(4), 1866–1870. https://doi.org/10.1103/PhysRevB.22.1866

[15] Lam, N.Q. Dagens, L., & Doan, N. V. (1983). Calculations of the properties of self-interstitials and vacancies in the face-centered cubic metals Cu, Ag and Au. *Journal of Physics. F, Metal Physics*, *13*(12), 2503–2516. https://doi.org/10.1088/0305-4608/13/12/009

[16] Korhonen, T., Puska, M., & Nieminen, R. (1995). Vacancy-Formation Energies For FCC And BCC Transition-Metals. *Physical Review. B, Condensed Matter*, *51*(15), 9526–9532. https://doi.org/10.1103/PhysRevB.51.9526

[17] Lynn, & Schultz, P. J. (1985). Vacancy formation energy measurements in single crystal aluminum using a variable-energy positron beam. *Applied Physics A Solids and Surfaces*, *38*(4), 293–293. https://doi.org/10.1007/BF00616066

[18] Osono, H., Hashimoto, E., & Kino, T. (2001). Thermal generation of vacancies in high-quality aluminium crystals. *Philosophical Magazine. A, Physics of Condensed Matter. Defects and Mechanical Properties*, *81*(12), 2925–2925. https://doi.org/10.1080/01418610108217174

[19] Jesson, B. J., Foley, M., & Madden, P. (1997). Thermal properties of the self-interstitial in aluminum: An ab initio molecular-dynamics study. *Physical Review. B, Condensed Matter*, *55*(8), 4941–4946. https://doi.org/10.1103/PhysRevB.55.4941

[20] Schultz, H. (1991). Defect parameters of b.c.c. metals: group-specific trends. *Materials Science & Engineering A*, *141*(2), 149–167. https://doi.org/10.1016/0921-5093(91)90766-G

[21] Ma, P. W., & Dudarev, S. L. (2019). Universality of point defect structure in body-centered cubic metals. *Physical Review Materials*, *3*(1), 013605. https://doi.org/10.1103/PhysRevMaterials.3.013605

[22] Stoller R. E., Odette, G. R., & Wirth, B. D. (1997). Primary damage formation in bcc iron. *Journal of Nuclear Materials*, *251*(1-3), 49–60. https://doi.org/10.1016/S0022-3115(97)00256-0

[23] Fu, C. C., Torre, J. D., Willaime, F., Bocquet, J. L., & Barbu, A. (2005). Multiscale modelling of defect kinetics in irradiated iron. *Nature materials*, *4*(1), 68-74. https://doi.org/10.1038/nmat1286

[24] Maier, K., Peo, M., Saile, B., Schaefer, H. E., & Seeger, A. (1979). High–temperature positron annihilation and vacancy formation in refractory metals. *Philosophical Magazine A*, *40*(5), 701-728. https://doi.org/10.1080/01418617908234869

[25] Dudarev, S. L., Derlet, P. M., & Woo, C. H. (2007). Driven mobility of self-interstitial defects under electron irradiation. *Nuclear Instruments and Methods in Physics Research Section B: Beam Interactions with Materials and Atoms*, *256*(1), 253-259. https://doi.org/10.1016/j.nimb.2006.12.013

[26] Guinan, Stuart, R., & Borg, R. (1977). Fully Dynamic Computer-Simulation Of Self-Interstitial Diffusion In Tungsten. *Physical Review. B, Condensed Matter*, *15*(2), 699–710. https://doi.org/10.1103/PhysRevB.15.699

[27] Wirth, B.D., Caturla, M. J., Diaz de la Rubia, T., Khraishi, T., & Zbib, H. (2001). Mechanical property degradation in irradiated materials: A multiscale modeling approach. *Nuclear Instruments & Methods in Physics Research. Section B, Beam Interactions with Materials and Atoms*, *180*(1), 23–31. https://doi.org/10.1016/S0168-583X(01)00392-5

[28] Robach, J. S., Robertson, I. M., Wirth, B. D., & Arsenlis, A. (2003). In-situ transmission electron microscopy observations and molecular dynamics simulations of dislocation-defect interactions in ion-irradiated copper. *Philosophical Magazine (Abingdon, England)*, *83*(8), 955–967. https://doi.org/10.1080/0141861031000065329

[29] Brailsford, A. D., & Bullough, R. (1981). The Theory of Sink Strengths. *Philosophical Transactions of the Royal Society of London. Series A: Mathematical and Physical Sciences*, *302*(1465), 87–137. https://doi.org/10.1098/rsta.1981.0158

[30] Gan, J., Was, G. S., & Stoller, R. E. (2001). Modeling of microstructure evolution in austenitic stainless steels irradiated under light water reactor condition. *Journal of Nuclear Materials*, *299*(1), 53–67. https://doi.org/10.1016/S0022-3115(01)00673-0

[31] Katoh, Y., Stoller, R. E., & Kohyama, A. (1994). Rate theory investigation of influence of cascade cluster formation and solute trapping on point defect agglomeration and extended defect evolution. *Journal of Nuclear Materials*, *212*, 179–185. https://doi.org/10.1016/0022-3115(94)90052-3

[32] Barashev, A. V., Golubov, S. I., & Stoller, R. E. (2015). Theoretical investigation of microstructure evolution and deformation of zirconium under neutron irradiation. *Journal of Nuclear Materials*, *461*(C), 85–94. https://doi.org/10.1016/j.jnucmat.2015.02.001

[33] Singh, B. N., Foreman, A. J. E., & Trinkaus, H. (1997). Radiation hardening revisited: role of intracascade clustering. *Journal of Nuclear Materials*, *249*(2), 103–115. https://doi.org/10.1016/S0022-3115(97)00231-6

[34] Trinkaus, H. (1983). Theory of the nucleation of multicomponent precipitates. *Physical Review. B, Condensed Matter*, *27*(12), 7372–7378. https://doi.org/10.1103/PhysRevB.27.7372

[35] Stoller, R. E. & Zarkadoula, E. (2020). 1.20 - Primary Radiation Damage Formation in Solids. In *Comprehensive Nuclear Materials* (Second Edition, pp. 620–662). Elsevier Ltd. https://doi.org/10.1016/B978-0-12-803581-8.00661-5

[36] Andresen, P.L. & Was, G. S. (2019). A historical perspective on understanding IASCC. *Journal of Nuclear Materials*, *517*, 380–392. https://doi.org/10.1016/j.jnucmat.2019.01.057

[37] Bruemmer, S. M., Simonen, E. P., Scott, P. M., Andresen, P. L., Was, G. S., & Nelson, J. L. (1999). Radiation-induced material changes and susceptibility to intergranular failure of light-water-reactor core internals. *Journal of Nuclear Materials*, *274*(3), 299-314. https://doi.org/10.1016/S0022-3115(99)00075-6

[38] Atkinson, H. V. (1985). Review of the role of short-circuit diffusion in the oxidation of nickel, chromium, and nickel-chromium alloys. *Oxidation of Metals*, *24*(3-4), 177–197. https://doi.org/10.1007/BF00664231

[39] Macdonald, D. D. (2011). The history of the Point Defect Model for the passive state: A brief review of film growth aspects. *Electrochimica Acta*, *56*(4), 1761–1772. https://doi.org/10.1016/j.electacta.2010.11.005

[40] Tedmon, C.S. (1966). Effect of Oxide Volatilization on Oxidation Kinetics o f Cr And Fe-Cr Alloys. *Journal of the Electrochemical Society*, *113*(8), 766–. https://doi.org/10.1149/1.2424115

[41] Lillerud, K. P. & Kofstad, P. (1980). On High Temperature Oxidation of Chromium: I. Oxidation of Annealed, Thermally Etched Chromium at 800°–1100°C. *Journal of the Electrochemical Society*, *127*(11), 2397–2410. https://doi.org/10.1149/1.2129478

[42] Lillerud, K. P. & Kofstad, P. (1980). On High Temperature Oxidation of Chromium: II. Oxidation of Annealed, Thermally Etched Chromium at 800°–1100°C. *Journal of the Electrochemical Society*, *127*(11), 2410–2419. https://doi.org/10.1149/1.2129481

[43] Gulbransen, E.A. & Andrew, K. (1957). Kinetics Of The Oxidation Of Chromium. *Journal of the Electrochemical Society*, *104*(6), 334–338. https://doi.org/10.1149/1.2428576

[44] Legrand, M., Diawara, B., Legendre, J.-J., & Marcus, P. (2002). Three-dimensional modelling of selective dissolution and passivation of iron–chromium alloys. *Corrosion Science*, *44*(4), 773–790. https://doi.org/10.1016/S0010-938X(01)00073-7

[45] Diawara, B., Legrand, M., Legendre, J., & Marcus, P. (2004). Use of quantum chemistry results in 3D modeling of corrosion of iron-chromium alloys. *Journal of the Electrochemical Society*, *151*(3), B172–B178. https://doi.org/10.1149/1.1646408

[46] Diawara, B., Beh, Y.-A., & Marcus, P. (2010). Nucleation and Growth of Oxide Layers on Stainless Steels (FeCr) Using a Virtual Oxide Layer Model. *Journal of Physical Chemistry. C*, *114*(45), 19299–19307. https://doi.org/10.1021/jp909445x

[47] Sabioni, A.C.S., Huntz, A., Philibert, J., Lesage, B., & Monty, C. (1992). Relation Between The Oxidation Growth-Rate Of Chromia Scales And Self-Diffusion In Cr_2O_3. *Journal of Materials Science*, *27*(17), 4782–4790. https://doi.org/10.1007/BF01166020

[48] Sabioni, A.C.S., Lesage, B., Huntz, A. M., Pivin, J. C., & Monty, C. (1992). Self-diffusion in Cr_2O_3 I. Chromium diffusion in single crystals. *Philosophical Magazine. A, Physics of Condensed Matter. Defects and Mechanical Properties*, *66*(3), 333–350. https://doi.org/10.1080/01418619208201560

[49] Sabioni, A.C.S., Lesage, B., Huntz, A. M., Pivin, J. C., & Monty, C. (1992). Self-diffusion in Cr_2O_3 II. Oxygen diffusion in single crystals. *Philosophical Magazine. A, Physics of Condensed Matter. Defects and Mechanical Properties*, *66*(3), 351–360. https://doi.org/10.1080/01418619208201561

[50] Sabioni, A.C.S., Lesage, B., Huntz, A. M., Pivin, J. C., & Monty, C. (1992). Self-diffusion in Cr_2O_3 III. Chromium and oxygen grain-boundary diffusion in polycrystals. *Philosophical Magazine. A, Physics of Condensed Matter. Defects and Mechanical Properties*, *66*(3), 361–374. https://doi.org/10.1080/01418619208201562

[51] Latu-Romain, L., Parsa, Y., Mathieu, S., Vilasi, M., Galerie, A., & Wouters, Y. (2017). Towards the growth of stoichiometric chromia on pure chromium by the control of temperature and oxygen partial pressure. *Corrosion Science*, *126*, 238–246. https://doi.org/10.1016/j.corsci.2017.07.005

[52] Huntz, A. M. & Tsai, S. C. (1994). Diffusion in Oxide Scales: Application to Cr_2O_3 Scales. *Journal of Materials Science Letters*, *13*(11), 821–825. https://doi.org/10.1007/BF00271331

[53] Kofstad, P. & Lillerud, K. P. (1982). Chromium transport through Cr_2O_3 scales I. On lattice diffusion of chromium. *Oxidation of Metals*, *17*(3-4), 177–194. https://doi.org/10.1007/BF00738381

[54] Tsai, S., Huntz, A., & Dolin, C. (1996). Growth mechanism of Cr_2O_3 scales: Oxygen and chromium diffusion, oxidation kinetics and effect of yttrium. *Materials Science & Engineering. A, Structural Materials : Properties, Microstructure and Processing*, *212*(1), 6–13. https://doi.org/10.1016/0921-5093(96)10173-8

[55] Hoshino, K. & Peterson, N. L. (1983). Cation Self-Diffusion in Cr_2O_3. *Journal of the American Ceramic Society*, *66*(11), c202–c203. https://doi.org/10.1111/j.1151-2916.1983.tb10572.x

[56] Schmucker, E., Petitjean, C., Martinelli, L., Panteix, P.-J., Lagha, B., & Vilasi, M. (2016). Oxidation of Ni-Cr alloy at intermediate oxygen pressures. II. Towards the lifetime prediction of alloys. *Corrosion Science*, *111*, 467–473. https://doi.org/10.1016/j.corsci.2016.05.024

[57] Lebreau, F., Islam, M. M., Diawara, B., & Marcus, P. (2014). Structural, Magnetic, Electronic, Defect, and Diffusion Properties of Cr_2O_3: A DFT+U Study. *Journal of Physical Chemistry. C*, *118*(31), 18133–18145. https://doi.org/10.1021/jp5039943

[58] Medasani, F., Sushko, M. L., Rosso, K. M., Schreiber, D. K., & Bruemmer, S. M. (2019). Temperature Dependence of Self-Diffusion in Cr_2O_3 from First Principles. *Journal of Physical Chemistry C*, *123*(36), 22139–22150. https://doi.org/10.1021/acs.jpcc.9b03218

[59] Medasani, F., Sushko, M. L., Rosso, K. M., Schreiber, D. K., & Bruemmer, S. M. (2018). First-Principles Investigation of Native Interstitial Diffusion in Cr_2O_3. *Journal of Physical Chemistry C*, *122*(24), 12984–12993. https://doi.org/10.1021/acs.jpcc.8b04383

[60] Gray, Lei, Y., & Wang, G. (2016). Charged vacancy diffusion in chromium oxide crystal: DFT and DFT+U predictions. *Journal of Applied Physics*, *120*(21), 215101–. https://doi.org/10.1063/1.4970882

[61] Holt, & Kofstad, P. (1994). Electrical conductivity and defect structure of Cr_2O_3. I. High temperatures (>∼1000°C). *Solid State Ionics*, *69*(2), 127–136. https://doi.org/10.1016/0167-2738(94)90401-4

[62] Hosemann, P., Hofer, C., Hlawacek, G., Li, N., Maloy, S. A., & Teichert, C. (2012). Structural, electrical and magnetic measurements on oxide layers grown on 316L exposed to liquid leadabismuth eutectic. *Journal of Nuclear Materials*, *421*(1-3), 140–146. https://doi.org/10.1016/j.jnucmat.2011.11.042

[63] Chen, J., Xiao, Q., Lu, Z., Ru, X., Peng, H., Xiong, Q., & Li, H. (2017). Characterization of interfacial reactions and oxide films on 316L stainless steel in various simulated PWR primary water environments. *Journal of Nuclear Materials*, *489*, 137–149. https://doi.org/10.1016/j.jnucmat.2017.03.029

[64] Zhang, J. & Li, N. (2008). Review of the studies on fundamental issues in LBE corrosion. *Journal of Nuclear Materials*, *373*(1), 351–377. https://doi.org/10.1016/j.jnucmat.2007.06.019

[65] Xu, Zhang, Y., Li, X., Liu, W., Li, D., Liu, C. S., Pan, B. C., & Wang, Z. (2017). Effects of iron and chromium on the dynamic properties of oxygen in liquid lead–bismuth eutectic alloy. *Corrosion Science*, *118*, 1–11. https://doi.org/10.1016/j.corsci.2017.01.003

[66] Shankar Rao, V., Lim, J., Hwang, I. S., & Singhal, L. K. (2012). Characterization of oxide scales grown on 216L stainless steels in liquid lead–bismuth eutectic. *Corrosion Science*, *63*, 113–118. https://doi.org/10.1016/j.corsci.2012.05.016

[67] Soulas, R., Cheynet, M., Rauch, E., Neisius, T., Legras, L., Domain, C., & Brechet, Y. (2013). TEM investigations of the oxide layers formed on a 316L alloy in simulated PWR environment. *Journal of Materials Science*, *48*(7), 2861–2871. https://doi.org/10.1007/s10853-012-6975-0

[68] Qiu, Han, J., Schoell, R., Popovic, M., Ghanbari, E., Kaoumi, D., Scully, J. R., Macdonald, D. D., & Hosemann, P. (2020). *Electrical properties of thermal oxide scales on pure iron in liquid lead-bismuth eutectic*. https://doi.org/10.48550/arXiv.2010.05372

[69] Jiao, Z. & Was, G. S. (2011). Oxidation of a Proton-Irradiated 316 Stainless Steel in Simulated BWR NWC Environment. In *Proceedings of the 15th International Conference on Environmental Degradation of Materials in Nuclear Power Systems — Water Reactors* (pp. 1329–1338). Springer International Publishing. https://doi.org/10.1007/978-3-319-48760-1_81

[70] Schroer, C, Nold, E, and Konys, J. (2009) Micro-Analysis of 316L Stainless-Steel After Long-Term Exposure to Lead-Bismuth Eutectic at 550 C. In *Proceedings of EUROCORR*, Nice, France.

[71] Chao, C. Y., Lin, L. F., & Macdonald, D. D. (1981). A Point Defect Model for Anodic Passive Films: I . Film Growth Kinetics. *Journal of the Electrochemical Society*, *128*(6), 1187–1194. https://doi.org/10.1149/1.2127591

[72] Frazer, D., Qvist, S., Parker, S., Krumwiede, D. L., Caro, M., Tesmer, J., Maloy, S. A., Wang, Y. Q., & Hosemann, P. (2016). Degradation of HT9 under simultaneous ion beam irradiation and liquid metal corrosion. *Journal of Nuclear Materials*, *479*(C), 382–389. https://doi.org/10.1016/j.jnucmat.2016.06.039

[73] Deng, P., Peng, Q., Han, E.-H., Ke, W., Sun, C., & Jiao, Z. (2017). Effect of irradiation on corrosion of 304 nuclear grade stainless steel in simulated PWR primary water. *Corrosion Science*, *127*, 91–100. https://doi.org/10.1016/j.corsci.2017.08.010

[74] Perrin, S., Marchetti, L., Duhamel, C., Sennour, M., & Jomard, F. (2013). Influence of Irradiation on the Oxide Film Formed on 316 L Stainless Steel in PWR Primary Water. *Oxidation of Metals*, *80*(5-6), 623–633. https://doi.org/10.1007/s11085-013-9401-3

[75] Schmidt, F., Hosemann, P., Scarlat, R. O., Schreiber, D. K., Scully, J. R., & Uberuaga, B. P. (2021). Effects of Radiation-Induced Defects on Corrosion. *Annual Review of Materials Research*, *51*(1), 293–328. https://doi.org/10.1146/annurev-matsci-080819-123403

[76] Eichenberg, J.D. (1960). Irradiation of UO_2 fuel rods : the X-1-L experiment / J.D. Eichenberg, R.M. Lieberman, and F.P. Mrazik. *Bettis Atomic Power Laboratory*, 1960.

[77] Dalgaard, S. B. (1962). Corrosion and hydriding behaviour of some Zr 2.5 wt% Nb alloys in water,steam and various gases at high temperature. Presented at *IAEA Conference on Corrosion of Reactor Materials*, Salzburg, June 1962

[78] Krause-Rehberg, R., Leipner, H. S., Abgarjan, T., & Polity, A. (1998). Review of defect investigations by means of positron annihilation in II-VI compound semiconductors. *Applied Physics A: Materials Science & Processing*, *66*(6). https://doi.org/10.1007/s003390050721

[79] Makhov, A. F. (1961). The penetration of electrons into solids. 1. The intensity of an electron beam, transverse paths of electrons. *Soviet Physics-Solid State*, *2*(9), 1934-1941.

[80] Asoka-Kumar, P., & Lynn, K. G., (1990). Implantation Profile Of Low-Energy Positrons In Solids. *Applied Physics Letters*, *57*(16), 1634–1636. https://doi.org/10.1063/1.104071

[81] Nagai, Y., Takadate, K., Tang, Z., Ohkubo, H., Sunaga, H., Takizawa, H., & Hasegawa, M. (2011). Effect of electron- and neutron-irradiation on Fe-Cu model alloys studied by positron annihilation spectroscopy. *International Workshop On Positron Studies Of Defects (PSD-08)*, *265*(1), 012007–6. https://doi.org/10.1088/1742-6596/265/1/012007

[82] Selim, F.A., Wells, D. P., Harmon, J. F., & Williams, J. (2005). Development of accelerator-based γ -ray-induced positron annihilation spectroscopy technique. *Journal of Applied Physics*, *97*(11), 113539–113539–5. https://doi.org/10.1063/1.1925769

[83] Eldrup, M. & Singh, B. N. (1997). Studies of defects and defect agglomerates by positron annihilation spectroscopy. *Journal of Nuclear Materials*, *251*, 132–138. https://doi.org/10.1016/S0022-3115(97)00221-3

[84] Asoka-Kumar, P., Alatalo, M., Ghosh, V., Kruseman, A., Nielsen, B., & Lynn, K. (1996). Increased elemental specificity of positron annihilation spectra. *Physical Review Letters*, *77*(10), 2097–2100. https://doi.org/10.1103/PhysRevLett.77.2097

[85] Hautojärvi, Dupasquier, A., Hautojärvi, P. (Pekka), & Dupasquier, A. (Alfredo). (1979). *Positrons in solids*. pp. 491-522. Springer-Verlag.

[86] Brandt, W. & Dupasquier A. (1981). *Proceedings of the International School of Physics "Enrico Fermi" Course 83*; Positron Solid-State Physics, Varenna on Lake Como, 1981.

[87] Dupasquier, A. & Zecca, A. (1985). Atomic And Solid-State Physics Experiments With Slow-Positron Beams. *La Rivista Del Nuovo Cimento*, *8*(12), 1–73. https://doi.org/10.1007/BF02724348

[88] Puska, M.J. & Nieminen, R. (1994). Theory Of Positrons In Solids And On Solid-Surfaces. *Reviews of Modern Physics*, *66*(3), 841–897. https://doi.org/10.1103/RevModPhys.66.841

[89] Čížek, J. (2018). Characterization of lattice defects in metallic materials by positron annihilation spectroscopy: A review. *Journal of Materials Science & Technology*, *34*(4), 577–598. https://doi.org/10.1016/j.jmst.2017.11.050

[90] Weisberg, H. & Berko, S. (1967). Positron Lifetimes In Metals. *Physical Review., 154: 249-57(Feb. 10, 1967)*, *154*(2), 249–257. https://doi.org/10.1103/PhysRev.154.249

[91] McGuire, S. & Keeble, D. J. (2006). Positron lifetimes of polycrystalline metals: A positron source correction study. *Journal of Applied Physics*, *100*(10), 103504–. https://doi.org/10.1063/1.2384794

[92] Kuriplach, J., Morales, A., Dauwe, C., Segers, D., & Sob, M. (1998). Vacancies and vacancy-oxygen complexes in silicon: Positron annihilation with core electrons. *Physical Review. B*, *58*(16), 10475–10483. https://doi.org/10.1103/PhysRevB.58.10475

[93] Kuriplach, J. & Barbiellini, B. (2014). Improved generalized gradient approximation for positron states in solids. *Physical Review. B*, *89*(15). https://doi.org/10.1103/PhysRevB.89.155111

[94] Selim, F. A., Wells, D. P., Harmon, J. F., & Williams, J. (2005). High depth nondestructive stress measurements on thick steel alloys. *Journal of Applied Physics*, *97*(11), 113540–113540–8. https://doi.org/10.1063/1.1925770

[95] Onitsuka, T., Takenaka, M., Kuramoto, E., Nagai, Y., & Hasegawa, M. (2002). Deformation-enhanced Cu precipitation in Fe-Cu alloy studied by positron annihilation spectroscopy. *Physical Review. B*, *65*(1). https://doi.org/10.1103/PhysRevB.65.012204

[96] Nagai, Y. Tang, Z., Hassegawa, M., Kanai, T., & Saneyasu, M. (2001). Irradiation-induced Cu aggregations in Fe: An origin of embrittlement of reactor pressure vessel

steels. *Physical Review. B, Condensed Matter*, *63*(13). https://doi.org/10.1103/PhysRevB.63.134110

[97] Čížek, J., Lukáč, F., Procházka, I., Kužel, R., Jirásková, Y., Janičkovič, D., Anwand, W., & Brauer, G. (2012). Characterization of quenched-in vacancies in Fe–Al alloys. *Physica. B, Condensed Matter*, *407*(14), 2659–2664. https://doi.org/10.1016/j.physb.2011.12.122

[98] Hardie, Williams, C. A., Xu, S., & Roberts, S. G. (2013). Effects of irradiation temperature and dose rate on the mechanical properties of self-ion implanted Fe and Fe–Cr alloys. *Journal of Nuclear Materials*, *439*(1-3), 33–40. https://doi.org/10.1016/j.jnucmat.2013.03.052

[99] Jiang, J., Wu, Y. C., Liu, X. B., Wang, R. S., Nagai, Y., Inoue, K., Shimizu, Y., & Toyama, T. (2015). Microstructural evolution of RPV steels under proton and ion irradiation studied by positron annihilation spectroscopy. *Journal of Nuclear Materials*, *458*, 326–334. https://doi.org/10.1016/j.jnucmat.2014.12.113

[100] Liu, X., Wang, R., Ren, A., Huang, P., Wu, Y., Jiang, J., Zhang, C., & Wang, X. (2012). Positron annihilation study of proton-irradiated reactor pressure vessel steels. *Radiation Physics and Chemistry (Oxford, England : 1993)*, *81*(10), 1586–1592. https://doi.org/10.1016/j.radphyschem.2012.05.014

[101] Lambrecht, M. & Malerba, L. (2011). Positron annihilation spectroscopy on binary Fe–Cr alloys and ferritic/martensitic steels after neutron irradiation. *ACTA MATERIALIA*, *59*(17), 6547–6555. https://doi.org/10.1016/j.actamat.2011.06.046

[102] Terentyev, D., Malerba, L., & Barashev, A. V. (2005). On the correlation between self-interstitial cluster diffusivity and irradiation-induced swelling in Fe-Cr alloys. *Philosophical Magazine Letters*, *85*(11), 587–594. https://doi.org/10.1080/09500830500383563

[103] Terentyev, D., Olsson, P., Malerba, L., & Barashev, A. V. (2007). Characterization of dislocation loops and chromium-rich precipitates in ferritic iron–chromium alloys as means of void swelling suppression. *Journal of Nuclear Materials*, *362*(2-3), 167–173. https://doi.org/10.1016/j.jnucmat.2007.01.069

[104] Terentyev, D., Malerba, L., & Barashev, A. V. (2008). Modelling the diffusion of self-interstitial atom clusters in Fe–Cr alloys. *Philosophical Magazine*, *88*(1), 21-29. https://doi.org/10.1080/14786430701727513

[105] Chaouadi, R., & Gérard, R. (2005). Copper precipitate hardening of irradiated RPV materials and implications on the superposition law and re-irradiation kinetics. *Journal of Nuclear Materials*, *345*(1), 65–74. https://doi.org/10.1016/j.jnucmat.2005.05.001

[106] Lambrecht, M., Meslin, E., Malerba, L., Hernández-Mayoral, M., Bergner, F., Pareige, P., Radiguet, B., & Almazouzi, A. (2010). On the correlation between irradiation-induced microstructural features and the hardening of reactor pressure vessel steels. *Journal of Nuclear Materials*, *406*(1), 84–89. https://doi.org/10.1016/j.jnucmat.2010.05.020

[107] Odette. G.R. (1983). On the dominant mechanism of irradiation embrittlement of reactor pressure vessel steels. *Scripta Metallurgica*, *17*(10), 1183–1188. https://doi.org/10.1016/0036-9748(83)90280-6

[108] Fisher, S. B., Harbottle, J. E., & Aldridge, N. (1985). Radiation Hardening in Magnox Pressure-Vessel Steels. *Philosophical Transactions of the Royal Society of London. Series A: Mathematical and Physical Sciences*, *315*(1532), 301–332. https://doi.org/10.1098/rsta.1985.0042

[109] Carter, R.G., Soneda, N., Dohi, K., Hyde, J. M., English, C. A., & Server, W. L. (2001). Microstructural characterization of irradiation-induced Cu-enriched clusters in reactor pressure vessel steels. *Journal of Nuclear Materials*, *298*(3), 211–224. https://doi.org/10.1016/S0022-3115(01)00659-6

[110] U.S. Nuclear Regulatory Commission, (2000). NRC NUREG-1511, Supplement 2 Reactor Pressure Vessel Status Report

[111] Sato, K., Kawamoto, S., Ikemura, K., Krsjak, V., Vieh, C., Brun, R., Xu, Q., Yoshiie, T., & Dai, Y. (2014). Positron annihilation spectroscopy of ferritic/martensitic steels F82H and T91 irradiated with protons and neutrons at PSI. *Journal of Nuclear Materials*, *450*(1-3), 59–63. https://doi.org/10.1016/j.jnucmat.2013.09.009

[112] Nagai, Hasegawa, M., Tang, Z., Hempel, A., Yubuta, K., Shimamura, T., Kawazoe, Y., Kawai, A., & Kano, F. (2000). Positron confinement in ultrafine embedded particles: Quantum-dot-like state in an Fe-Cu alloy. *Physical Review. B*, *61*(10), 6574–6578. https://doi.org/10.1103/PhysRevB.61.6574

[113] Nanstad, R. K., Tipping, P., Kalkhof, R., & Sokolov, M. (2004). Irradiation and Post-Annealing Reirradiation Effects on Fracture Toughness of RPV Steel Heat JRQ. *Effects of Radiation on Materials: 21st International Symposium*, *1447*, 149–163. https://doi.org/10.1520/STP11225S

[114] Ding, Zhang, C., Zhang, X., Chen, Y., Yang, Y., Song, Y., Liu, X., & Xue, F. (2020). Post-irradiation annealing behavior of irradiation hardening of China low-Cu RPV steel. *Nuclear Materials and Energy*, *22*, 100727–. https://doi.org/10.1016/j.nme.2020.100727

[115] Standards for Protection Against Radiation, 10 C.F.R. § 20 (2007).

[116] Eldrup, M. & Singh, B. (2000). Study of defect annealing behaviour in neutron irradiated Cu and Fe using positron annihilation and electrical conductivity. *Journal of Nuclear Materials*, *276*(1), 269–277. https://doi.org/10.1016/S0022-3115(99)00186-5

[117] Singh, B. N., & Evans, J. H. (1995). Significant differences in defect accumulation behaviour between fcc and bcc crystals under cascade damage conditions. *Journal of Nuclear Materials*, *226*(3), 277-285. https://doi.org/10.1016/0022-3115(95)00121-2

[118] Singh, B. N. (1999). Atomic displacements and defect accumulation during irradiation with energetic particles: An autobiographical review. *Radiation effects and defects in solids*, *148*(1-4), 383-446. https://doi.org/10.1080/10420159908229103

[119] Trinkaus, H. (1983). Energetics and formation kinetics of helium bubbles in metals. *Radiation Effects*, *78*(1-4), 189–211. https://doi.org/10.1080/00337578308207371

[120] Allen, T. Busby, J., Meyer, M., & Petti, D. (2010). Materials challenges for nuclear systems. *Materials Today*, *13*(12), 14–23. https://doi.org/10.1016/S1369-7021(10)70220-0

[121] Kršjak, V., Hruška, P., Degmová, J., Sojak, S., Noga, P., Shen, T., Sabelová, V., Egger, W., & Sluge, V. (2021). A new approach to near-surface positron annihilation analysis of ion irradiated ferritic alloys. *Nanoscale Advances*, *3*(23), 6596–6667. https://doi.org/10.1039/d1na00394a

[122] Degmová, J., Kršjak, V., Shen, T., Šimeg Veterniková, J., Gatciová, A., Sojak, S., & Hruška, P. (2021). Near-surface investigation of positron diffusion length in helium-implanted Fe9Cr and its ODS variant. *Applied Surface Science*, *538*, 148004–. https://doi.org/10.1016/j.apsusc.2020.148004

[123] Kršjak, V., Degmová, J., Noga, P., Petriska, M., Sojak, S., Saro, M., Neuhold, I., & Slugen, V. (2021). Application of Positron Annihilation Spectroscopy in Accelerator-Based Irradiation Experiments. *Materials*, *14*(21), 6238. https://doi.org/10.3390/ma14216238

[124] Was, G.S. (2007). *Fundamentals of radiation materials science: metals and alloys*. Springer.

[125] Jin, S. Mo, B., Zhang, W., Zhang, T., Li, Y., Guo, L., Cao, X., & Wang, B. (2019). Towards understanding the evolution of dislocation loops and their interaction with vacancies in Fe9Cr alloy during the irradiation swelling incubation period. *Materialia*, *5*, 100241–. https://doi.org/10.1016/j.mtla.2019.100241

[126] Agarwal, S., Liedke, M. O., Jones, A. C. L., Reed, E., Kohnert, A. A., Uberuaga, B. P., Wang, Y. Q., Cooper, J., Kaoumi, D., Li, N., Auguste, R., Hosemann, P., Capolungo, L., Edwards, D.

J., Butterling, M., Hirschmann, E., Wagner, A., & Selim, F. A. (2020). A new mechanism for void-cascade interaction from nondestructive depth-resolved atomic-scale measurements of ion irradiation-induced defects in Fe. *Science Advances*, *6*(31), eaba8437–eaba8437. https://doi.org/10.1126/sciadv.aba8437

[127] Agarwal, S., Butterling, M., Liedke, M. O., Yano, K. H., Schreiber, D. K., Jones, A. C. L., Uberuaga, B. P., Wang, Y. Q., Chancey, M., Kim, H., Derby, B. K., Li, N., Edwards, D. J., Hosemann, P., Kaoumi, D., Hirschmann, E., Wagner, A., & Selim, F. A. (2022). The mechanism behind the high radiation tolerance of Fe–Cr alloys. *Journal of Applied Physics*, *131*(12), 125903–. https://doi.org/10.1063/5.0085086

[128] Liedke, M.O. Anwand, W., Bali, R., Cornelius, S., Butterling, M., Trinh, T. T., Wagner, A., Salamon, S., Walecki, D., Smekhova, A., Wende, H., & Potzger, K. (2015). Open volume defects and magnetic phase transition in Fe 60 Al 40 transition metal aluminide. *Journal of Applied Physics*, *117*(16), 163908–. https://doi.org/10.1063/1.4919014

[129] Anwand, W., Wagner, A., Brauer, G., Butterling, M., & Kissener, H. R. (2012). Design and Construction of a Slow Positron Beam for Solid and Surface Investigations. *Diffusion and Defect Data. Solid State Data. Pt. A, Defect and Diffusion Forum*, *331*, 25–40. https://doi.org/10.4028/www.scientific.net/DDF.331

[130] Wagner, A., Butterling, M., Liedke, M. O., Potzger, K., & Krause-Rehberg, R. (2018). Positron annihilation lifetime and Doppler broadening spectroscopy at the ELBE facility. *AIP Conference Proceedings*, *1970*(1). https://doi.org/10.1063/1.5040215

[131] Kinomura, A., Suzuki, R., Ohdaira, T., Oshima, N., O'Rourke, B. E., & Nishijima, T. (2013). In-situ positron lifetime spectroscopy of radiation damage by simultaneous irradiation of slow-positron and ion beams. *16th International Conference On Positron Annihilation (ICPA-16)*, *443*(1), 12043–12044. https://doi.org/10.1088/1742-6596/443/1/012043'

[132] Kinomura, A., Suzuki, R., Ohdaira, T., Oshima, N., O'Rourke, B. E., & Nishijima, T. (2013, June). In-situ positron lifetime spectroscopy of radiation damage by simultaneous irradiation of slow-positron and ion beams. In *Journal of Physics: Conference Series* (Vol. 443, No. 1, p. 012043). IOP Publishing. https://doi:10.1088/1742-6596/443/1/012043

[133] Iwai, T. & Tsuchida, H. (2012). In situ positron beam Doppler broadening measurement of ion-irradiated metals – Current status and potential. *Nuclear Instruments & Methods in Physics Research. Section B, Beam Interactions with Materials and Atoms*, *285*, 18–23. https://doi.org/10.1016/j.nimb.2012.05.005

[134] Tsuchida, H., Iwai, T., Awano, M., Oshima, N., Suzuki, R., Yasuda, K., Batchuluun, C., & Itoh, A. (2013). Radiation damage in nanocrystalline Ni under irradiation studied using positron annihilation spectroscopy. *Journal of Nuclear Materials*, *442*(1-3), S856–S860. https://doi.org/10.1016/j.jnucmat.2013.03.012

[135] Li, B., Krsjak, V., Degmova, J., Wang, Z., Shen, T., Li, H., Sojak, S., Slugen, V., & Kawasuso, A. (2020). Positron annihilation spectroscopy study of vacancy-type defects in He implanted polycrystalline α-SiC. *Journal of Nuclear Materials*, *535*, 152180–. https://doi.org/10.1016/j.jnucmat.2020.152180

[136] Polity, A., Huth, S., & Lausmann, M. (1999). Defect characterization in electron-irradiated 6 H − SiC by positron annihilation. *Physical Review. B, Condensed Matter*, *59*(16), 10603–10606. https://doi.org/10.1103/PhysRevB.59.10603

[137] Hui, C., Zhang, Z. D., Zhou, T. J., Ling, C. C., Beling, C. D., Fung, S., Brauer, G., Anwand, W., & Skorupa, W. (2007). Positron annihilation spectroscopic study of hydrothermal grown n-type zinc oxide single crystal. *Physica Status Solidi C - Current Topics In Solid State Physics, 4*(10), 3672–3675. https://doi.org/10.1002/pssc.200675857

[138] Fidelus, J. D., Karbowski, A., Mariazzi, S., Werner-Malento, E., Brusa, R. S., Zhou, W., & Karwasz, G. P. (2012). Combined positron-annihilation and structural studies of hydrothermally grown zirconia. *Nanomaterials and Energy*, *1*(2), 97–105. https://doi.org/10.1680/nme.11.00014

[139] Tuomisto, F. & Makkonen, I. (2013). Defect identification in semiconductors with positron annihilation: Experiment and theory. *Reviews of Modern Physics*, *85*(4), 1583–1631. https://doi.org/10.1103/RevModPhys.85.1583

[140] Haseman, M., Somodi, C. B., Stepanov, P., Wall, D. E., Boatner, L. A., Hosemann, P., Wang, Y. Q., Uberuaga, B. P., & Selim, F. A. (2021). Neutron irradiation induced defects in oxides and their impact on the oxide properties. *Journal of Applied Physics*, *129*(21), 215901–. https://doi.org/10.1063/5.0046292

[141] Derby, B., Mills, S., Agarwal, S., Valdez, J. A., Baldwin, J. K., Schneider, M. M., Minor, A. M., Uberuaga, B. P., Selim, F., & Li, N. (2022). Microstructural dependence of defect formation in iron-oxide thin films. *Applied Surface Science*, *589*, 152844–. https://doi.org/10.1016/j.apsusc.2022.152844

[142] Ohnishi, T., Shibuya, K., Yamamoto, T., & Lippmaa, M. (2008). Defects and transport in complex oxide thin films. *Journal of Applied Physics*, *103*(10), 103703–103703–6. https://doi.org/10.1063/1.2921972

[143] Sickafus, K. E., Minervini, L., Grimes, R. W., Valdez, J. A., Ishimaru, M., Li, F., McClellan, K. J., & Hartmann, T. (2000). Radiation Tolerance of Complex Oxides. *Science*, *289*(5480), 748–751. https://doi.org/10.1126/science.289.5480.748

[144] Sickafus, K. E., Grimes, R. W., Valdez, J. A., Cleave, A., Tang, M., Ishimaru, M., Corish, S. M., Stanek, C. R., & Uberuaga, B. P. (2007). Radiation-induced amorphization resistance

and radiation tolerance in structurally related oxides. *Nature Materials*, *6*(3), 217–223. https://doi.org/10.1038/nmat1842

[145] Weber, W. J., (1983). Radiation-induced swelling and amorphization in Ca2Nd8(SiO4)6O2. *Radiation Effects*, *77*(3-4), 295–308. https://doi.org/10.1080/00337578308228193

[146] Parker, C. A., Hobbs, L. W., Russell, K. C., & Clinard, F. W. (1985). Damage structures in fast neutron irradiated magnesium aluminate and electron irradiated aluminum oxynitride spinels. *Journal of Nuclear Materials*, *133*(AUG), 741–744. https://doi.org/10.1016/0022-3115(85)90248-X

[147] Sickafus, K. E., Larson, A. C., Yu, N., Nastasi, M., Hollenberg, G. W., Garner, F. A., & Bradt, R. C. (1995). Cation disorder in high dose, neutron-irradiated spinel. *Journal of Nuclear Materials*, *219*(1-3), 128–134. https://doi.org/10.1016/0022-3115(94)00386-6

[148] Sprengel, W., Oberdorfer, B., Steyskal, E.-M., & Würschum, R. (2012). Dilatometry: a powerful tool for the study of defects in ultrafine-grained metals. *Journal of Materials Science*, *47*(22), 7921–7925. https://doi.org/10.1007/s10853-012-6460-9

[149] Simmons, R. O. & Balluffi, R. (1960). Measurements Of The High-Temperature Electrical Resistance Of Aluminum - Resistivity Of Lattice Vacancies. *Physical Review*, *117*(1), 62–68. https://doi.org/10.1103/PhysRev.117.62

[150] Simmons, R. O. & Balluffi, R. (1960). Measurement Of The Equilibrium Concentration Of Lattice Vacancies In Silver Near The Melting Point. *Physical Review*, *119*(2), 600–605. https://doi.org/10.1103/PhysRev.119.600

[151] Schenkel, T., Lidia, S. M., Weis, C. D., Waldron, W. L., Schwartz, J., Minor, A. M., Hosemann, P., & Kwan, J. W. (2013). Towards pump–probe experiments of defect dynamics with short ion beam pulses. *Nuclear Instruments & Methods in Physics Research. Section B, Beam Interactions with Materials and Atoms*, *315*, 350–355. https://doi.org/10.1016/j.nimb.2013.05.074

Research Objective

[1] Edwards, D. J., Simonen, E. P., Garner, F. A., Greenwood, L. R., Oliver, B. M., & Bruemmer, S. M. (2003). Influence of irradiation temperature and dose gradients on the microstructural evolution in neutron-irradiated 316SS. *Journal of nuclear materials*, *317*(1), 32-45. https://doi.org/10.1016/S0022-3115(03)00003-5

Ex-situ PAS measurements and results on nuclear relevant materials

[1] Liedke, M.O. Anwand, W., Bali, R., Cornelius, S., Butterling, M., Trinh, T. T., Wagner, A., Salamon, S., Walecki, D., Smekhova, A., Wende, H., & Potzger, K. (2015). Open volume defects and magnetic phase transition in Fe 60 Al 40 transition metal aluminide. *Journal of Applied Physics*, *117*(16), 163908–. https://doi.org/10.1063/1.4919014

[2] Anwand, W., Wagner, A., Brauer, G., Butterling, M., & Kissener, H. R. (2012). Design and Construction of a Slow Positron Beam for Solid and Surface Investigations. *Diffusion and Defect Data. Solid State Data. Pt. A, Defect and Diffusion Forum*, *331*, 25–40. https://doi.org/10.4028/www.scientific.net/DDF.331

[3] Wagner, A., Butterling, M., Liedke, M. O., Potzger, K., & Krause-Rehberg, R. (2018). Positron annihilation lifetime and Doppler broadening spectroscopy at the ELBE facility. *AIP Conference Proceedings*, *1970*(1). https://doi.org/10.1063/1.5040215

[4] Wagner, A. Anwand, W., Attallah, A. G., Dornberg, G., Elsayed, M., Enke, D., Hussein, A. E. M., Krause-Rehberg, R., Liedke, M. O., Potzger, K., & Trinh, T. T. (2017). Positron annihilation lifetime spectroscopy at a superconducting electron accelerator. *14th International Workshop on Slow Positron Beam Techniques & Applications*, *791*(1), 12004. https://doi.org/10.1088/1742-6596/791/1/012004

[5] Mills, A.P. (1980). Time bunching of slow positrons for annihilation lifetime and pulsed laser photon absorption experiments. *Applied Physics*, *22*, 273–276. https://doi.org/10.1007/BF00899876

[6] Hirschmann, E., Butterling, M., Hernandez Acosta, U., Liedke, M. ., Attallah, A. ., Petring, P., Görler, M., Krause-Rehberg, R., & Wagner, A. (2021). A new system for real-time data acquisition and pulse parameterization for digital positron annihilation lifetime spectrometers with high repetition rates. *Journal of Instrumentation*, *16*(8), P08001–. https://doi.org/10.1088/1748-0221/16/08/P08001

[7] Čížek, J. (2018). Characterization of lattice defects in metallic materials by positron annihilation spectroscopy: A review. *Journal of Materials Science & Technology*, *34*(4), 577–598. https://doi.org/10.1016/j.jmst.2017.11.050

[8] Olsen, J.V., Kirkegaard, P., Pedersen, N. J., & Eldrup, M. (2007). PALSfit: A new program for the evaluation of positron lifetime spectra. *Physica Status Solidi. C*, *4*(10), 4004–4006. https://doi.org/10.1002/pssc.200675868

[9] Tedmon, C.S. (1966). Effect of Oxide Volatilization on Oxidation Kinetics o f Cr And Fe-Cr Alloys. *Journal of the Electrochemical Society*, *113*(8), 766–. https://doi.org/10.1149/1.2424115

[10] Lillerud, K. P. & Kofstad, P. (1980). On High Temperature Oxidation of Chromium: I. Oxidation of Annealed, Thermally Etched Chromium at 800°–1100°C. *Journal of the Electrochemical Society*, *127*(11), 2397–2410. https://doi.org/10.1149/1.2129478

[11] Lillerud, K. P. & Kofstad, P. (1980). On High Temperature Oxidation of Chromium: II. Oxidation of Annealed, Thermally Etched Chromium at 800°–1100°C. *Journal of the Electrochemical Society*, *127*(11), 2410–2419. https://doi.org/10.1149/1.2129481

[12] Gulbransen, E.A. & Andrew, K. (1957). Kinetics Of The Oxidation Of Chromium. *Journal of the Electrochemical Society*, *104*(6), 334–338. https://doi.org/10.1149/1.2428576

[13] Giletti, B.J. & Hess, K. C. (1988). Oxygen diffusion in magnetite. *Earth and Planetary Science Letters*, *89*(1), 115–122. https://doi.org/10.1016/0012-821X(88)90037-4

[14] Kaspar, T., Taylor, S. D., Yano, K. H., Lach, T. G., Zhou, Y., Zhu, Z., Kohnert, A. A., Still, E. K., Hosemann, P., Spurgeon, S. R., & Schreiber, D. K. (2021). Bulk and Short-Circuit Anion Diffusion in Epitaxial Fe2O3 Films Quantified Using Buried Isotopic Tracer Layers. *Advanced Materials Interfaces*, *8*(9). https://doi.org/10.1002/admi.202001768

[15] Legrand, M., Diawara, B., Legendre, J.-J., & Marcus, P. (2002). Three-dimensional modelling of selective dissolution and passivation of iron–chromium alloys. *Corrosion Science*, *44*(4), 773–790. https://doi.org/10.1016/S0010-938X(01)00073-7

[16] Diawara, B., Legrand, M., Legendre, J., & Marcus, P. (2004). Use of quantum chemistry results in 3D modeling of corrosion of iron-chromium alloys. *Journal of the Electrochemical Society*, *151*(3), B172–B178. https://doi.org/10.1149/1.1646408

[17] Diawara, B., Beh, Y.-A., & Marcus, P. (2010). Nucleation and Growth of Oxide Layers on Stainless Steels (FeCr) Using a Virtual Oxide Layer Model. *Journal of Physical Chemistry. C*, *114*(45), 19299–19307. https://doi.org/10.1021/jp909445x

[18] Sabioni, A.C.S., Huntz, A., Philibert, J., Lesage, B., & Monty, C. (1992). Relation Between The Oxidation Growth-Rate Of Chromia Scales And Self-Diffusion In Cr_2O_3. *Journal of Materials Science*, *27*(17), 4782–4790. https://doi.org/10.1007/BF01166020

[19] Sabioni, A.C.S., Lesage, B., Huntz, A. M., Pivin, J. C., & Monty, C. (1992). Self-diffusion in Cr_2O_3 I. Chromium diffusion in single crystals. *Philosophical Magazine. A, Physics of Condensed Matter. Defects and Mechanical Properties*, *66*(3), 333–350. https://doi.org/10.1080/01418619208201560

[20] Sabioni, A.C.S., Lesage, B., Huntz, A. M., Pivin, J. C., & Monty, C. (1992). Self-diffusion in Cr_2O_3 II. Oxygen diffusion in single crystals. *Philosophical Magazine. A, Physics of Condensed Matter. Defects and Mechanical Properties*, *66*(3), 351–360. https://doi.org/10.1080/01418619208201561

[21] Sabioni, A.C.S., Lesage, B., Huntz, A. M., Pivin, J. C., & Monty, C. (1992). Self-diffusion in Cr_2O_3 III. Chromium and oxygen grain-boundary diffusion in polycrystals. *Philosophical Magazine. A, Physics of Condensed Matter. Defects and Mechanical Properties*, *66*(3), 361–374. https://doi.org/10.1080/01418619208201562

[22] Latu-Romain, L., Parsa, Y., Mathieu, S., Vilasi, M., Galerie, A., & Wouters, Y. (2017). Towards the growth of stoichiometric chromia on pure chromium by the control of temperature and oxygen partial pressure. *Corrosion Science*, *126*, 238–246. https://doi.org/10.1016/j.corsci.2017.07.005

[23] Huntz, A. M. & Tsai, S. C. (1994). Diffusion in Oxide Scales: Application to Cr_2O_3 Scales. *Journal of Materials Science Letters*, *13*(11), 821–825. https://doi.org/10.1007/BF00271331

[24] Kofstad, P. & Lillerud, K. P. (1982). Chromium transport through Cr_2O_3 scales I. On lattice diffusion of chromium. *Oxidation of Metals*, *17*(3-4), 177–194. https://doi.org/10.1007/BF00738381

[25] Tsai, S., Huntz, A., & Dolin, C. (1996). Growth mechanism of Cr_2O_3 scales: Oxygen and chromium diffusion, oxidation kinetics and effect of yttrium. *Materials Science & Engineering. A, Structural Materials : Properties, Microstructure and Processing*, *212*(1), 6–13. https://doi.org/10.1016/0921-5093(96)10173-8

[26] Hoshino, K. & Peterson, N. L. (1983). Cation Self-Diffusion in Cr_2O_3. *Journal of the American Ceramic Society*, *66*(11), c202–c203. https://doi.org/10.1111/j.1151-2916.1983.tb10572.x

[27] Schmucker, E., Petitjean, C., Martinelli, L., Panteix, P.-J., Lagha, B., & Vilasi, M. (2016). Oxidation of Ni-Cr alloy at intermediate oxygen pressures. II. Towards the lifetime prediction of alloys. *Corrosion Science*, *111*, 467–473. https://doi.org/10.1016/j.corsci.2016.05.024

[28] Lebreau, F., Islam, M. M., Diawara, B., & Marcus, P. (2014). Structural, Magnetic, Electronic, Defect, and Diffusion Properties of Cr_2O_3: A DFT+U Study. *Journal of Physical Chemistry. C*, *118*(31), 18133–18145. https://doi.org/10.1021/jp5039943

[29] Medasani, F., Sushko, M. L., Rosso, K. M., Schreiber, D. K., & Bruemmer, S. M. (2019). Temperature Dependence of Self-Diffusion in Cr_2O_3 from First Principles. *Journal of Physical Chemistry C*, *123*(36), 22139–22150. https://doi.org/10.1021/acs.jpcc.9b03218

[30] Medasani, F., Sushko, M. L., Rosso, K. M., Schreiber, D. K., & Bruemmer, S. M. (2018). First-Principles Investigation of Native Interstitial Diffusion in Cr_2O_3. *Journal of Physical Chemistry C*, *122*(24), 12984–12993. https://doi.org/10.1021/acs.jpcc.8b04383

[31] Gray, Lei, Y., & Wang, G. (2016). Charged vacancy diffusion in chromium oxide crystal: DFT and DFT+U predictions. *Journal of Applied Physics*, *120*(21), 215101–. https://doi.org/10.1063/1.4970882

[32] Kuramoto, E., Takano, Y., Kikuchi, N., & Takenaka, M. (1986). Positron annihilation lifetime measurements of irradiated iron and iron-chromium alloys. *Journal of Nuclear Materials*, *141*, 829–836. https://doi.org/10.1016/0022-3115(86)90100-5

[33] Lambrecht, M. & Malerba, L. (2011). Positron annihilation spectroscopy on binary Fe–Cr alloys and ferritic/martensitic steels after neutron irradiation. *Acta Materialia*, *59*(17), 6547–6555. https://doi.org/10.1016/j.actamat.2011.06.046

[34] Horodek, P., Siemek, K., Kobets, A. G., Kulik, M., & Meshkov, I. N. (2015). Positron beam and RBS studies of thermally grown oxide films on stainless steel grade 304. *Applied Surface Science*, *333*, 96–103. https://doi.org/10.1016/j.apsusc.2015.01.225

[35] Yabuuchi, A., Maekawa, M., & Kawasuso, A. (2011). Vacancy defects in a stress-corrosion-cracked Type 304 stainless steel investigated by positron annihilation spectroscopy. *Journal of Nuclear Materials*, *419*(1), 9–14. https://doi.org/10.1016/j.jnucmat.2011.08.012

[36] Asoka-Kumar, P., & Lynn, K. G., (1990). Implantation Profile Of Low-Energy Positrons In Solids. *Applied Physics Letters*, *57*(16), 1634–1636. https://doi.org/10.1063/1.104071

[37] van Veen, A.V., Schut, H., Clement, M., de Nijs, J. M. M., Kruseman, A., & IJpma, M. R. (1995). VEPFIT applied to depth profiling problems. *Applied Surface Science*, *85*(1-4), 216–224. https://doi.org/10.1016/0169-4332(94)00334-3

[38] van Veen, A.V., Schut, H., Devries, J., Hakvoort, R., & Ijpma, M. (1990). Analysis Of Positron Profiling Data By Means Of Vepfit. *Positron Beams For Solids And Surfaces*, AIP Conf. Proc., 218, 1, 171-198

[39] Johansson, J., Vehanen, A., Yli-Kauppila, J., Hautojärvi, P., & Moser, P. (1981). Positron lifetime measurements on electron-irradiated chromium. *Radiation Effects*, *58* (1-2), 31–33. https://doi.org/10.1080/01422448108226525

[40] Campillo Robles, M., Ogando, E., & Plazaola, F. (2007). Positron lifetime calculation for the elements of the periodic table. *Journal of Physics. Condensed Matter*, *19*(17), 176222–176222. https://doi.org/10.1088/0953-8984/19/17/176222

[41] Čížek, J., Melikhova, O., Barnovska, Z., Prochazka, I., & Islamgaliev, R. K. (2013). Vacancy clusters in ultra fine grained metals prepared by severe plastic deformation. *16th International Conference On Positron Annihilation (ICPA-16)*, *443*(1), 12008–6. https://doi.org/10.1088/1742-6596/443/1/012008

[42] Häkkinen, H., Mäkinen, S., & Manninen, M. (1989). Positron States in Dislocations: Shallow and Deep Traps. *Europhysics Letters*, *9*(8), 809–814. https://doi.org/10.1209/0295-5075/9/8/012

[43] Linderoth, S., & Hidalgo, C. (1987). Direct Evidence For Positron-Annihilation From Shallow Traps. *Physical Review. B, Condensed Matter*, *36*(7), 4054–4057. https://doi.org/10.1103/PhysRevB.36.4054

[44] Chen, Z. Q., Hu, X. W., & Wang, S. J. (1996). Positron annihilation studies of defect properties in semi-insulating GaAs. *Physica Status Solidi. A, Applied Research*, *156*(2), 277–284. https://doi.org/10.1002/pssa.2211560206

[45] Kosub, T., Kopte, M., Huehne, R., Appel, P., Shields, B., Maletinsky, P., Huebner, R., Liedke, M. O., Fassbender, J., Schmidt, O. G., & Makarov, D. (2017). Purely antiferromagnetic magnetoelectric random access memory. *Nature Communications*, *8*(1), 13985–13985. https://doi.org/10.1038/ncomms13985

[46] Troev, T., Mincov, I., Shofan, A., & Angelov, C. (1989). Positron lifetime and Doppler broadening of annihilation gamma-line measurements in neutron irradiated chromium. *Physics Letters. A*, *140*(3), 147–150. https://doi.org/10.1016/0375-9601(89)90509-4

[47] Assali, S., Elsayed, M., Nicolas, J., Liedke, M. O., Wagner, A., Butterling, M., Krause-Rehberg, R., & Moutanabbir, O. (2019). Vacancy complexes in nonequilibrium germanium-tin semiconductors. *Applied Physics Letters*, *114*(25), 251907–. https://doi.org/10.1063/1.5108878

[48] Harrington, S. P. & Devine, T. M. (2009). Relation Between the Semiconducting Properties of a Passive Film and Reduction Reaction Rates. *Journal of the Electrochemical Society*, *156*(4), C154–C159. https://doi.org/10.1149/1.3077576

[49] Sunseri, C., Piazza, S., & Di Quarto, F. (1990). Photocurrent Spectroscopic Investigations Of Passive Films On Chromium. *Journal of the Electrochemical Society*, *137*(8), 2411–2417. https://doi.org/10.1149/1.2086952

[50] Moffat, T. P., & Latanision, R. M. (1992). An Electrochemical And X-Ray Photoelectron-Spectroscopy Study Of The Passive State Of Chromium. *Journal of the Electrochemical Society*, *139*(7), 1869–1879. https://doi.org/10.1149/1.2069514

[51] Kong, D. S., Chen, S. H., Wang, C., & Yang, W. (2003). A study of the passive films on chromium by capacitance measurement. *Corrosion Science*, *45*(4), 747–758. https://doi.org/10.1016/S0010-938X(02)00148-8

[52] Poulain, C., Seyeux, A., Voyshnis, S., & Marcus, P. (2017). Volatilization and Transport Mechanisms During Cr Oxidation at 300 °C Studied In Situ by ToF-SIMS. *Oxidation of Metals*, *88*(3-4), 423–433. https://doi.org/10.1007/s11085-017-9756-y

[53] Caplan, D. & Sproule, G. I. (1981). Discussion of "On High Temperature Oxidation of Chromium II . Properties of Cr_2O_3 and the Oxidation Mechanism of Chromium" [K. P. Lillerud and P. Kofstad (pp. 2410–2419, Vol. 127, No. 11)]. *Journal of the Electrochemical Society*, *128*(6), 1388–1389. https://doi.org/10.1149/1.2127646

[54] Alemberti, A., Smirnov, V., Smith, C. F., & Takahashi, M. (2014). Overview of lead-cooled fast reactor activities. *Progress in Nuclear Energy (New Series)*, *77*, 300–307. https://doi.org/10.1016/j.pnucene.2013.11.011

[55] Fazio, C. Gröschel, F., Wagner, W., Thomsen, K., Smith, B. L., Stieglitz, R., Zanini, L., Guertin, A., Cadiou, A., Henry, J., Agostini, P., Dai, Y., Heyck, H., Dementjev, S., Panebianco, S., Almazouzi, A., Eikenberg, J., Letourneau, A., Toussaint, J. C., … Knebel, J. U. (2008). The MEGAPIE-TEST project: Supporting research and lessons learned in first-of-a-kind spallation target technology. *Nuclear Engineering and Design*, *238*(6), 1471–1495. https://doi.org/10.1016/j.nucengdes.2007.11.006

[56] Lu, Y., Wang, Z. B., Song, Y. Y., & Rong, L. J. (2016). Effects of pre-formed nanostructured surface layer on oxidation behaviour of 9Cr2WVTa steel in air and liquid Pb–Bi eutectic alloy. *Corrosion Science*, *102*, 301–309. https://doi.org/10.1016/j.corsci.2015.10.021

[57] Popovic, M. P., Chen, K., Shen, H., Stan, C. V., Olmsted, D. L., Tamura, N., Asta, M., Abad, M. D., & Hosemann, P. (2018). A study of deformation and strain induced in bulk by the oxide layers formation on a Fe-Cr-Al alloy in high-temperature liquid Pb-Bi eutectic. *Acta Materialia*, *151*, 301–309. https://doi.org/10.1016/j.actamat.2018.03.041

[58] Hosemann, P., Hofer, C., Hlawacek, G., Li, N., Maloy, S. A., & Teichert, C. (2012). Structural, electrical and magnetic measurements on oxide layers grown on 316L exposed to liquid lead bismuth eutectic. *Journal of Nuclear Materials*, *421*(1-3), 140–146.

[59] Chen, J., Xiao, Q., Lu, Z., Ru, X., Peng, H., Xiong, Q., & Li, H. (2017). Characterization of interfacial reactions and oxide films on 316L stainless steel in various simulated PWR primary water environments. *Journal of Nuclear Materials*, *489*, 137–149. https://doi.org/10.1016/j.jnucmat.2017.03.029

[60] Zhang J., & Li, N. (2008). Review of the studies on fundamental issues in LBE corrosion. *Journal of Nuclear Materials*, *373*(1), 351–377. https://doi.org/10.1016/j.jnucmat.2007.06.019

[61] Xu, Y., Zhang, Y., Li, X., Liu, W., Li, D., Liu, C. S., Pan, B. C., & Wang, Z. (2017). Effects of iron and chromium on the dynamic properties of oxygen in liquid lead–bismuth eutectic alloy. *Corrosion Science*, *118*, 1–11. https://doi.org/10.1016/j.corsci.2017.01.003

[62] Shankar Rao, V., Lim, J., Hwang, I. S., & Singhal, L. K. (2012). Characterization of oxide scales grown on 216L stainless steels in liquid lead–bismuth eutectic. *Corrosion Science*, *63*, 113–118. https://doi.org/10.1016/j.corsci.2012.05.016

[63] Soulas, R., Cheynet, M., Rauch, E., Neisius, T., Legras, L., Domain, C., & Brechet, Y. (2013). TEM investigations of the oxide layers formed on a 316L alloy in simulated PWR environment. *Journal of Materials Science*, *48*(7), 2861–2871. https://doi.org/10.1007/s10853-012-6975-0

[64] Qiu, J., Han, J., Schoell, R., Popovic, M., Ghanbari, E., Kaoumi, D., Scully, J. R., Macdonald, D. D., & Hosemann, P. (2020). *Electrical properties of thermal oxide scales on pure iron in liquid lead-bismuth eutectic*. https://doi.org/10.48550/arXiv.2010.05372

[65] Jiao, Z. & Was, G. (2012). Oxidation of a Proton-Irradiated 316 Stainless Steel in Simulated BWR NWC Environment. In *15th International Conference on Environmental Degradation of Materials in Nuclear Power Systems-Water Reactors* (pp. 1329–1338). John Wiley & Sons, Inc. https://doi.org/10.1002/9781118456835.ch138

[66] Tannhauser, D.S. (1962). Conductivity in iron oxides. *The Journal of Physics and Chemistry of Solids.*, *23*(1-2), 25–34. https://doi.org/10.1016/0022-3697(62)90053-7

[67] Schroer, C, Nold, E, and Konys, J. (2009) Micro-Analysis of 316L Stainless-Steel After Long-Term Exposure to Lead-Bismuth Eutectic at 550 C. In *Proceedings of EUROCORR*, Nice, France.

[68] Chao, C., Lin, L. F., & Macdonald, D. D. (1981). A Point Defect Model for Anodic Passive Films: I . Film Growth Kinetics. *Journal of the Electrochemical Society*, *128*(6), 1187–1194. https://doi.org/10.1149/1.2127591

[69] Was, G., Jiao, Z., Getto, E., Sun, K., Monterrosa, A. M., Maloy, S. A., Anderoglu, O., Sencer, B. H., & Hackett, M. (2014). Emulation of reactor irradiation damage using ion beams. *Scripta Materialia*, *88*(C), 33–36. https://doi.org/10.1016/j.scriptamat.2014.06.003

[70] Frazer, D., Qvist, S., Parker, S., Krumwiede, D. L., Caro, M., Tesmer, J., Maloy, S. A., Wang, Y. Q., & Hosemann, P. (2016). Degradation of HT9 under simultaneous ion beam irradiation and liquid metal corrosion. *Journal of Nuclear Materials*, *479*(C), 382–389. https://doi.org/10.1016/j.jnucmat.2016.06.039

[71] Deng, P., Peng, Q., Han, E.-H., Ke, W., Sun, C., & Jiao, Z. (2017). Effect of irradiation on corrosion of 304 nuclear grade stainless steel in simulated PWR primary water. *Corrosion Science*, *127*, 91–100. https://doi.org/10.1016/j.corsci.2017.08.010

[72] Perrin, S., Marchetti, L., Duhamel, C., Sennour, M., & Jomard, F. (2013). Influence of Irradiation on the Oxide Film Formed on 316 L Stainless Steel in PWR Primary Water. *Oxidation of Metals*, *80*(5-6), 623–633. https://doi.org/10.1007/s11085-013-9401-3

[73] Boudinov, H., Tan, H., & Jagadish, C. (2001). Electrical isolation of n-type and p-type InP layers by proton bombardment. *Journal of Applied Physics*, *89*(10), 5343–5347. https://doi.org/10.1063/1.1365063

[74] Islam, M. M., Liedke, M. O., Winarski, D., Butterling, M., Wagner, A., Hosemann, P., Wang, Y., Uberuaga, B., & Selim, F. A. (2020). Chemical manipulation of hydrogen induced high p-type and n-type conductivity in Ga_2O_3. *Scientific Reports*, *10*(1), 6134–6134. https://doi.org/10.1038/s41598-020-62948-2

[75] Schwenk, W. & Rahmel, A. (1986). Theoretical considerations on phase boundary reactions and mass transfer during the oxidation of iron. *Oxidation of Metals*, *25*(5-6), 293–303. https://doi.org/10.1007/BF01072910

[76] Ziegler, J. F., Ziegler, M. D., & Biersack, J. P. (2010). SRIM – The stopping and range of ions in matter (2010). *Nuclear Instruments & Methods in Physics Research. Section B, Beam Interactions with Materials and Atoms*, *268*(11), 1818–1823. https://doi.org/10.1016/j.nimb.2010.02.091

[77] Konobeyev, A.Y., Fischer, U., Korovin, Y. A., & Simakov, S. P. (2017). Evaluation of effective threshold displacement energies and other data required for the calculation of advanced atomic displacement cross-sections. *Nuclear Energy and Technology*, *3*(3), 169–175. https://doi.org/10.1016/j.nucet.2017.08.007

[78] Owusu-Mensah, C.J., Morales, A. L., Yano, K., Taylor, S. D., Schreiber, D. K., Uberuaga, B. P., & Kaoumi, D. (2022). Surprisingly high irradiation-induced defect mobility in $Fe3O_4$ as

revealed through in situ transmission electron microscopy. *Materials Characterization*, *187*(C), 111863–. https://doi.org/10.1016/j.matchar.2022.111863

[79] Selim, F.A. (2021). Positron annihilation spectroscopy of defects in nuclear and irradiated materials- a review. *Materials Characterization*, *174*(C), 110952–. https://doi.org/10.1016/j.matchar.2021.110952

[80] Winarski, D., Anwand, W., Wagner, A., Saadatkia, P., Selim, F. A., Allen, M., Wenner, B., Leedy, K., Allen, J., Tetlak, S., & Look, D. C. (2016). Induced conductivity in sol-gel ZnO films by passivation or elimination of Zn vacancies. *AIP Advances*, *6*(9), 95004–095004–10. https://doi.org/10.1063/1.4962658

[81] Selim, F.A., Varney, C. R., Tarun, M. C., Rowe, M. C., Collins, G. S., & McCluskey, M. D. (2013). Positron lifetime measurements of hydrogen passivation of cation vacancies in yttrium aluminum oxide garnets. *Physical Review. B, Condensed Matter and Materials Physics*, *88*(17). https://doi.org/10.1103/PhysRevB.88.174102

[82] Muhich, C.L., Aston, V. J., Trottier, R. M., Weimer, A. W., & Musgrave, C. B. (2016). First-Principles Analysis of Cation Diffusion in Mixed Metal Ferrite Spinels. *Chemistry of Materials*, *28*(1), 214–226. https://doi.org/10.1021/acs.chemmater.5b03911

[83] Yano, K. H., Kohnert, A. A., Banerjee, A., Edwards, D. J., Holby, E. F., Kaspar, T. C., Kim, H., Lach, T. G., Taylor, S. D., Wang, Y., Uberuaga, B. P., & Schreiber, D. K. (2021). Radiation-Enhanced Anion Transport in Hematite. *Chemistry of Materials*, *33*(7), 2307–2318. https://doi.org/10.1021/acs.chemmater.0c04235

[84] Perriot, R., Matthews, C., Cooper, M. W. D., Uberuaga, B. P., Stanek, C. R., & Andersson, D. A. (2019). Atomistic modeling of out-of-pile xenon diffusion by vacancy clusters in UO2. *Journal of Nuclear Materials*, *520*, 96–109. https://doi.org/10.1016/j.jnucmat.2019.03.050

[85] Zamora, R.J., Voter, A. F., Perez, D., Perriot, R., & Uberuaga, B. P. (2016). The effects of cation-anion clustering on defect migration in MgAl2O4. *Physical Chemistry Chemical Physics : PCCP*, *18*(29), 19647–19654. https://doi.org/10.1039/c6cp03931f

[86] Zinkle, S.J. (1996). Irradiation Spectrum and Ionization-Induced Diffusion Effects in Ceramics. *MRS Proceedings*, *439*. https://doi.org/10.1557/PROC-439-667

[87] Park, Y. K., Waber, J. T., Meshii, M., Snead Jr, C. L., & Park, C. G. (1986). Dislocation studies on deformed single crystals of high-purity iron using positron annihilation: Determination of dislocation densities. *Physical Review B: Condensed Matter, 34*(2), 823–836. https://doi.org/10.1103/PhysRevB.34.823

[88] Puska, M.J. & Nieminen, R. M. (1983). Defect spectroscopy with positrons: a general calculational method. *Journal of Physics. F, Metal Physics*, *13*(2), 333–346. https://doi.org/10.1088/0305-4608/13/2/009

[1] Kerl, R. Wolff, J., & Hehenkamp, T. (1999). Equilibrium vacancy concentrations in FeAl and FeSi investigated with an absolute technique. *Intermetallics*, *7*(3), 301–308. https://doi.org/10.1016/S0966-9795(98)00118-6

[2] Dimitrov, C., Tenti, M., & Dimitrov, O. (1981). Resistivity recovery in austenitic Fe-Cr-Ni alloys neutron irradiated at 23K. *Journal of Physics F: Metal Physics*, *11*(4), 753. https://doi.org/10.1088/0305-4608/11/4/009

[3] Persaud, Barnard, J. J., Guo, H., Hosemann, P., Lidia, S., Minor, A. M., Seidl, P. A., & Schenkel, T. (2015). Accessing Defect Dynamics using Intense, Nanosecond Pulsed Ion Beams. *Physics Procedia, 66, 604-609.* https://doi.org/10.1016/j.phpro.2015.05.080

[4] Wiedersich, H. (1972). On the theory of void formation during irradiation. *Radiation Effects 12: 1-2,* 111–125. https://doi.org/10.1080/00337577208231128

[5] MATLAB. Version 9.4.0 (R2018a). Natick, Massachusetts: The MathWorks Inc., (2018).

[6] Ziegler, J. F., Ziegler, M. D., & Biersack, J. P. (2010). SRIM – The stopping and range of ions in matter (2010). *Nuclear Instruments & Methods in Physics Research. Section B, Beam Interactions with Materials and Atoms*, *268*(11), 1818–1823. https://doi.org/10.1016/j.nimb.2010.02.091

[7] Stoller, R.E., Toloczko, M. B., Was, G. S., Certain, A. G., Dwaraknath, S., & Garner, F. A. (2013). On the use of SRIM for computing radiation damage exposure. *Nuclear Instruments & Methods in Physics Research. Section B, Beam Interactions with Materials and Atoms*, *310*, 75–80. https://doi.org/10.1016/j.nimb.2013.05.008

[8] ASTM Standards, ASTM International, PA, E706(ID), ASTM E693-12, (2012).

[9] Anwand, W., Wagner, A., Brauer, G., Butterling, M., & Kissener, H. R. (2012). Design and Construction of a Slow Positron Beam for Solid and Surface Investigations. *Diffusion and Defect Data. Solid State Data. Pt. A, Defect and Diffusion Forum*, *331*, 25–40. https://doi.org/10.4028/www.scientific.net/DDF.331

[10] Wagner, A., Butterling, M., Liedke, M. O., Potzger, K., & Krause-Rehberg, R. (2018). Positron annihilation lifetime and Doppler broadening spectroscopy at the ELBE facility. *AIP Conference Proceedings*, *1970*(1). https://doi.org/10.1063/1.5040215

[11] Wagner, A. Anwand, W., Attallah, A. G., Dornberg, G., Elsayed, M., Enke, D., Hussein, A. E. M., Krause-Rehberg, R., Liedke, M. O., Potzger, K., & Trinh, T. T. (2017). Positron annihilation lifetime spectroscopy at a superconducting electron accelerator. *14th*

International Workshop on Slow Positron Beam Techniques & Applications, *791*(1), 12004. https://doi.org/10.1088/1742-6596/791/1/012004

[12] Hautojärvi, Dupasquier, A., Hautojärvi, P. (Pekka), & Dupasquier, A. (Alfredo). (1979). *Positrons in solids*. pp. 491-522. Springer-Verlag.

[13] Makhov, A. F. (1961). The penetration of electrons into solids. 1. The intensity of an electron beam, transverse paths of electrons. *Soviet Physics-Solid State*, *2*(9), 1934-1941.

[14] Seeger, A. (1995). Positron diffusion in solids and in liquid metals. *Applied Surface Science*, *85*(1-4), 8–16. https://doi.org/10.1016/0169-4332(94)00300-9

[15] Jiang, J., Wu, Y. C., Liu, X. B., Wang, R. S., Nagai, Y., Inoue, K., Shimizu, Y., & Toyama, T. (2015). Microstructural evolution of RPV steels under proton and ion irradiation studied by positron annihilation spectroscopy. *Journal of Nuclear Materials*, *458*, 326–334. https://doi.org/10.1016/j.jnucmat.2014.12.113

[16] Shi, J.J. Zhao, W. Z., Wu, Y. C., Liu, X. B., & Jiang, J. (2019). Characterization of proton-irradiated Chinese A508-3-type reactor pressure vessel steel by slow positron beam, TEM, and nanoindentation. *Nuclear Instruments & Methods in Physics Research. Section B, Beam Interactions with Materials and Atoms*, *443*, 62–69. https://doi.org/10.1016/j.nimb.2019.01.044

[17] Kinomura, A., Suzuki, R., Ohdaira, T., Oshima, N., O'Rourke, B. E., & Nishijima, T. (2013). In-situ positron lifetime spectroscopy of radiation damage by simultaneous irradiation of slow-positron and ion beams. *16th International Conference On Positron Annihilation (ICPA-16)*, *443*(1), 12043–12044. https://doi.org/10.1088/1742-6596/443/1/012043

[18] Stoller, R.E. (2012). 1.11 - Primary Radiation Damage Formation. In *Comprehensive Nuclear Materials* (pp. 293–332). Elsevier Ltd. https://doi.org/10.1016/B978-0-08-056033-5.00027-6

[19] Sprouster, D.J., Sun, C., Zhang, Y., Chodankar, S. N., Gan, J., & Ecker, L. E. (2019). Irradiation-Dependent Helium Gas Bubble Superlattice in Tungsten. *Scientific Reports*, *9*(1), 2277–2277. https://doi.org/10.1038/s41598-019-39053-0

[20] Lupinacci, A., Chen, K., Li, Y., Kunz, M., Jiao, Z., Was, G. S., Abad, M. D., Minor, A. M., & Hosemann, P. (2015). Characterization of ion beam irradiated 304 stainless steel utilizing nanoindentation and Laue microdiffraction. *Journal of Nuclear Materials*, *458*(C), 70–76. https://doi.org/10.1016/j.jnucmat.2014.11.050

[21] Yan, Q., Gigax, J., Chen, D., Garner, F. A., & Shao, L. (2016). Monte Carlo modeling of cavity imaging in pure iron using back-scatter electron scanning microscopy. *Journal of Nuclear Materials*, *480*(C), 420–428. https://doi.org/10.1016/j.jnucmat.2016.08.016

[22] Wirth, B.D., Caturla, M. J., Diaz de la Rubia, T., Khraishi, T., & Zbib, H. (2001). Mechanical property degradation in irradiated materials: A multiscale modeling approach. *Nuclear Instruments & Methods in Physics Research. Section B, Beam Interactions with Materials and Atoms*, *180*(1), 23–31. https://doi.org/10.1016/S0168-583X(01)00392-5

[23] Robach, J. S., Robertson, I. M., Wirth, B. D., & Arsenlis, A. (2003). In-situ transmission electron microscopy observations and molecular dynamics simulations of dislocation-defect interactions in ion-irradiated copper. *Philosophical Magazine (Abingdon, England)*, *83*(8), 955–967. https://doi.org/10.1080/0141861031000065329

[24] Hirschmann, E., Butterling, M., Hernandez Acosta, U., Liedke, M., Attallah, A. ., Petring, P., Görler, M., Krause-Rehberg, R., & Wagner, A. (2021). A new system for real-time data acquisition and pulse parameterization for digital positron annihilation lifetime spectrometers with high repetition rates. *Journal of Instrumentation*, *16*(8), P08001–. https://doi.org/10.1088/1748-0221/16/08/P08001

[25] Antonelli, A., Kaxiras, E., & Chadi, D. (1998). Vacancy in silicon revisited: Structure and pressure effects. *Physical Review Letters*, *81*(10), 2088–2091. https://doi.org/10.1103/PhysRevLett.81.2088

[26] Olsen, J.V., Kirkegaard, P., Pedersen, N. J., & Eldrup, M. (2007). PALSfit: A new program for the evaluation of positron lifetime spectra. *Physica Status Solidi. C*, *4*(10), 4004–4006. https://doi.org/10.1002/pssc.200675868

[27] Staab, T.E.M., Sieck, A., Haugk, M., Puska, M., Frauenheim, T., & Leipner, H. (2002). Stability of large vacancy clusters in silicon. *Physical Review. B, Condensed Matter*, *65*(11). https://doi.org/10.1103/PhysRevB.65.115210

[28] Campillo Robles, J.M., Ogando, E., & Plazaola, F. (2007). Positron lifetime calculation for the elements of the periodic table. *Journal of Physics. Condensed Matter*, *19*(17), 176222–176222. https://doi.org/10.1088/0953-8984/19/17/176222

[29] Morehead, F. F., Crowder, B. L., & Title, R. S. (1972). Formation of amorphous silicon by ion bombardment as a function of ion, temperature, and dose. *Journal of Applied Physics*, *43*(3), 1112-1118. https://doi.org/10.1063/1.1661223

[30] Pelaz, L., Marqués, L. A., López, P., Santos, I., Aboy, M., & Barbolla, J. (2005). Atomistic modeling of ion beam induced amorphization in silicon. *Nuclear Instruments & Methods in Physics Research. Section B, Beam Interactions with Materials and Atoms*, *241*(1-4), 501–505. https://doi.org/10.1016/j.nimb.2005.07.096

[31] Pelaz, L., Marques, L., & Barbolla, J. (2004). Ion-beam-induced amorphization and recrystallization in silicon. *Journal of Applied Physics*, *96*(11), 5947–5976. https://doi.org/10.1063/1.1808484

[32] Huang, X., Xie, Y., Balooch, M., Lubner, S., & Hosemann, P. (2022). Helium implantation in Si (100): Swelling, microstructure, and mechanical property changes. *Journal of Applied Physics*, *132*(2), 025106. https://doi.org/10.1063/5.0096802

[33] Proposal for Department of Energy, Basic Energy Sciences (DE-FOA-0002653), (Proposal ID: 0000268580), *Fundamental Understanding of Transport Under Reactor Extremes (FUTURE),* August 2022

[34] Potzger, K. (November 22, 2013). *AIDA Layout*. Helmholtz-Zentrum Dresden-Rossendorf, HZDR. Retrieved November 21, 2022, from https://www.hzdr.de/db/Cms?pNid=no&pOid=40409

Discussion

[1] MATLAB. Version 9.4.0 (R2018a). Natick, Massachusetts: The MathWorks Inc., (2018).

[2] Wiedersich, H. (1972). On the theory of void formation during irradiation. *Radiation Effects 12: 1-2,* 111–125. https://doi.org/10.1080/00337577208231128

[3] K-P model

[4] Ziegler, J. F., Ziegler, M. D., & Biersack, J. P. (2010). SRIM – The stopping and range of ions in matter (2010). *Nuclear Instruments & Methods in Physics Research. Section B, Beam Interactions with Materials and Atoms*, *268*(11), 1818–1823. https://doi.org/10.1016/j.nimb.2010.02.091

[5] Park, Y. K., Waber, J. T., Meshii, M., Snead Jr, C. L., & Park, C. G. (1986). Dislocation studies on deformed single crystals of high-purity iron using positron annihilation: Determination of dislocation densities. *Physical Review B: Condensed Matter, 34*(2), 823–836. https://doi.org/10.1103/PhysRevB.34.823

[6] Puska, M.J. & Nieminen, R. M. (1983). Defect spectroscopy with positrons: a general calculational method. *Journal of Physics. F, Metal Physics*, *13*(2), 333–346. https://doi.org/10.1088/0305-4608/13/2/009

[7] Iwai, T. & Tsuchida, H. (2012). In situ positron beam Doppler broadening measurement of ion-irradiated metals – Current status and potential. *Nuclear Instruments & Methods in Physics Research. Section B, Beam Interactions with Materials and Atoms*, *285*, 18–23. https://doi.org/10.1016/j.nimb.2012.05.005

[8] Lillerud, K. P. & Kofstad, P. (1980). On High Temperature Oxidation of Chromium: I. Oxidation of Annealed, Thermally Etched Chromium at 800°–1100°C. *Journal of the Electrochemical Society*, *127*(11), 2397–2410. https://doi.org/10.1149/1.2129478

[9] Lillerud, K. P. & Kofstad, P. (1980). On High Temperature Oxidation of Chromium: II. Oxidation of Annealed, Thermally Etched Chromium at 800°–1100°C. *Journal of the Electrochemical Society*, *127*(11), 2410–2419. https://doi.org/10.1149/1.2129481

[10] Harrington, S. P. & Devine, T. M. (2009). Relation Between the Semiconducting Properties of a Passive Film and Reduction Reaction Rates. *Journal of the Electrochemical Society*, *156*(4), C154–C159. https://doi.org/10.1149/1.3077576

[11] Sunseri, C., Piazza, S., & Di Quarto, F. (1990). Photocurrent Spectroscopic Investigations Of Passive Films On Chromium. *Journal of the Electrochemical Society*, *137*(8), 2411–2417. https://doi.org/10.1149/1.2086952

[12] Moffat, T. P., & Latanision, R. M. (1992). An Electrochemical And X-Ray Photoelectron-Spectroscopy Study Of The Passive State Of Chromium. *Journal of the Electrochemical Society*, *139*(7), 1869–1879. https://doi.org/10.1149/1.2069514

[13] Kong, D. S., Chen, S. H., Wang, C., & Yang, W. (2003). A study of the passive films on chromium by capacitance measurement. *Corrosion Science*, *45*(4), 747–758. https://doi.org/10.1016/S0010-938X(02)00148-8

[14] Lebreau, F., Islam, M. M., Diawara, B., & Marcus, P. (2014). Structural, Magnetic, Electronic, Defect, and Diffusion Properties of Cr_2O_3: A DFT+U Study. *Journal of Physical Chemistry. C*, *118*(31), 18133–18145. https://doi.org/10.1021/jp5039943

[15] Medasani, F., Sushko, M. L., Rosso, K. M., Schreiber, D. K., & Bruemmer, S. M. (2019). Temperature Dependence of Self-Diffusion in Cr_2O_3 from First Principles. *Journal of Physical Chemistry C*, *123*(36), 22139–22150. https://doi.org/10.1021/acs.jpcc.9b03218

[16] Medasani, F., Sushko, M. L., Rosso, K. M., Schreiber, D. K., & Bruemmer, S. M. (2018). First-Principles Investigation of Native Interstitial Diffusion in Cr_2O_3. *Journal of Physical Chemistry C*, *122*(24), 12984–12993. https://doi.org/10.1021/acs.jpcc.8b04383

[17] Gray, Lei, Y., & Wang, G. (2016). Charged vacancy diffusion in chromium oxide crystal: DFT and DFT+U predictions. *Journal of Applied Physics*, *120*(21), 215101–. https://doi.org/10.1063/1.4970882

[18] Schroer, C, Nold, E, and Konys, J. (2009) Micro-Analysis of 316L Stainless-Steel After Long-Term Exposure to Lead-Bismuth Eutectic at 550 C. In *Proceedings of EUROCORR*, Nice, France.

[19] Chao, C., Lin, L. F., & Macdonald, D. D. (1981). A Point Defect Model for Anodic Passive Films: I . Film Growth Kinetics. *Journal of the Electrochemical Society*, *128*(6), 1187–1194. https://doi.org/10.1149/1.2127591

[20] Qiu, J., Han, J., Schoell, R., Popovic, M., Ghanbari, E., Kaoumi, D., Scully, J. R., Macdonald, D. D., & Hosemann, P. (2020). *Electrical properties of thermal oxide scales on pure iron in liquid lead-bismuth eutectic*. https://doi.org/10.48550/arXiv.2010.05372

[21] Schwenk, W. & Rahmel, A. (1986). Theoretical considerations on phase boundary reactions and mass transfer during the oxidation of iron. *Oxidation of Metals*, *25*(5-6), 293–303. https://doi.org/10.1007/BF01072910

[22] Selim, F.A. (2021). Positron annihilation spectroscopy of defects in nuclear and irradiated materials- a review. *Materials Characterization*, *174*(C), 110952–. https://doi.org/10.1016/j.matchar.2021.110952

[23] Čížek, J. (2018). Characterization of lattice defects in metallic materials by positron annihilation spectroscopy: A review. *Journal of Materials Science & Technology*, *34*(4), 577–598. https://doi.org/10.1016/j.jmst.2017.11.050

[24] Proposal for Department of Energy, Basic Energy Sciences (DE-FOA-0002653), (Proposal ID: 0000268580), *Fundamental Understanding of Transport Under Reactor Extremes (FUTURE),* August 2022